May 1998 • NREL/SR-520-24724

Amorphous Silicon Research

Final Technical Progress Report
1 August 1994–28 February 1998

S. Guha
United Solar Systems Corporation
Troy, Michigan

National Renewable Energy Laboratory
1617 Cole Boulevard
Golden, Colorado 80401-3393
A national laboratory of
the U.S. Department of Energy
Managed by Midwest Research Institute
for the U.S. Department of Energy
under Contract No. DE-AC36-83CH10093

NREL/SR-520-24724

Amorphous Silicon Research

Final Technical Progress Report
1 August 1994–28 February 1998

S. Guha
United Solar Systems Corporation
Troy, Michigan

NREL technical monitor: K. Zweibel

National Renewable Energy Laboratory
1617 Cole Boulevard
Golden, Colorado 80401-3393
A national laboratory of
the U.S. Department of Energy
Managed by Midwest Research Institute
for the U.S. Department of Energy
under Contract No. DE-AC36-83CH10093

Prepared under Subcontract No. ZAN-4-13318-02
May 1998

Available to DOE and DOE contractors from:
Office of Scientific and Technical Information (OSTI)
P.O. Box 62
Oak Ridge, TN 37831
Prices available by calling (423) 576-8401

Available to the public from:
National Technical Information Service (NTIS)
U.S. Department of Commerce
5285 Port Royal Road
Springfield, VA 22161
(703) 487-4650

Preface

This Final Technical Progress Report covers the work performed by United Solar Systems Corp. for the period 1 August 1994 to 28 February 1998 under DOE/NREL Subcontract No. ZAN-4-13318-02. The following personnel participated in the research program.

A. Banerjee, E. Chen, T. Glatfelter, S. Guha (Principal Investigator), K. Lord, M. Haag, G. Hammond, M. Hopson, T. Palmer, S. Sugiyama, D. Wolf, and J. Yang.

We would like to thank V. Trudeau for preparation of this report.

Executive Summary

Objectives

The principal objective of this R&D program is to expand, enhance and accelerate knowledge and capabilities for the development of high-performance, two-terminal multijunction amorphous silicon (a-Si) alloy cells and modules. The near-term goal of the program is to achieve 12% stable active-area efficiency using the multijunction approach. The long-term goal is to achieve 15% stable efficiency multijunction modules.

Approach

The major effort of this program is to develop high efficiency component cells and incorporate them in the triple-junction structure to obtain the highest stable efficiency. New and improved deposition regimes including a higher rate (~3 Å/s) deposition of intrinsic layers were investigated to obtain better cell performance. Fundamental studies to obtain better understanding of material and cell performance were undertaken.

Status/Accomplishments

- Several new deposition regimes/conditions were explored to investigate their effect on material/device performance. No beneficial effect on cell performance could be observed by i) ion bombardment during deposition, ii) preheating the deposition gas mixture and iii) He dilution.

- In order to facilitate optimum ion bombardment during growth, a large parameter space involving chamber pressure, rf power and hydrogen dilution were investigated. No further improvement in cell efficiency could be obtained in this expanded parameter space.

- We carried out a series of experiments using discharge modulation at various pulsed-plasma intervals in order to study the effect of Si-particle incorporation on solar cell performance. We found no observable difference in cell performance under discharge modulated and standard conditions for deposition regimes investigated.

- Hydrogen dilution during deposition is found to improve both the initial and stable performance of a-Si and a-SiGe alloy cells. No correlation was observed between deep defect density measured by the constant photocurrent method and cell efficiency.

- We conducted a series of temperature ramping experiments on samples prepared with high and low hydrogen dilutions in order to study the effect of hydrogen effusion on solar cell performance. We found that hydrogen effusion in highly diluted samples resulted in little change in cell efficiency, but caused a reduction in cell performance in low dilution samples.

- Using internal photoemission method, the electrical bandgap of microcrystalline *p* layer used in high efficiency solar cell was measured to be 1.6 eV. The band discontinuity at the microcrystalline-amorphous interface is found to be predominantly at the valence band edge. Use of these parameters in numerical simulations is found to predict solar cell performance accurately.

- New measurement techniques were developed to evaluate the interface and bulk contribution of losses to solar cell performance.

- We replaced hydrogen with deuterium and found deuterated amorphous silicon alloy solar cells exhibit reduced light-induced degradation. The deuterated alloys have structural similarity with hydrogenated alloys grown with heavy hydrogen dilution. The improved stability is believed to arise from improved microstructures.

- The incorporation of a microcrystalline *n* layer in a multijunction cell is seen to improve cell performance.

- We achieved a world record single-junction a-Si alloy stable cell efficiency of 9.2% with an active-area of 0.25 cm^2 grown with high hydrogen dilution.

- We achieved state-of-the-art top, middle, and bottom component cells with the initial and stable characteristics shown in Table 1.

- We achieved a world record triple-junction, stable, active-area cell efficiency of 13.0% with an active area of 0.25 cm^2. The J-V characteristics are shown in Table 1. Table 1 also lists progress made in cell efficiencies since the beginning of the subcontract.

- Status of component cells and triple-junction devices in which the intrinsic layers are deposited at a higher rate of 3 Å/s is summarized in Table 2.

Table 1. Initial and Light-soaked J-V Characteristics of the Component and Triple-junction Cells at United Solar.

Cell	Status	J_{sc} (mA/cm^2)	V_{oc} (V)	FF	P_{max} (mW/cm^2)
top[d]	initial[a]	8.97	0.980	0.761	6.69
middle[e]	initial[b]	9.30	0.753	0.687	4.81
bottom[f]	initial[c]	12.2	0.631	0.671	5.17
triple[d]	initial[c]	8.57	2.357	0.723	14.6
top[d]	1994 stable[b]	7.3	0.97	0.72	5.1
	1997 stable[a]	8.78	0.953	0.709	5.93
middle[e]	1994 stable[b]	7.6	0.76	0.60	3.5
	1997 stable[b]	8.92	0.717	0.587	3.75
bottom[f]	1994 stable[c]	9.84	0.67	0.55	3.60
	1996 stable[c]	11.4	0.60	0.56	3.80
	1997 stable[c]	11.12	0.609	0.622	4.21
triple[d]	1995 stable[c]	6.87	2.38	0.68	11.1
	1996 stable[c]	7.49	2.283	0.692	11.8
	1997 stable[c]	8.27	2.294	0.684	13.0

a deposited on a bare stainless steel substrate
b deposited on a textured substrate coated with Cr
c deposited on textured Ag/ZnO back reflector
d measured under AM1.5 illumination
e measured under AM1.5 with a λ>530 nm filter
f measured under AM1.5 with a λ>630 nm filter

Table 2. Status of Initial and Stabilized Solar Cells Deposited at 3 Å/s.

Cell	Status	Active-area J_{sc} (mA/cm^2)	V_{oc} (V)	FF	P_{max} (mW/cm^2)
Top[ad]	Initial	8.73	0.967	0.749	6.32
	Stabilized	8.56	0.904	0.646	5.00
Middle[bd]	Initial	8.73	0.742	0.666	4.31
	Stabilized	8.17	0.694	0.539	3.06
Bottom[cd]	Initial	10.62	0.62	0.63	4.15
	Stabilized	10.11	0.594	0.564	3.39
Triple[ae]	Initial	8.09	2.265	0.689	12.6
	Stabilized	7.63	2.18	0.614	10.2

[a] measured under AM1.5
[b] measured under AM1.5 with a λ>530 nm filter
[c] measured under AM1.5 with a λ>630 nm filter
[d] deposited onto a bare ss substrate
[e] deposited onto a textured Ag/ZnO substrate

Table of Contents

List of Figures

Page

List of Tables

Section 1

Introduction

This report describes the research performed in a four-phase, three and a half-year program under NREL Subcontract No. ZAN-4-13318-02. The research program is intended to expand, enhance and accelerate knowledge and capabilities for the development of high-performance, two-terminal multijunction amorphous silicon (a-Si) alloy cells and modules.

It is now widely recognized that a multijunction, multibandgap approach has the potential of achieving the highest stable efficiency in a-Si alloy solar cells. In this approach, the bandgap of the materials of the component cell is varied in order to capture a wide spectrum of the solar photons. Significant progress has been made in the development of materials and cell design in the last few years, and a stable module efficiency of 10.2% has been demonstrated over one-square-foot area using a triple-junction approach in which the bottom two component cells use amorphous silicon germanium (a-SiGe) alloy. In order to meet the Department of Energy goal of achievement of 15% stable module efficiency, it is necessary to make further improvements in each of the component cells. This has been the thrust of the current program.

The research report describes the activities on both materials and device research. Important changes in deposition conditions which affect both the plasma and the growth chemistry have been investigated, and the results are reported in Sections 2 through 5. Specifically, in Section 2, we discuss the effect of ion bombardment and gas preheating on the performance of a-Si and a-SiGe alloy solar cells. In Section 3, we present results on the effect of plasma chemistry on a-Si alloy cell performance where the chemistry is altered by changing chamber pressure, rf power, substrate temperature and hydrogen dilution. In Section 4, we investigate the effect of particulates in the plasma on cell properties. The density of particulates was controlled by modulation of the discharge during deposition. Section 5 discusses the effect of hydrogen and helium dilution on a-Si and a-SiGe alloy materials and devices. To understand the role of hydrogen bonding on cell properties, we have investigated the effect of hydrogen effusion on cell performance for cells grown with low and high hydrogen dilution. The results, both for initial and light-degraded states, are presented in Section 6. The use of microcrystalline *p* layer has been shown to improve solar cell performance considerably. Not much information, however, is available regarding the bandgap and the location of the conduction and the valence band edges of this material. In Section 7, we present experimental results on these parameters and discuss the effect of band discontinuity at the microcrystalline-amorphous interface on the performance of solar cells. In the design of solar cells, it is important to recognize the interface and bulk parameters that contribute to solar cell performance. In Sections 8 and 9, we describe carefully-designed experiments which allow us to identify the different losses coming from the bulk and the interface. We have also replaced hydrogen with deuterium in the deposition gas mixtures and investigated the effect on cell performance and stability. The results are presented in Section 10 where a possible correlation between stability and microstructure of the material is discussed. The tunnel junction between the doped layers in a multijunction cell plays an important role in determining cell performance. In Section 11, we discuss the effect of the incorporation of a microcrystalline *n*-type layer in the tunnel junction on multijunction cell performance. In Section 12, we present the status of the component cell; incorporation of these component cells to design a high-efficiency, triple-junction cell is discussed in Section 13. Light-induced degradation studies are presented and the achievement of a new world record of 13% stable active-area cell efficiency is reported. The performance of the triple-junction cells as a function of temperature is also discussed. In Section 14, we report the status of the component cell and triple-junction devices in which the intrinsic layers are deposited at ~3 Å/s. The initial and light-soaked cell characteristics are presented. Solar cells with high stable efficiencies deposited at high growth rates are very desirable for photovoltaic manufacturing. Finally, in Section 15, we comment on the future directions of research.

Section 2

Effects of Ion Bombardment and Gas Preheating on a-Si Alloy Solar Cells

Introduction

Control of growth chemistry is known to play a very important role in improving the properties of a-Si and a-SiGe alloy materials and solar cells. Ion bombardment on film growing surface by applying an electric bias is known to be an effective way to modify the film growth mechanism. By controlling the flux and energy of impinging ions, reactive species can be energized to find a favorable site and form a denser network. The effect of ion bombardment during film growth on the structural and electronic properties of a-Si and a-SiGe alloy films has been extensively studied (Knights et al. 1979, Drevillion and Toulemonde 1985, Cabarrocas et al. 1991, Perrin et al. 1989). From the studies of optoelectronic properties of a-Si alloy films deposited under a negative substrate bias, Roca i Cabarrocas et al. (Cabarrocas et al. 1991) reached the conclusion that positive ion bombardment during deposition improves film properties; films with the best electronic properties are obtained at a negative bias of 50 V. Recently, Ganguly and Matsuda reported that by applying a small positive bias to a mesh type controlling electrode in a triode configuration, hole mobility can be improved by orders of magnitude (Ganguly and Matsuda 1994). However, very little has been reported on the effect of ion bombardment on the solar cell performance of a-Si or a-SiGe alloy material.

We present a systematic study of the effect of ion bombardment on both a-Si and a-SiGe alloy solar cells. Samples were deposited by rf plasma-enhanced chemical vapor deposition under both diode and triode configurations. DC bias voltage applied to the substrates was varied from -200 to 50 V to facilitate both electron and ion bombardment.

Experimental

Single-junction a-Si and a-SiGe alloy *p i n* solar cells were deposited in a multichamber reactor using conventional rf plasma-enhanced chemical vapor deposition. In this study, gas mixtures of Si_2H_6+H_2 and Si_2H_6+GeH_4+H_2 were used for a-Si and a-SiGe alloy depositions, respectively. The triode configuration was achieved by introducing a grounded high-purity metal screen to a diode system between the cathode and the substrate. Experiments on the effect of electric bias were carried out by applying a dc electric bias to the substrate in both the triode (with screen) and the diode (without screen) configurations.

Experiments include the following four cases: i) a-Si alloy cells deposited in a triode mode, ii) a-SiGe alloy cells in a triode mode, iii) a-Si alloy cells in a diode mode, and iv) a-SiGe alloy cells in a diode mode. In cases ii) and iii), the cells were deposited on a textured Ag/ZnO back reflector, and the other samples were deposited on stainless steel (ss) without any back reflector. For a-SiGe alloy cells, the concentration of germanium was kept constant throughout the thickness. All the solar cells reported in this work have an active area of 0.25 cm^2.

Results and Discussions on Ion Bombardment Effect

In contrast to the effect of bias on film properties (Cabarrocas et al. 1991, Ganguly and Matsuda 1994), less significant effect is observed on the solar cell performance. Generally, dc bias on the substrates changes the deposition rate in both the diode and triode configurations. Since the deposition rate plays a critical role in determining cell properties (Guha et al. 1992), we adjusted the deposition conditions in order to obtain similar deposition rates.

Triode Configuration

The most significant effect of applying an electric bias was observed in the case of a-Si alloy cells deposited in the triode configuration. A typical example of the bias effect on a-Si alloy cells is shown in Table 3. The thickness and deposition rate are 3000 Å and 1.5 Å/sec, respectively. Also included in Table 3 are the blue and the red fill factors measured using narrow-band-pass filters, centered at 390 and 670 nm, respectively.

As shown in Table 3, an application of positive bias to the substrate improves both the fill factors and open circuit voltage of the cells, while applying a negative bias deteriorates the cell performance. Since the red fill factor, which is mainly determined by bulk properties of the cell, shows the largest effect, it is clear that positive ion bombardment on the growing surface is detrimental to a-Si alloy cells in this deposition configuration.

In the case of a-SiGe alloy cells, we found that a dc bias on the substrate affects both the deposition rate and the Ge content incorporated into the cells. For a given Si_2H_6/GeH_4 ratio in a solar cell configuration, open-circuit voltages turned out to be 0.63, 0.74 and 0.79 volts, respectively, for +50, 0 and -50 volt bias. The Si_2H_6/GeH_4 ratio and rf power were adjusted to keep similar Ge content and deposition rate. As shown in Table 4, with similar Ge content (as monitored by V_{oc}) and deposition rate, the performance of the a-SiGe alloy cells was hardly affected by either positive or negative bias up to a certain value. At large negative biases (-150 to -200 V), the cell performance deteriorates, as mainly reflected in the red fill factors. It should be pointed out that the average thickness of the first three samples is 2500 Å, about 10% thicker than the remaining five samples listed in Table 4.

Diode Configuration

Quite different results were observed when the screen was removed. The effect of bias on a-Si alloy cells in the diode mode are shown in Table 5. Note that the bias of +50 volt increases the deposition rate about 15% while -10 volt bias reduces the rate by ~10%. Except for the different rates due to the bias, there is essentially no difference in cell performance for the three a-Si alloy solar cells. In the case of negative bias, only 10 volts are applied because the plasma could not be sustained with the same power at higher biases.

Similar experiments were also carried out on a-SiGe alloy cells in the diode mode. In this experiment, the a-SiGe alloy cells were deposited on ss without back reflectors. The thickness is around 4000 Å (power was adjusted slightly to maintain similar deposition rates). As shown in Table 6, three a-SiGe alloy cells deposited under different bias voltages have very similar characteristics. In this case also, sustenance of the plasma was problematic at higher voltages and hence, the bias voltage was changed only between -15 to +15 V.

Discussions

Our results indicate that positive-ion bombardment is not beneficial to either a-Si or a-SiGe alloy cells. On the contrary, at high biases positive ion-bombardment is found to affect the cell performance adversely. Note that these results are different from reports from Ganguly and Matsuda (Ganguly and Matsuda 1994) who reported a dramatic improvement in hole mobility of a-Si alloy deposited in a triode system when a small positive bias is applied to the mesh/screen. Turner et al. (Turner et al. 1990) also reported an improvement in the quality of cathode-deposited a-SiGe alloy films which they attributed to the beneficial effect of positive ion bombardment. It has been conjectured that ion bombardments may increase the adatom mobility of the impinging species giving rise to a better material.

Table 3. Bias Effect on a-Si Alloy Cells in Triode Configuration.

Sample No.	Bias (V)	P_{max} (mW/cm^2)	J_{sc} (mA/cm^2)	V_{oc} (volt)	FF (white)	FF (blue)	FF (red)
2636	0	6.77	10.9	0.94	0.66	0.74	0.66
2635	-50	5.68	10.1	0.91	0.61	0.72	0.60
2638	+50	7.49	10.9	0.96	0.72	0.76	0.69

Table 4. Bias Effect on a-SiGe Alloy Cells in Triode Configuration.

Sample No.	Bias (V)	P_{max} (mW/cm^2)	J_{sc} (mA/cm^2)	V_{oc} (volt)	FF (white)	FF (blue)	FF (red)
4232	+50	7.4	19.2	0.71	0.54	0.56	0.59
4223	0	8.2	18.9	0.74	0.58	0.60	0.61
4220	-50	7.9	19.0	0.75	0.56	0.69	0.56
4332	+50	8.2	18.7	0.74	0.60	0.68	0.61
4323	0	8.3	18.4	0.73	0.62	0.68	0.62
4329	-50	8.1	18.7	0.74	0.58	0.69	0.61
4327	-150	7.6	17.9	0.75	0.57	0.67	0.58
4328	-200	7.5	18.1	0.74	0.56	0.67	0.56

Table 5. Bias Effect on a-Si Alloy Cells in Diode Configuration.

Sample No.	Bias (V)	P_{max} (mW/cm^2)	J_{sc} (mA/cm^2)	V_{oc} (volt)	FF (white)	Thickness (nm)
3727	0	9.51	16.1	0.93	0.63	550
3737	+50	9.56	16.6	0.93	0.62	630
3740	-10	9.58	15.9	0.93	0.64	490

Table 6. Bias Effect on a-SiGe Alloy Cells in Diode Configuration.

Sample No.	Bias (V)	P_{max} (mW/cm^2)	J_{sc} (mA/cm^2)	V_{oc} (volt)	FF (white)
3746	0	6.11	15.9	0.71	0.54
3747	+15	6.16	15.5	0.72	0.55
3748	-15	6.00	15.5	0.72	0.54

We believe that the above arguments are valid only if the material quality is less than optimum. The materials used in this study have been optimized using heavy hydrogen dilution which results in a better hydrogen coverage of the growing surface, thus giving rise to an increased adatom mobility. We have shown elsewhere (Guha et al. 1995) that positive ion bombardment indeed has a beneficial effect on a-Si and a-SiGe alloy cells deposited at high rates. These materials have poorer quality since the impinging species do not have enough time to find stable sites. Ion bombardment is expected to increase the adatom mobility, thus giving rise to a superior microstructure. This is, of course, accompanied by bombardment-induced defects; but for poorer quality material, this is offset by the large number of defects inherent in the material.

Note that dc bias also has effect on V_{oc} of a-Si alloy cells made in the triode configuration. A difference of 50 mV in V_{oc} is observed between the cells made with +50 V and -50 V bias. Three factors may cause changes in V_{oc}: a) more hydrogen incorporated into the films in the case of positive bias, b) different interface situations caused by ion bombardment, and c) improved bulk properties due to reduced ion bombardment. From Table 3 we find that the increase in V_{oc} does not cause a lowering of J_{sc} and is accompanied by an increase of FF. It therefore appears that the observed higher V_{oc} is caused by improved bulk properties of a-Si alloy due to reduced ion bombardment.

Preheating Effect of Gas Mixture

In a-Si alloy film deposition, a certain amount of energy is needed for the species to diffuse on the growing surface to find a stable site and form a denser structure. Usually the energy for the species is supplied by heating the substrate to provide thermal energy. However, a very high substrate temperature makes hydrogen evolve from the films, which can deteriorate the a-Si alloy film properties. Another way to provide the species with high thermal energy is to preheat the gas mixtures or species while the substrate temperature is held at 200 ~ 300 °C.

We have carried out two experiments to preheat either the gas mixtures or species during a-Si alloy solar cell deposition. In the first, gases were preheated by heating the gas lines, either outside or in the deposition chamber. For the second experiment, a heated metal mesh (or grid) was installed between the Al screen and the substrate to energize the species (in the triode configuration).

In the heated gas line experiment, no appreciable effect was observed. This result may be limited by the maximum temperature reached in the experiment. Another explanation is that the heated gas molecules may lose their thermal energy by colliding with the walls before they can reach the growing surface. Some typical data are shown in Table 7.

Table 7. Characterization of a-Si Alloy Cells Deposited with and without Preheating of Gas Mixtures. The gas line was heated by a lamp inside the deposition chamber. The cells were made on SS without back reflectors and are 2700 Å thick.

Sample No.	Pre-heating	P_{max} (mW/cm^2)	J_{sc} (mA/cm^2)	V_{oc} (V)	FF
2853	Off	6.62	9.87	0.96	0.71
2856	On	6.57	9.82	0.95	0.70

In the second experiment, either tungsten (W) mesh or W wire grid was installed between the Al screen and the substrate. The W mesh/grid is ~2 cm away from the substrate. It was verified that, without plasma, there was no deposition due to thermal decomposition by only flowing the gas mixtures through the heated W mesh or grid. By increasing the current flowing through the W grids or mesh, fill factors of a-Si alloy cells appear to be slightly improved. An example is presented in Table 8. In contrast, ETL group reported that a significant improvement in a-Si alloy film properties in terms of defect density was observed by constant photocurrent measurement (Ganguly et al. 1994). One may argue that if a-Si alloy films are deposited at nonoptimized conditions such as at low substrate temperatures, or high deposition rates, preheating may be more effective.

Note that no effort has been made to accurately measure the temperature on the metal mesh or grid in our experiments. The current flowing through the mesh for sample 3338 was 6 A. When the current was increased to 20 A, V_{oc} dropped to 0.91 V and FF to 0.60. This indicates that at this high mesh current, there is substantial heating of the substrate. We should also mention that beyond a mesh current of 8 A, the fill factor did not improve any further. The above experiments indicate that there is indeed mesh heating; however, the beneficial effect on the cell properties is negligible.

Table 8. The Effect of Preheating Species by W Grids on a-Si Alloy Cells. The cells are 3000 Å thick.

Sample No.	Pre-heating	P_{max} (mW/cm^2)	J_{sc} (mA/cm^2)	V_{oc} (V)	FF
3335	Off	7.08	10.6	0.97	0.69
3338	On	7.33	10.8	0.96	0.71

Conclusions

A systematic study of electric bias effect on a-Si and a-SiGe alloy solar cells has been carried out in both diode and triode configurations. In the triode mode, an application of positive bias on substrate improves the performance of a-Si alloy cells; zero bias gives best results for a-SiGe alloy cells. In the diode mode, no appreciable bias effect is observed on both a-Si and a-SiGe alloy cells. Also no significant effect of preheating of gas mixture is observed on a-Si alloy cells for both diode and triode modes.

Section 3

Effect of Deposition Parameters on a-Si Alloy Solar Cells

Introduction

In the previous section, we presented the effect of ion bombardment on a-Si alloy solar cells by the application of dc bias voltage to the substrate during deposition. Experimental results showed that in the triode mode, positive bias improves the cell performance slightly, while in the diode mode, there is essentially no effect of bias.

Recently, Ganguly and Matsuda carried out an experiment where the plasma potential was controlled by changing deposition parameters such as the applied power, chamber pressure and the spacing between electrodes (Ganguly and Matsuda 1995). They reported that within a narrow range of plasma potential (ion energy), the room temperature hole drift mobility in a-Si alloy was enhanced by two orders of magnitude. This would, of course, lead to a tremendous improvement in solar cell performance.

Results and Discussion

We have performed a series of experiments on a-Si alloy solar cells where we have varied the deposition parameters. The experiments were carried out in a conventional rf plasma-enhanced CVD system having a diode configuration, and the substrate was grounded instead of being floated as in previous dc bias experiments. The following parameters were varied: pressure, rf power and hydrogen dilution. Figure 1 shows both red FF (open circles) and white FF (solid circles) of a-Si alloy cells as a function of thickness of the intrinsic layer. As expected, the white FF decreases as the cells get thicker, particularly as thickness exceeds 5500 Å. Note that the scatter in the data is caused by the different deposition conditions.

Dependence of a-Si alloy cell performance (for cells with thickness in the range 4600 ± 500 Å) on bias voltage (measured between the cathode and the substrate) and chamber pressure is shown in Figs. 2 and 3, respectively. Although the values of the red FF remain between 0.70 to 0.74, the white FF shows larger fluctuation, scattering from 0.60 to 0.68. The best value of white FF in this group of samples is 0.68, which is comparable to our good baseline value. We thus find that even though we have probed a reasonable range of deposition parameters, we have not been able to achieve the narrow optimum deposition condition under which Ganguly and Matsuda obtained the very high hole mobility.

We note that Ganguly and Matsuda (Ganguly and Matsuda 1995) commented that even under nominally optimal plasma conditions, only about 20% of the samples turned out to be good. Therefore, 16 runs involved in our experiments may not be sufficient to obtain the "extraordinary" results on solar cells.

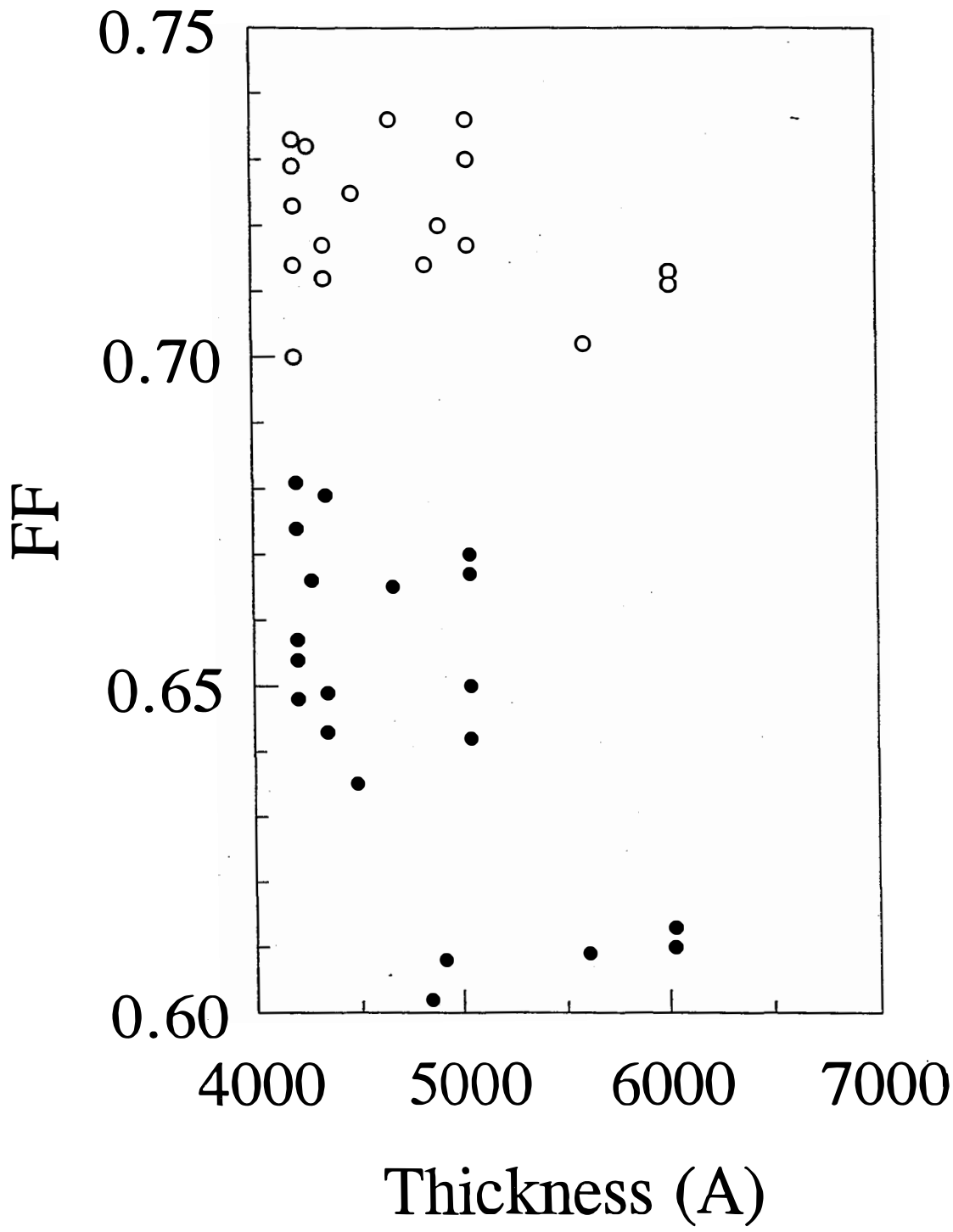

Figure 1. **Red (open circle) and white (solid circle) fill factors of a-Si alloy solar cells versus intrinsic layer thickness.**

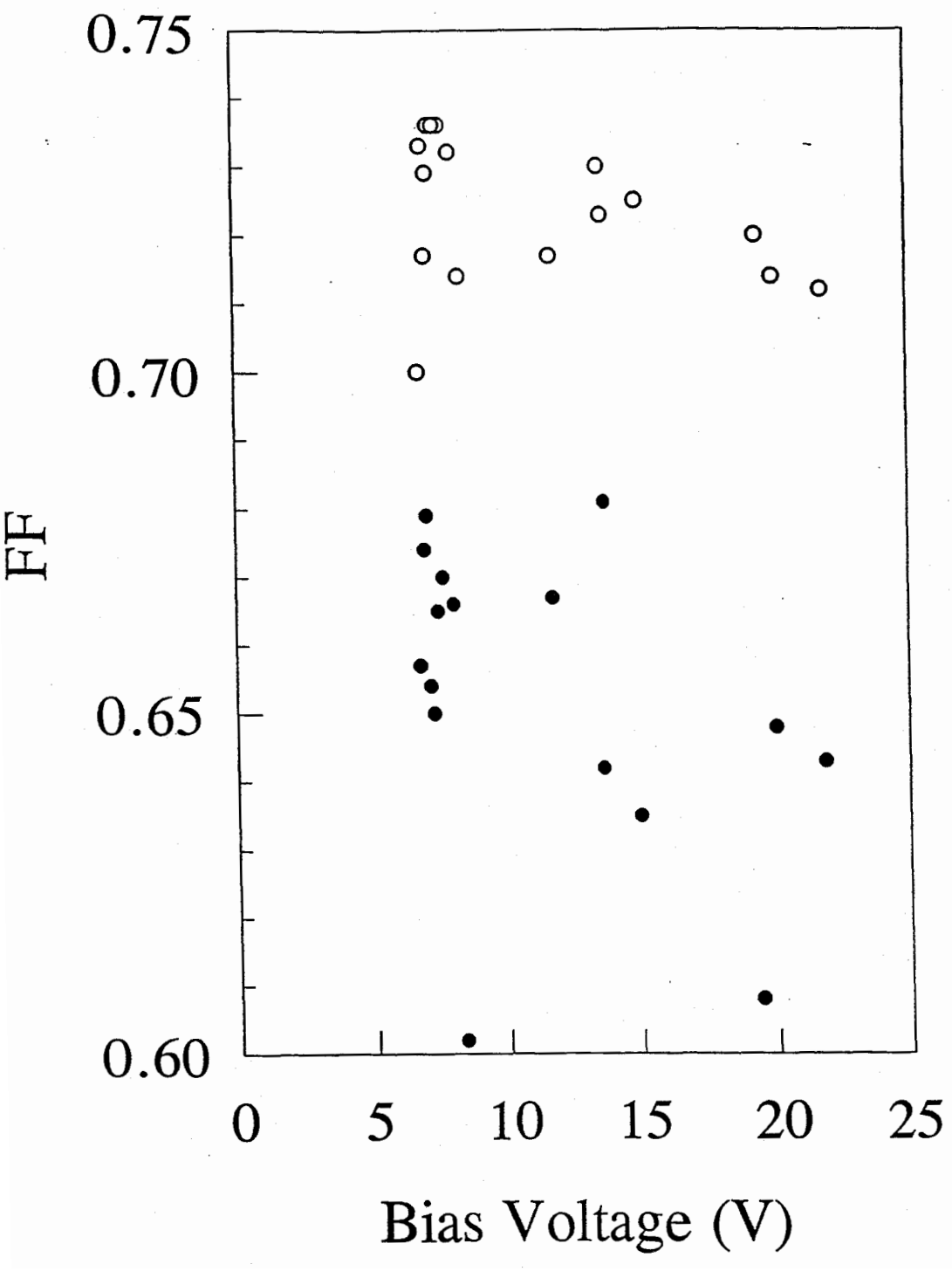

Figure 2. **Red (open circle) and white (solid circle) fill factors of a-Si alloy solar cells versus applied bias voltage.**

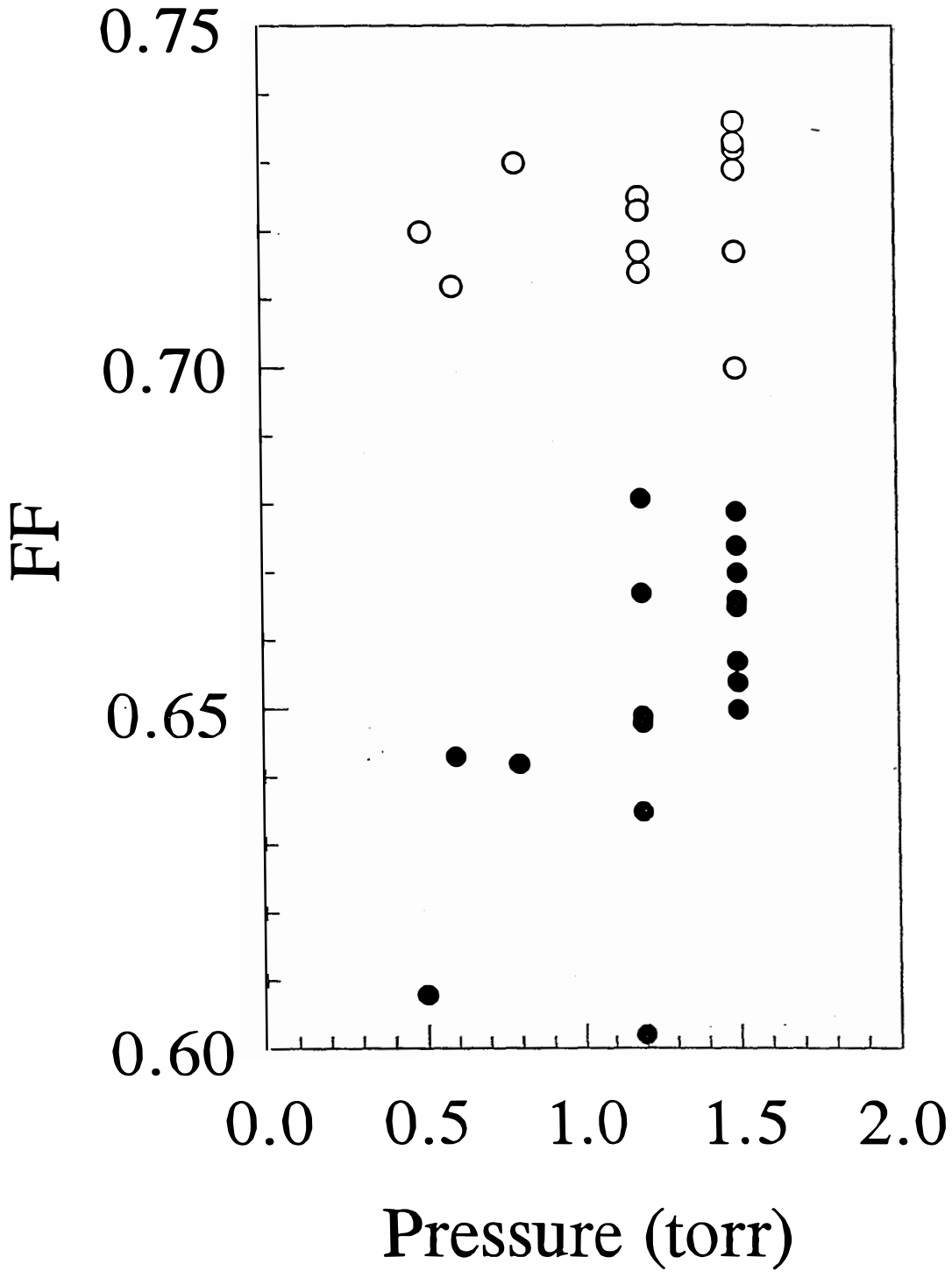

Figure 3. **Red (open circle) and white (solid circle) fill factors of a-Si alloy solar cells versus chamber pressure.**

Section 4

Effect of Discharge Modulation on a-Si Alloy Solar Cells

Pulsed discharge, instead of continuous discharge, has been the subject of several investigations. Yoshida et al. [Yoshida et al. 1989] used it to obtain a high, transient electron energy in the plasma. The technique was also used to increase the doping efficiency for *p*-type amorphous silicon carbon alloys [Yoshida et al. 1990]. Verdeyen et al. (Verdeyen et al. 1990) showed that the amount of dust generated in a pulsed discharge is much lower than in the case for a continuous discharge. They attributed this improvement to the low level of negative ion density in a pulsed discharge. Recently, Gallagher et al. (Gallagher et al. 1996) proposed that the incorporation of silicon particles into amorphous silicon alloy films can affect the electrical quality of the films. They also suggested the use of pulsed discharge or discharge modulation to improve the quality of the material.

In order to investigate the effect of Si-particles' incorporation in a-Si alloy solar cells, we fabricated *p-i-n* a-Si alloy solar cells on stainless steel substrates where intrinsic layers were deposited by using pulsed-rf plasma with period of 1 ms, 10 ms, and 100 ms, and compared the characteristics with those of the reference cells made by continuous rf plasma; the deposition conditions are otherwise the same. The duty cycle of the pulse is fixed at 50% for all experiments.

The initial characteristics of the cells are listed in Table 9. The deposition time is adjusted to obtain the same thickness. We could achieve stable plasma for 1 ms and 10 ms pulses. For the 100 ms pulse, the plasma became unstable after ~8 min of deposition. From Table 9, the characteristics of the cells using pulsed plasma seem to be similar to that by continuous plasma.

Table 9. Cell Characteristics for Different Pulsed Conditions Described in the Text.

Run #	Pulse	i-D time (min)	Thickness (Å)	P_{max} (mW/cm^2)	J_{sc} (Q) (mA/cm^2)	V_{oc} (V)	FF	Blue	Red	Comments
6555	No-)	8.6	2250	7.26	12.21	0.951	0.625	0.754	0.660	
6576	pulse)	8.6	2390	7.28	11.83	0.926	0.665	0.755	0.707	
6567	1 ms)	16	2230	7.06	12.36	0.941	0.607	0.753	0.650	
6592	pulse)	17.5	2200	6.77	12.07	0.920	0.610	0.739	0.639	
6566	10 ms pulse	13	2280	6.89	11.66	0.944	0.626	0.747	0.667	
6553	100 ms pulse	13	2360	7.59	12.22	0.944	0.658	0.764	0.700	plasma unstable

We also adjusted the rf power to obtain the same *i*-layer thickness for no pulse, 1 ms, and 100 ms pulses while keeping the deposition time constant. The initial characteristics are listed in Table 10. This result also shows that there is no observable difference between pulsed plasma and continuous plasma.

Table 10. Cell Characteristics for Different Pulsed Conditions Described in the Text.

Run #	Pulse	i-D:time (min)	Temp. (°C)	Thickness (Å)	P_{max} (mW/cm²)	J_{sc}(Q) (mA/cm²)	V_{oc} (V)	FF	Blue	Red
6534	No-Pulse	7	300	1530	6.56	9.87	0.959	0.693	0.753	0.713
6538	1 ms Pulse	7	300	1650	6.86	10.19	0.957	0.703	0.762	0.712
6539	100 ms Pulse	7	300	1620	6.38	9.47	0.961	0.701	0.754	0.712

Section 5

Effect of H_2 and He Dilution on a-Si and a-SiGe Alloy Materials and Solar Cells

Introduction

Hydrogen dilution is known to improve the material quality of a-Si alloys by controlling the growth kinetics (Guha et al. 1981, Tanaka and Matsuda 1987, Doughty et al. 1990). Guha et al. observed that films grown using 10% silane (SiH_4) and 90% hydrogen (H_2) exhibited improved stability against prolonged light soaking when compared with films grown using pure SiH_4 (Guha et al. 1981). We have reported that by using high hydrogen dilution with optimized preparation conditions, improved performance is achieved for both a-Si and a-SiGe alloy solar cells (Yang et al. 1994-1, Yang et al. 1994-2).

In order to understand the physics behind the improved device performance, we have carried out extensive studies on materials properties of a-Si and a-SiGe alloy films deposited with different levels of hydrogen dilution and at different temperatures. Material characterizations employed in this work include constant photocurrent measurement (CPM), infrared (IR) absorption, hydrogen evolution, small angle x-ray scattering (SAXS), and primary photocurrent measurements (PPC). Light-induced degradation studies on a-Si and a-SiGe alloy solar cells with different levels of hydrogen dilution have also been carried out. Also presented are experimental results on He dilution effect on a-Si alloy solar cells.

Experimental

In the studies on hydrogen dilution effect, Si_2H_6-H_2 and Si_2H_6-GeH_4-H_2 gas mixtures were used to deposit a-Si and a-SiGe alloy films, respectively. Two Si_2H_6/H_2 ratios and two substrate temperatures were used for a-Si alloy deposition, while a-SiGe alloy films were deposited at 300 °C with two levels of hydrogen dilution. The films were grown on 7059 glass for optical and electrical characterization, on crystalline Si (c-Si) for infrared analysis, on stainless steel (ss) and c-Si for hydrogen evolution, and on Al foil for small angle x-ray scattering measurements.

Both a-Si and a-SiGe alloy single-junction *p i n* solar cells were deposited on ss without any back reflector. The thicknesses of the intrinsic layers are ~5000 Å and ~4000 Å for a-Si and a-SiGe alloy solar cells, respectively. For stability studies, the cells were exposed to one sun white light in open-circuit mode at 50 °C for over 1000 hours.

Results of H_2 Dilution Effect

The main characteristics of six a-Si and a-SiGe alloy samples used in this work are listed in Table 11. Except for sample #3, all the other a-Si alloy samples have similar values of dark-conductivity, σ_d, (~1×10^{-11} s/cm), and electron mobility-life time product, $\mu\tau$, measured with a flux of 5×10^{15} photons/cm^2 at 650 nm. High hydrogen diluted samples show slightly larger values of activation energy (E_a) of dark conductivity and broader optical ("Tauc") gap (E_{opt}). Similar trend is also observed for a-SiGe alloy films where the high hydrogen diluted sample shows slightly higher E_a, $\mu\tau$ and E_{opt}.

Table 11. Main Characteristics of a-Si and a-SiGe Alloy Films.

Sample No.	E_{opt}(eV)	C_H(%)	E_a(eV)	σ_D ($\Omega^{-1}cm^{-1}$)	$\mu\tau$ (cm^2V^{-1})	Notes
#1	1.72	8.1	0.97	1.1e-11	1.3e-6	a-Si, 300 °C, low H_2 dilution
#2	1.74	7.4	1.00	0.9e-11	1.0e-6	a-Si, 300 °C, high H_2 dilution
#3	1.77	13.2	0.93	1.3e-10	0.9e-6	a-Si, 175 °C, low H_2 dilution
#4	1.79	12.3	1.04	1.1e-11	1.6e-6	a-Si, 175 °C, high H_2 dilution
#5	1.40	6.4	0.71	2.4e-9	1.3e-7	a-SiGe, 300 °C, low H_2 dilution
#6	1.43		0.79	1.2e-9	2.1e-7	a-SiGe, 300 °C, high H_2 dilution

Sub-bandgap Absorption

Sub-bandgap absorption measured by CPM on the films prepared under different conditions shows little difference (within measurement error). All the four a-Si alloy samples had similar Urbach energy of 47 to 49 meV. The sub-bandgap absorption data are summarized in Table 12. In the initial state, the defect density for films deposited at a given temperature is within a factor of 2 from each other; the values are even closer for the degraded state. However, spectral response measured by PPC on the four a-Si alloy solar cells shows larger difference in the light-soaked state with sample #3 (deposited at 175 °C with low dilution) showing the highest defect density.

Table 12. Data Obtained from CPM and PPC.

Sample No.	E_u (meV) (CPM)	$N_{s,initial}$ (CMP) (cm^{-3})	$N_{s,degraded}$ (CPM) (cm^{-3})	$QE(1.2eV)_{initial}$ (PPC) (a.u.)	$QE(1.2eV)_{degraded}$ (PPC) (a.u.)
#1	47	2.9e15	2.9e16	1.1	8.1
#2	47	4.4e15	3.0e16	1.0	5.8
#3	49	7.9e15	3.0e16	1.1	14.8
#4	48	5.0e15	2.5e16	1.0	6.2
#5	52	6.4e15			
#6	52	4.0e15			

IR Analysis

As shown in Table 11, total hydrogen concentrations (determined from 630 cm^{-1} mode) for the a-Si alloy films for the two different dilutions are very similar. However, IR spectra in the range of 800 to 960 cm^{-1} reveal dramatic differences. Figure 4 compares IR absorption spectra in this range for the four a-Si alloy samples. For all the samples, there is an absorption peak around 880 cm^{-1} which can be attributed to the bending mode of SiH_2 (Knights et al. 1978). However, sample #3 shows a doublet at 880 and 845 cm^{-1} indicating presence of $(SiH_2)_n$ in this sample. Note that sample #4 shows an absorption peak around 915 cm^{-1} to which we do not have satisfactory attribution.

Hydrogen Evolution

For a-Si alloy samples, hydrogen evolution experiments show that there are sharp peaks at low temperature for the samples prepared with high H_2 dilution. For the pair of a-Si alloy samples deposited at 300 °C, as shown in Fig. 5, sample #1 shows a main peak around 500 °C, while sample #2 has a strong and sharp peak around 400 °C. For the other pair of a-Si alloy samples deposited at 175 °C, low dilution one (#3) shows three small peaks from 400 to 600 °C and the high dilution sample (#4) shows two sharp peaks around 400 and 500 °C.

In contrast to a-Si alloy, there is no appreciable difference in hydrogen evolution spectra for a-SiGe alloy samples deposited with low and high H_2 dilution. Both samples show a broad peak between 350 to 550 °C with three fine structures at ~380, 440 and ~480 °C.

SAXS

The SAXS data show that high H_2 dilution tends to form more anisotropic microstructure with columns parallel to the growth direction. The SAXS of the a-Si alloy sample deposited at 175 °C with low H_2 dilution (#3) is isotropic, and can be modeled with spherical voids averaging near 1 nm in diameter, while the SAXS data for the other three a-Si alloy samples (#1, #2 and #4) are anisotropic, showing columnar-like microstructures (Williamson 1995).

In the case of a-SiGe alloy films, both the samples show columnar-like features in SAXS data. However, the sample made with high dilution exhibits stronger tilting effect than the sample made with low dilution, which indicates the existence of larger size of oriented microstructures in the high dilution sample.

Stability of Solar Cells

Both a-Si and a-SiGe alloy cells deposited with high hydrogen dilution not only show improved performance in the initial state but also maintain superior performance in the light-soaked state. The characteristics of six solar cells with i-layers deposited under nominally identical conditions to the six samples in Table 11 are presented in Table 13. It can be seen that the a-Si alloy cell deposited at 175 °C with low hydrogen dilution degraded by 43%, much more than the other three a-Si alloy cells (16 to 23%). High hydrogen dilution has similar effect on a-SiGe alloy solar cells. The high dilution sample has superior performance in the initial state and is also more stable than the low dilution sample.

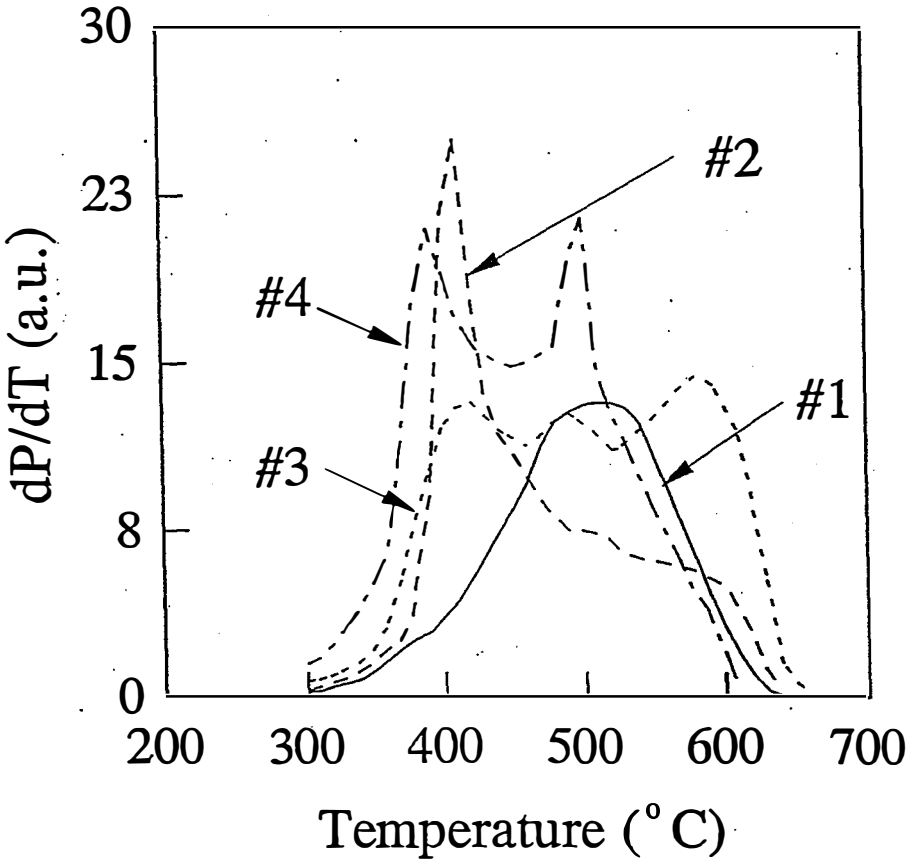

Figure 4. IR spectra of four a-Si alloy samples.
Refer to Table 11 for sample description.

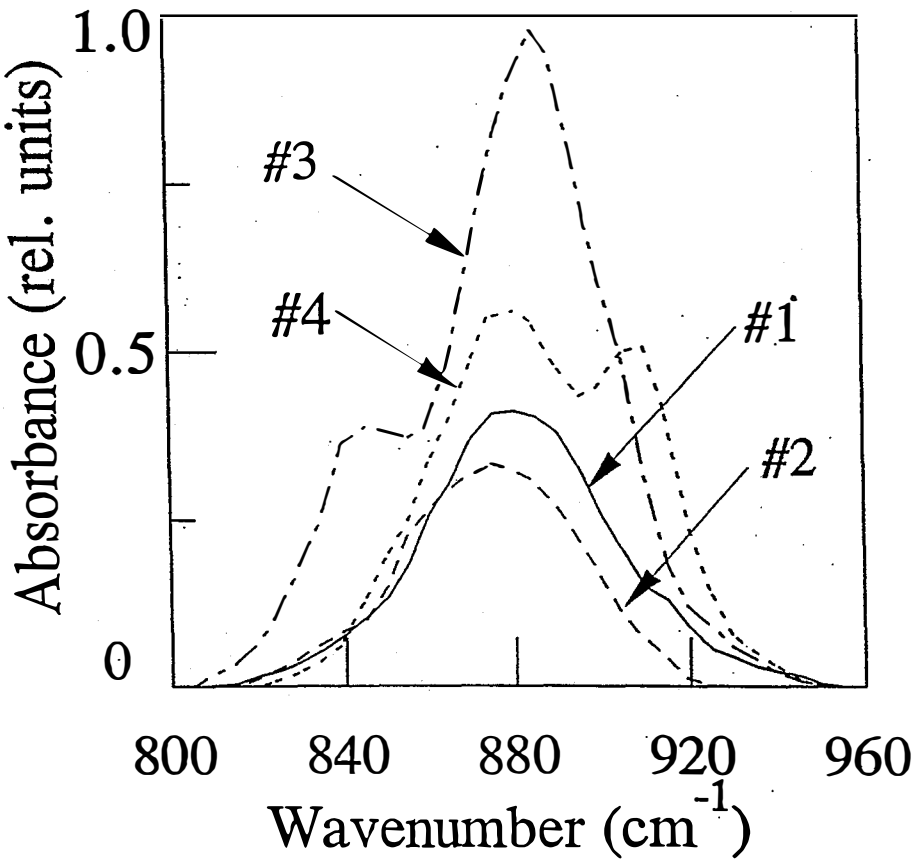

Figure 5. Hydrogen evolution spectra for four a-Si alloy samples. Refer to Table 11 for sample description.

Table 13. Characteristics of a-Si and a-SiGe Alloy Cells In Both Initial and Degraded States.

Description	State	J_{sc} (mA/cm^2)	V_{oc} (volt)	FF	P_{max} (mW/cm^2)
300 °C, Low Dilution	Initial	12.3	0.94	0.65	7.5
	Degraded	11.6	0.91	0.55	5.8
	% Degradation				23
300 °C, High Dilution	Initial	11.6	0.96	0.68	7.6
	Degraded	11.2	0.94	0.61	6.4
	% Degradation				16
175 °C, Low Dilution	Initial	11.4	0.96	0.64	7.0
	Degraded	9.5	0.91	0.46	4.0
	% Degradation				43
175 °C, High Dilution	Initial	10.9	1.00	0.69	7.5
	Degraded	10.5	0.97	0.60	6.1
	% Degradation				19
a-SiGe, Low Dilution	Initial	17.6	0.72	0.55	7.1
	Degraded	14.9	0.64	0.41	3.9
	% Degradation				45
a-SiGe, High Dilution	Initial	18.0	0.74	0.59	8.0
	Degraded	16.3	0.69	0.45	5.1
	% Degradation				36

Discussions on H_2 Dilution

As the H_2 dilution ratio during a-Si alloy film deposition increases, more oriented microstructures are created while the density of isotropic nanovoids (~ 1 nm in diameter) is reduced (more significantly in the low temperature case). Hydrogen associated with these oriented microstructures in high H_2 dilution samples tends to evolve out within a narrow temperature range at low temperature, corresponding to sharp peaks observed around 400 °C in H_2 evolution spectra of samples #2 and 4. However, these hydrogen atoms are not bonded in $(SiH_2)_n$ structures since in IR spectra the high dilution samples show less signals at 845 cm^{-1} and 880 cm^{-1} than the low dilution samples. The only exception is sample #1 (300 °C, low H_2 dilution); there is no low temperature peaks observed in H_2 evolution experiment although this sample does show evidence of oriented microstructures.

Correlation between SAXS data and solar cell performance is worthy of more discussions. It has been found that nanostructure in the form of 1 to 4 nm voids or H-rich clusters are harmful to solar cell performance (Knights et al. 1978, Williamson 1995). Williamson suggested that since the oriented microstructures observed in high H_2 dilution samples are parallel to the solar cell transport direction, they may not be detrimental to cell performance. However, why does the existence of these oriented microstructures improve the cell performance, particularly in the degraded state? Of particular importance is to clarify whether high hydrogen dilution creates more ordered microstructures which may enhance the transport properties in solar cells.

Regarding the sub-bandgap absorption of a-Si alloy material and solar cell performance, there is still no satisfactory correlation. We have previously reported on the lack of correlation between CPM data and solar cell performance (Guha et al. 1992, Xu et al. 1993). Although PPC results showed a better correlation with cell performance, more experiments will be necessary before PPC can be used as a tool for cell evaluation.

He Dilution Effect on a-Si Alloy Cells

It has been reported that highly photosensitive low bandgap (~1.5 eV) a-Si alloy can be obtained by using helium dilution of process gases in plasma-enhanced CVD in a certain optimum pressure range (Hazra et al. 1995). Low bandgap of a-Si alloy films was said to be caused by reducing the bonded hydrogen content. Compared with a-SiGe alloy film with similar bandgap, low bandgap a-Si alloy films showed higher $\mu\tau$ product and photosensitivity values (Hazra et al. 1995).

We have carried out experiments to study the effect of He dilution on a-Si alloy solar cells. Characteristics and deposition parameters for He-diluted a-Si alloy cells are summarized in Table 14. The only change in deposition parameters for all the runs is the pressure which varied from 0.8 to 2.0 torr. The deposition rate increases from 0.80 Å/s to 1.7 Å/s as the pressure increases from 0.8 to 1.6 torr and comes down slightly to 1.4 Å/s at 2.0 torr. Up to 1.8 torr, there is essentially no difference in V_{oc}, and the variation in FF is caused by the difference in thickness. However, the cell deposited at 2.0 torr shows poorer FF and slightly lower V_{oc}, which indicates that the quality of the material is inferior.

In order to find out whether He dilution affects the bandgap of a-Si alloy film, we deposited He-diluted a-Si alloy films on glass substrate at different pressures. The difference in optical gap for these three a-Si alloy films deposited at 1.2, 1.8 and 2.0 torr is less than 0.04 eV (1.72~1.76 eV). This is consistent with the results of cells listed in Table 14 where we find only small changes in the magnitude of V_{oc}.

Except for different deposition rate and inferior performance at the highest pressure, He dilution has no effect on a-Si alloy solar cells made in our conventional rf PECVD system. The optical gap remains to be around 1.74 eV. However, geometrical factors of electrodes such as electrode configuration and separation may play an important role in a-Si alloy film deposition. Without knowing the geometry of the system used in the work of Hazra et al. (Hazra et al. 1995), we can not make a definite conclusion about those results of He dilution effect on a-Si alloy film performance.

Table 14. Characteristics of He-diluted a-Si Alloy Cells Deposited at Different Pressures.

Run No.	Pressure (torr)	J_{sc}	V_{oc}	FF	d(Å)	Dep.Rate (Å/s)
4747	0.8	12.4	0.93	0.68	1900	0.79
4711	1.2	14.1	0.94	0.65	2700	1.1
4720	1.6	14.4	0.93	0.58	4100	1.7
4712	1.8	15.3	0.93	0.59	3800	1.6
4715	2.0	14.6	0.89	0.42	3300	1.4

Conclusions

Our results show that measurements on a-Si and a-SiGe alloy films in the co-planar configuration, such as $\mu\tau$ product and CPM, are not sufficient to predict solar cell performance which depends mainly on properties in the transverse direction. The existence of the oriented microstructures associated with low-temperature hydrogen evolution in both high H_2 dilution a-Si and a-SiGe alloy materials is not necessarily deleterious to solar cell performance. In fact, cells made with high H_2 dilution show the best stable performance. He dilution is found to have no effect on the optical gap of a-Si alloys. In contrast to expectation from published work (Hazra et al. 1995), a-Si alloy films grown under He-dilution do not seem to have the desired quality to be used for low bandgap component cells.

Section 6

Effect of Hydrogen Effusion on a-Si Alloy Solar Cells

As discussed in the previous section, amorphous silicon alloy solar cells prepared with high hydrogen dilution have been found to be more stable than those prepared with low dilution. Films with high dilution also exhibit a sharp peak at low temperature (400 °C) in hydrogen effusion spectra. To study the effect of hydrogen effusion on solar cell performance, we have prepared two sets of a-Si alloy *p i n* solar cells on ss with high and low hydrogen dilutions. In the high dilution case, we prepared one cell with standard procedures and two other cells in which the sample temperature was raised to 400 °C at two different rates after the *i* layer deposition. In the low dilution case, only one effusion sample and one standard sample were prepared. The results are summarized in Table 15.

Table 15. Initial Characteristics of a-Si Alloy *p i n* Solar Cells with and without Hydrogen Effusion Prepared with High and Low Hydrogen Dilution.

Run #	H_2-Effusion after *i* dep.	P_{max} (mW/cm^2)	J_{sc} (mA/cm^2)	V_{oc} (V)	FF	Thickness (Å)	Notes
6424	**No**	6.60	8.52	1.014	0.764	1250	*i* dep. temp.: 150°C
6422	H_2-Effusion (1)	6.65	9.09	0.985	0.743	1170	**High H-dilution**
6423	H_2-Effusion (2)	6.56	8.84	0.990	0.750	1230	For all samples
6431	**No**	5.43	7.38	0.983	0.746	1020	*i* dep. temp.: 200°C
6430	H_2-Effusion (1)	5.03	7.16	0.961	0.731	950	**Low H-dilution** For both samples

Condition of H_2-Effusion after *i*-layer deposition

H_2-Effusion (1): Temperature increased at 10 °C/6 min up to 400 °C (similar to earlier hydrogen effusion experiment).

H_2-Effusion (2): Temperature increased up to 400 °C rapidly, then maintained at 400 °C for 15 min.

We observed that

1. For the cells with high hydrogen dilution, hydrogen effusion after *i* layer deposition under H_2-Effusion (1) condition gives lower V_{oc} and FF but higher J_{sc}, resulting in similar efficiencies (6422-6424). On the other hand, for cells with low dilution, all characteristics seem to become poorer with hydrogen effusion (compare 6430 to 6431). It is interesting to note that highly diluted cells after hydrogen effusion give rise to higher J_{sc} although the low dilution cell did not show this behavior. It should also be pointed out from our earlier experiments that low hydrogen dilution film did not show sharp H_2 effusion peak at low temperatures.

2. More hydrogen is effused out by using H_2-Effusion (1) than H_2-Effusion (2).

As shown in Table 16, light-soaking experiments show that cells with H_2-effusion after *i*-layer deposition have higher degradation than the one without H_2-effusion as reflected in the fill factor. It appears that hydrogen in the film which is effused out at lower temperature (~400 °C) affects cell stability. We do not know if the effused-out hydrogen is bonded or nonbonded. More experiments are certainly needed to understand the effect of hydrogen effusion on cell performance.

Table 16. Light Soaking Behavior of Cells with and without Hydrogen Effusion.

Run #	H_2-Effusion after *i* dep.	State	P_{max} (mW/cm^2)	J_{sc} (mA/cm^2)	V_{oc} (V)	FF	Thickness (Å)
6424	No	Initial	6.60	8.52	1.014	0.764	1250
		Stable (1010 hrs)	5.63	8.17	0.977	**0.705**	
		Degradation	15%	4%	4%	8%	
6422	H_2-Effusion (1)	Initial	6.65	9.09	0.985	0.743	1170
		Stable (1010 hrs)	5.45	8.66	0.940	**0.670**	
		Degradation	18%	5%	5%	10%	
6423	H_2-Effusion (2)	Initial	6.56	8.84	0.990	0.750	1230
		Stable (1010 hrs)	5.42	8.50	0.948	**0.673**	
		Degradation	17%	4%	4%	10%	

See Table 15 for H_2-Effusion (1) and H_2-Effusion (2) conditions.

Section 7

Band Discontinuity Effect on a-Si and a-SiGe Alloy Solar Cells

Introduction

Microcrystalline (μc) boron-doped silicon layers (Guha et al. 1986) play a key role in the improvement of the efficiency of a-Si alloy cells. As compared to their amorphous counterpart, μc *p*-type layers show lower conductivity activation energy and higher optical transmission, giving rise to higher open-circuit voltage (V_{oc}) and short-circuit current density (J_{sc}) for the solar cell. The properties of the thin *p*-type μc layer used in the cell, however, are not very well understood. Specifically, not much information is available regarding the bandgap of the layer and the band edge discontinuities at the *p*(μc)-intrinsic(*i*) a-Si alloy interface. This information is extremely important for reliable numerical simulation of the device performance starting from fundamental material parameters.

Although very little information is available regarding the μc-Si/a-Si alloy interface, several contradictory reports have been made on the band edge discontinuities between crystalline silicon (c-Si) and the a-Si alloys (Evangelisti 1985, Matsuura and Okushi 1992, Mimura and Hatanaka 1987, Cuniot and Marfaing 1988). From the measurement of the internal photoemission (IPE) at a c-Si/a-Si alloy heterojunction, Mimura and Hatanaka (Mimura and Hatanaka 1987) concluded that the major band edge discontinuity occurs in the valence band ($\Delta E_v = 0.71$ eV), while it is only 0.09 eV in the conduction band (ΔE_c). Cuniot and Marfaing (Cuniot and Marfaing 1988), on the other hand, used a structure of c-Si/sputtered a-Si alloy for IPE measurement and found that the discontinuity in the valence band is negligible, with the main discontinuity existing in the conduction band. We take ΔE_v to be positive when the valence band edge for μc- or c-Si lies above that for a-Si or a-SiGe alloy in the electron energy diagram (Fig. 6). The opposite is the case for ΔE_c; i.e., ΔE_c is positive when the conduction band edge for μc- or c-Si lies below that for a-Si alloy or a-SiGe alloy (Fig. 6). We present new experimental results of IPE measurements on μc-Si/a-Si alloy structures and discuss the effect of band edge discontinuities on a-Si and a-SiGe alloy solar cell performance.

Experimental

The samples for the internal photoemission measurement were deposited on specular stainless steel (ss) substrates without back reflectors. The structure of samples used to measure ΔE_v is ss/*p* μc-Si (600 Å)/*i* a-Si (100 - 400 Å)/*n* a-Si (~100 Å) (#1 and 2 of Table 17). The intrinsic a-Si alloy layer was grown by rf plasma-enhanced chemical vapor deposition using a disilane-hydrogen mixture. Hydrogen diluted silane was used for μc-Si alloy layer deposition. BF_3 and PH_3 were added as dopants for *p* and *n* type doping, respectively.

A semitransparent Au or Al front electrode was evaporated on top of the sample to form an Ohmic contact. The monochromatic exciting light of varying wavelength was incident on the front metal electrode. A reverse bias of 50 mV was applied for collecting the photo-generated carriers.

For cell performance studies, a-Si and a-SiGe alloy solar cells were deposited on ss substrates without back reflectors. The structure of the cells is ss/*n*/*i* a-Si alloy (or a-SiGe alloy)/*p* μc-Si/ITO. The thicknesses of the intrinsic layers are 5000 and 3700 Å for a-Si and a-SiGe alloy cells, respectively.

Table 17. Sample Structures for Internal Photoemission Measurement and Observed Threshold Energies.

Sample No.	Structure	E_t (eV)
1	ss/*p* μc-Si (600 Å)/*i* a-Si (400 Å)/*n* a-Si (100 Å)/Au	1.68
2	ss/*p* μc-Si (600 Å)/*i* a-Si (100 Å)/*n* a-Si (100 Å)/Au	1.57
3	ss/*n* a-Si (200 Å)/*i* a-Si (1000 Å)/*p* μc-Si (100 Å)/ITO	1.74
4	ss/*n* μc-Si (600 Å)/*i* a-Si (100 Å)/*p* μc-Si (100 Å)/Al	1.85

Determination of ΔE_v and ΔE_c

According to Kane's model (Kane 1962) for indirect transitions from semiconductors, the quantum yield Y of internal photoemission in the vicinity of the threshold energy (E_t) can be expressed as

$$Y \sim (h\nu - E_t)^{5/2} \quad (1)$$

where $h\nu$ is the energy of photons. The internal photoemission process in the ss/*p* μc-Si/*i* a-Si/*n* a-Si/Au sample can be described as follows. The photons that are transmitted through the metal electrode and the thin *n* and *i* layers are partially absorbed in the μc-Si alloy layer. The electrons are photoemitted from the valence band of μc-Si alloy to the conduction band of a-Si alloy (see Fig. 6). The threshold energy, E_{t1}, is the sum of the bandgap, E_g (μc-Si), of μc-Si alloy, and ΔE_c. Since both *i* and *n* layers are very thin, the predominant contribution to the photocurrent is due to the transition from the valence band of μc-Si alloy to the conduction band of the intrinsic a-Si alloy.

The 2/5 power of the photoemission quantum yield Y is plotted against the photon energy in Fig. 7 for two samples with different thicknesses of the intrinsic a-Si alloy layer (#1 and 2 of Table 17). As seen in Fig. 7, $(Y)^{2/5}$ becomes more linear with $h\nu$ when the *i* a-Si alloy layer becomes thinner. For sample #2 with a 100 Å thick *i* layer, a good linear relationship is observed in the range of 1.7 to 2.4 eV. The threshold energy, E_{t1}, is obtained by extrapolating the straight line to the intercept; and 1.57 eV is obtained for sample #2. For the sample with the 400 Å thick *i* a-Si alloy layer (sample #1), the contribution of the photogenerated carriers from the *i* layer is not negligible and the intercept energy shifts to around 1.68 eV, which is close to the "threshold energy" of 1.74 eV obtained from 1000 Å thick *i* layer using the configuration of sample #3, i.e., simply the gap energy of a-Si alloy.

We performed similar experiments to determine the discontinuity of the conduction band edge between μc-Si and a-Si alloy layers using the structure #4 of Table 17, ss/*n* μc-Si (600 Å)/*i* a-Si (100 Å)/*p* μc-Si (100 Å)/Al. In this case, the threshold energy corresponds to the transition from the top of the valence band of a-Si alloy to the bottom of the conduction band of *n* μc-Si alloy. This threshold energy, E_{t2}, which is the sum of E_g(μc-Si) and ΔE_v, is ~1.85 eV (see Fig. 7).

The discontinuities in both the valence and the conduction band edges between μc-Si and a-Si alloy can be determined if the value of the mobility gap of a-Si alloy is known. Lee et al. measured the mobility gap by internal photoemission (Lee et al. 1990). Chen and Wronski reinterpreted these data and recommended a value for the mobility of 1.83 eV (Chen and Wronski 1995). Using the values of E_{t1} and E_{t2} obtained from Fig. 7, we can calculate that

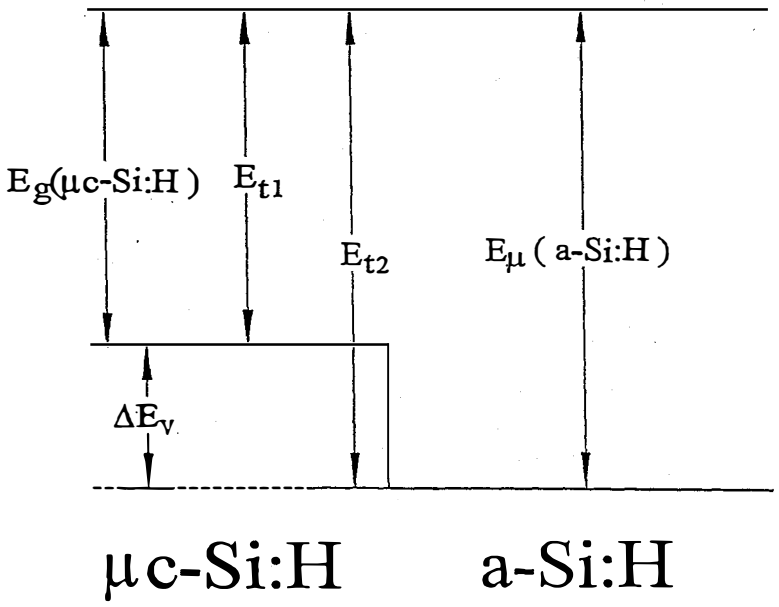

Figure 6. Schematic band diagram of the μc-Si/*i* a-Si alloy heterostructure.

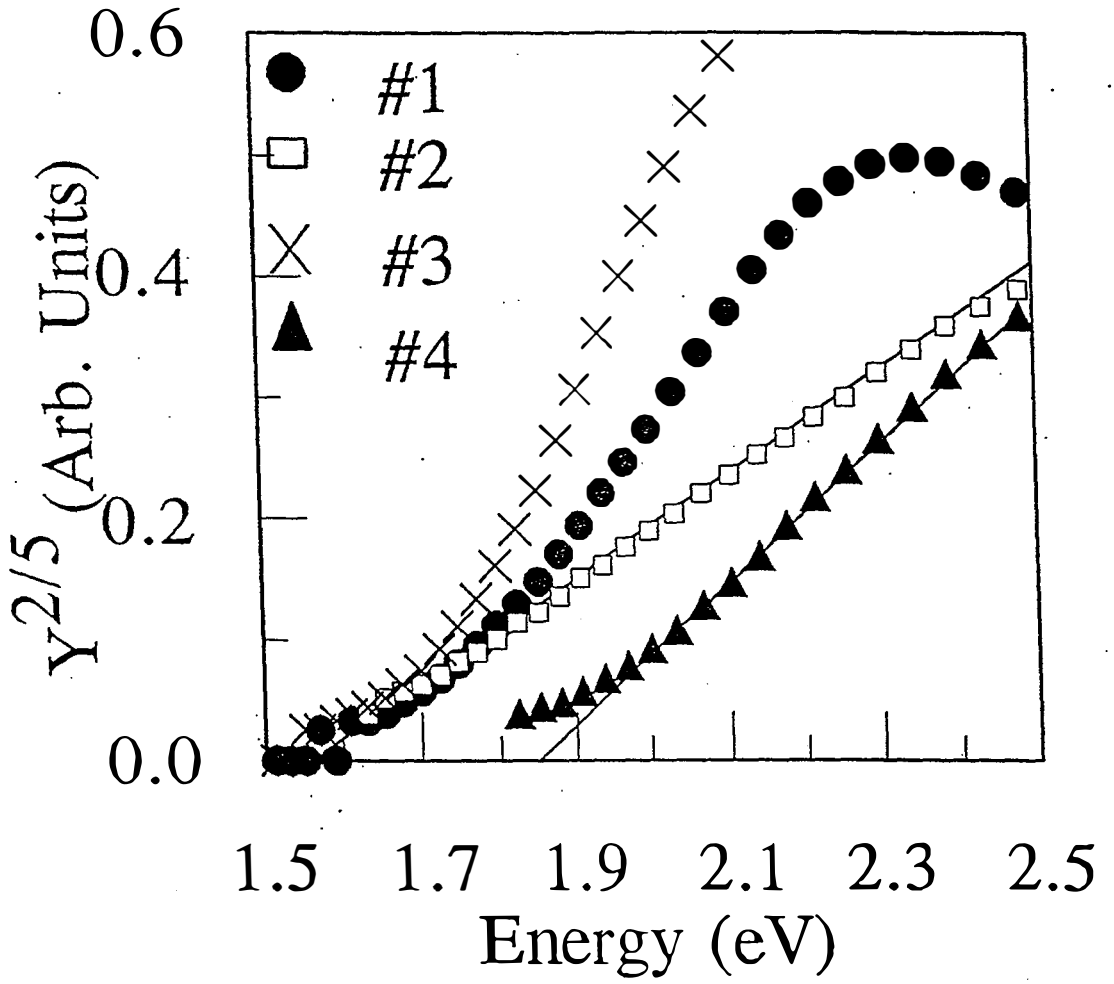

Figure 7. **$(Y)^{2/5}$ versus photon energy *hν* for four samples.** The lines are eye guide.

$$\Delta E_v = E_\mu(\text{a-Si}) - E_{t1} = 1.83 - 1.57 = 0.26 \text{ eV} \quad (2)$$

$$\Delta E_c = E_\mu(\text{a-Si}) - E_{t2} = 1.83 - 1.85 = -0.02 \text{ eV} \quad (3)$$

$$E_g(\mu\text{c-Si}) = E_\mu(\text{a-Si}) - \Delta E_c - \Delta E_v = 1.83 + 0.02 - 0.26 = 1.59 \text{ eV} \quad (4)$$

The observation of an electrical bandgap of ~1.6 eV for the μc-Si alloy merits some discussion. Single crystal silicon has a bandgap of 1.1 eV. It is, however, well known that for nano-crystalline silicon the bandgap increases as the cluster size decreases (Delley and Steigmeier 1993). Our earlier studies on μc-films using transmission electron microscopy (TEM) show a grain size between 70-100 Å and a crystalline volume fraction of 80%. Reflection high energy electron diffraction (RHEED) studies also confirm the existence of microcrystallinity in the thin p layers used in *p i n* solar cell configuration. Using the theoretical calculation of Delley and Steigmeier (Delley and Steigmeier 1993), who computed the bandgap of nano-crystalline Si as a function of cluster diameter using the density-functional approach for finite structures, we find a bandgap in the range of 1.5 to 1.6 eV for a cluster size of 70 Å. This value is in good agreement with our observations.

Effect on a-Si Alloy Cells

To study the effect of band edge discontinuities on a-Si and a-SiGe alloy solar cells with *p* μc-Si alloy layers, we have carried out numerical simulations using the AMPS model developed at Penn State University (Arch et al. 1991). Calculated a-Si alloy cell characteristics are tabulated in Tables 18 and 19, and compared with experimental results. Table 18 shows that V_{oc} increases (i) as the bandgap of the microcrystalline material increases and (ii) as the discontinuity at the valence band edge decreases. This is understandable since, in both of these cases, the built-in potential increases. We also find very good agreement between theory and experiment (case #3) when the measured values of E_g, ΔE_v, and ΔE_c, as obtained from the IPE measurements, are used in the numerical simulations.

Table 18. Simulated and Measured a-Si Alloy Cell Characteristics.
A value of 1.83 eV is used for the mobility gap of a-Si alloy in the simulation.

E_g(μc-Si) (eV)	$\Delta E_c/\Delta E_v$ (meV)	V_{oc} (V)	FF	Case #
1.90	-35/-35	0.99	0.69	1
1.59	240/0	0.98	0.68	2
1.59	0/240	0.93	0.66	3
1.10	60/670	0.53	0.59	4
Measured		0.93	0.65	

Table 19 shows the effect of bandgap of the *p* μc-Si alloy layer and the band edge discontinuities on the ratio of quantum efficiency, i.e., quantum efficiency under -3 V bias to that without bias, Q(-3 V)/ Q(0V), which reflects the loss of carrier collection (Banerjee et al. 1995). In this case also, use of a bandgap of 1.1 eV (that for crystalline silicon) gives a poor fit to the experimental results. The best fit is obtained when the bandgap is taken to be 1.59 eV, and the band discontinuity is assumed to be in the valence band (case #3). This is consistent with the results from IPE measurement.

Table 19. Ratio of Q(-3 V), Quantum Efficiency under -3 V Bias, to Q(0 V), with No Bias, for a-Si Alloy Cells as a Function of Wavelength.

E_g(μc-Si) (eV)	$\Delta E_c/\Delta E_v$ (meV)	λ (nm)	[Q(-3 V)/Q(0 V) - 1]×100 (%) 400	500	600	700	Case #
1.90	-35/-35		1.4	0.9	2.5	5.9	1
1.59	240/0		2.0	1.1	2.5	5.8	2
1.59	0/240		9.9	3.8	3.4	6.7	3
1.10	60/670		65.8	21.2	10.5	14.6	4
Measured			6.6	2.2	2.5	5.8	

Effect on a-SiGe Alloy Cells

Simulated and measured values of a-SiGe alloy cell characteristics are summarized in Tables 20 and 17. The optical gap of the a-SiGe alloy was measured to be 1.55 eV. In the simulation, a mobility gap of 1.63 eV is used for a-SiGe alloy. As in the case of a-Si alloy, V_{oc} has a strong dependence on E_g(μc-Si) only when E_g is much smaller than the mobility gap of the intrinsic layer. Good agreement between simulated and measured values is obtained for E_g(μc-Si) equal to 1.59 eV. This is again consistent with the IPE results. It is interesting to note that for a wide range of discontinuity distributions, from zero to maximum offset at either the conduction or the valence band edge, both V_{oc} and FF are remarkably insensitive. This indicates that these parameters are governed more by the bulk properties.

The simulation of quantum efficiency of a-SiGe alloy cells is less successful in explaining the experimental results. For all five cases listed in Table 20, the simulated Q ratio, i.e., the loss of carrier collection, is much lower than the measured value (see Table 21). Further simulation studies using different bulk and interface parameters will be necessary to understand this discrepancy.

Table 20. Simulated and Measured a-SiGe Alloy Cell Characteristics.
A value of 1.63 eV is used for the mobility gap of a-SiGe alloy in the simulation.

E_g(μc-Si) (eV)	$\Delta E_c/\Delta E_v$ (meV)	V_{oc} (V)	FF	Case #
1.90	-170/-100	0.75	0.61	5
1.59	-180/220	0.74	0.57	6
1.59	-90/130	0.74	0.58	7
1.59	0/40	0.74	0.60	8
1.10	-80/610	0.49	0.53	9
Measured		0.74	0.59	

Table 21. Ratio of Q(-3 V) to Q(0 V) of a-SiGe Alloy Cells.

E_g(μc-Si) (eV)	$\Delta E_c/\Delta E_v$ (meV)	λ(nm)	[Q(-3 V)/Q(0 V) - 1]×100 (%) 400	500	600	700	800	Case #
1.90	-170/-100		3.2	0.9	1.0	2.6	2.7	5
1.59	-180/220		1.5	0.6	1.1	3.2	2.6	6
1.59	-90/130		1.3	0.5	0.9	2.7	2.8	7
1.59	0/40		1.4	0.8	1.1	2.8	2.9	8
1.10	-80/610		1.4	0.7	2.1	5.5	5.7	9
Measured			13.4	7.2	5.1	6.9	10.8	

Conclusions

In conclusion, we have used IPE measurements to determine the electrical bandgap of microcrystalline *p* layers used in a-Si alloy solar cells, and the band edge discontinuities at the conduction and valence bands between μc-Si and a-Si alloy. The bandgap of μc-Si alloy is found to be around 1.6 eV, and the discontinuities at the conduction and the valence band edges are -0.02 and 0.26 eV, respectively. Use of these parameters in the numerical simulation of single-junction a-Si and a-SiGe alloy solar cells is found to predict solar cell performance under global AM1.5 illumination. However, further understanding is needed to explain the loss of carrier collection in a-SiGe alloy cells.

Section 8

Analysis of Fill Factor Losses in a-Si and a-SiGe Alloy Solar Cells

Introduction

The multijunction multi-bandgap approach has proved to be successful for obtaining high efficiency solar cells and modules (Yang et al. 1988, Guha et al. 1994, Yang et al. 1994). An initial efficiency of 11.8% and stabilized efficiency of 10.2% have been reported on approximately one square foot aperture area modules (Guha et al. 1994, Yang et al. 1994). The derating factor in efficiency for increasing the cell area from 0.25 cm^2 active area to the module aperture area is small. Any further improvement in the module efficiency can be brought about only by first increasing the small area cell efficiency. In recent times, several techniques have been used to improve the component cell efficiency and reduce losses in the multijunction structure (Banerjee et al. 1994-1, Banerjee et al. 1994-2, Banerjee 1995). This section presents a new way to analyze losses in the *i* layer of single-junction a-Si and a-SiGe alloy *p i n* cells. Losses at the *p/i* interface and the bulk of the *i* layer have been investigated. The deleterious effect of substrate texture on cell performance has been explored.

There have been some studies carried out on especially the *p/i* junction loss. It was experimentally demonstrated (Arya et al. 1986, Schropp et al. 1993, Xi et al. 1994) that the open-circuit voltage, V_{oc}, the fill factor, FF, and the stability could be increased by interposing a thin interfacial graded layer and/or insulator layer between the *p* and the *i* layers of a *p i n* cell in which amorphous silicon-carbon (a-SiC) alloy was used as the *p* layer. Different explanations have been given for the carrier recombination losses occurring at the *p/i* interface and the beneficial role of the *p/i* interfacial layer. Boron contamination of the *i* layer from the underlying *p* layer, bond distortion and lattice mismatch at the *p/i* interface due to bandgap discontinuity, and back diffusion of electrons generated near the *p/i* interface are some such explanations. The wide bandgap buffer layer has been said to alleviate the boron diffusion and/or reduce back diffusion of electrons by separating the carrier generation area from the geometric interface as well as provide an electric field. Some modelling studies (Fantoni et al. 1994) of the role of thin defective buffer layers at both the *p/i* and *n/i* interfaces of *p i n* cells have been done.

All the work done to date on *p/i* and *n/i* junction losses has been carried out on cells made in the superstrate structure (glass/transparent conducting oxide/*p/i/n*/metal) in which the light is incident through the glass. In this configuration, the conventional *p* layer is either microcrystalline or amorphous SiC alloy. The inherent disadvantage is that the *p* layer is subjected to thermal stresses during the subsequent deposition of the overlying *i* and *n* layers which are normally done at higher temperatures. The microcrystalline *p* layer is especially susceptible to degradation during high temperature processing. Further, interdiffusion between the *p* and *i* layers elements is very likely. Use of C in the *p* layers makes the *p/i* junction even more complex. Thus, the superstrate structure is difficult to analyze.

In this study, we have used the substrate configuration (ss/*n/i/p*/transparent conducting oxide) to study the losses. Basically, the technique consists of the comparison of the ratio of quantum efficiency, Q, measured under reverse bias, Q(-), and zero bias, Q(0), with the fill factor measured under blue, FF_b, and red, FF_r, light illumination. A technique to reduce the losses is also described. The results provide important feedback for designing a better device.

Experimental

Both a-Si and a-SiGe alloy cells were deposited in the substrate configuration on stainless steel substrates, (ss) without any back reflector and textured Ag/ZnO back reflectors (BR) by conventional glow discharge technique. Three different types of cells were made: (1) a-Si alloy with *i* layer thickness 250-270 nm, (2) intermediate bandgap a-SiGe alloy with *i* layer thickness 150-170 nm and (3) narrow bandgap a-SiGe alloy with *i* layer thickness 140-160 nm. The Q curves of the cells were measured as a function of wavelength. The current-voltage, IV, characteristics were measured under AM 1.5 illumination, and under blue and red light illumination using narrow band-pass filters centered at 390 and 670 nm, respectively.

Results and Discussion

The Q loss curves, Q_L, defined as Q(-)/Q(0), as a function of wavelength of the a-Si alloy cells are shown in Fig. 8. The value of Q_L qualitatively denotes the carrier collection loss in the *i* layer: higher values represent higher losses. Samples 1Sa and 1Bb are cells made on ss and BR, respectively; S denotes stainless steel and B back reflector. The collection losses increase at both low and high wavelengths displaying a minimum at ~500 nm. The BR sample displays a higher loss across the entire wavelength range compared to the ss sample. Samples 1Bc and 1Sd (see Fig. 8) are similar to samples 1Bb and 1Sa, respectively, except that two thin interfacial *i* layers are interposed between the *p/i* and *n/i* junctions. Comparison of the samples 1Bc with 1Bb and 1Sd with 1Sa shows that the reduction in the collection loss is across the entire wavelength spectrum. The fractional gain is higher for the BR sample. The ss sample shows a gain mainly in the low wavelength regime. In order to separate the effects of the two interfacial layers, sample 1Be was made on BR which is equivalent to sample 1Bb except that it has only a *p/i* interfacial layer. Figure 9 compares the losses of the two samples 1Bb and 1Be. It is clear that the gain in this case is primarily in the blue part. The small gain in the red is probably a run to run variation.

The IV characteristics of the samples shown in Figs. 8 and 9 are summarized in Table 22. The values of only the open-circuit voltage, V_{oc}, measured under AM 1.5 illumination and FF_b and FF_r are shown. Comparison of the results of samples 1Sa and 1Bb show that the substrate texture has a deleterious effect on primarily the FF_b and to a certain extent on the V_{oc} and FF_r. The values of FF_b and FF_r for the samples 1Sa and 1Bb are 0.767 and 0.701, respectively, and 0.696 and 0.683, respectively. The samples 1Bc (with the double interfacial layers) shows an improvement in the values of FF_b and FF_r to 0.732 and 0.719, respectively, and V_{oc} to 0.977 V. Sample 1Sd also exhibits similar gains in FF_b and FF_r to 0.788 and 0.725, respectively, and V_{oc} to 0.995 V. Sample 1Be (with only the *p/i* interfacial layer) shows a gain primarily in FF_b to 0.718; FF_r is similar, 0.687, and V_{oc} increases to 0.964 V.

Other a-Si alloy cells with different thicknesses of *p/i* interfacial layers have been fabricated on back reflectors. The value of FF_b initially increases and then decreases with increasing thickness of the interfacial layer. The value of the FF_r is independent of the thickness of the layer.

An analysis of the above data elucidates the strong correlation between the Q_L data in Figs. 8 and 9 and the IV results shown in Table 22. High values of FF_b are associated with low values of Q_L in the lower wavelength regime and vice versa. FF_r and Q_L in the higher wavelength regime enjoy a similar inter-relationship. The increase in Q_L with decreasing wavelength at low wavelengths is attributed to back diffusion of electrons from the front surface of the cell where blue light is strongly absorbed. The increase in Q_L at wavelengths ≥500 nm is more difficult to interpret since the light is absorbed reasonably uniformly across the thickness of the *i*-layer. The substrate texture has a deleterious effect on the cell performance: FF_b decreases and Q_L in the entire wavelength regime increases. The lower FF_b and higher Q_L in the blue part are attributed to enhanced back diffusion of electrons near the *p/i* interface due to the

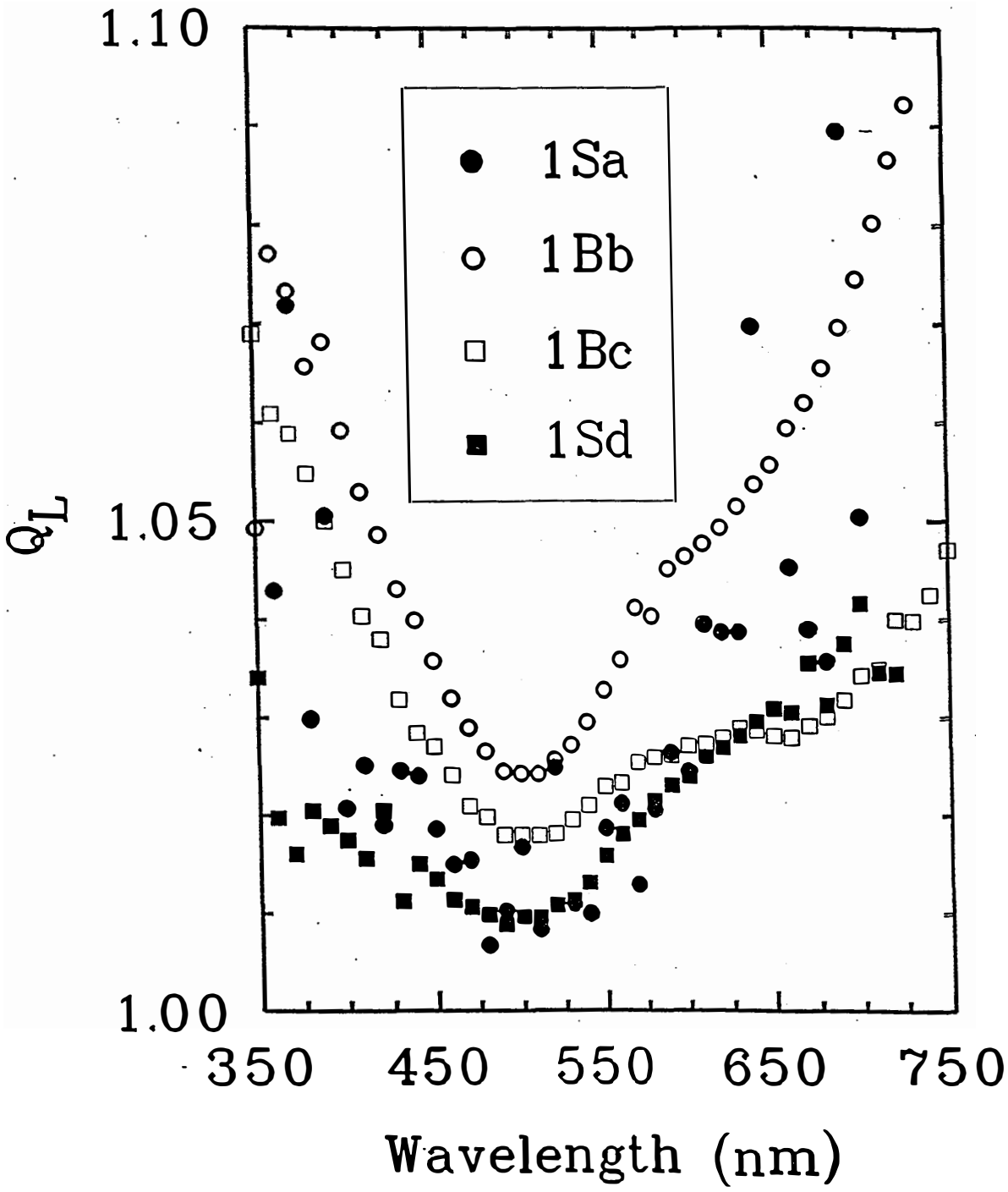

Figure 8. **Q_L curves of the a-Si alloy cells.**
Refer to Table 22 for sample description.

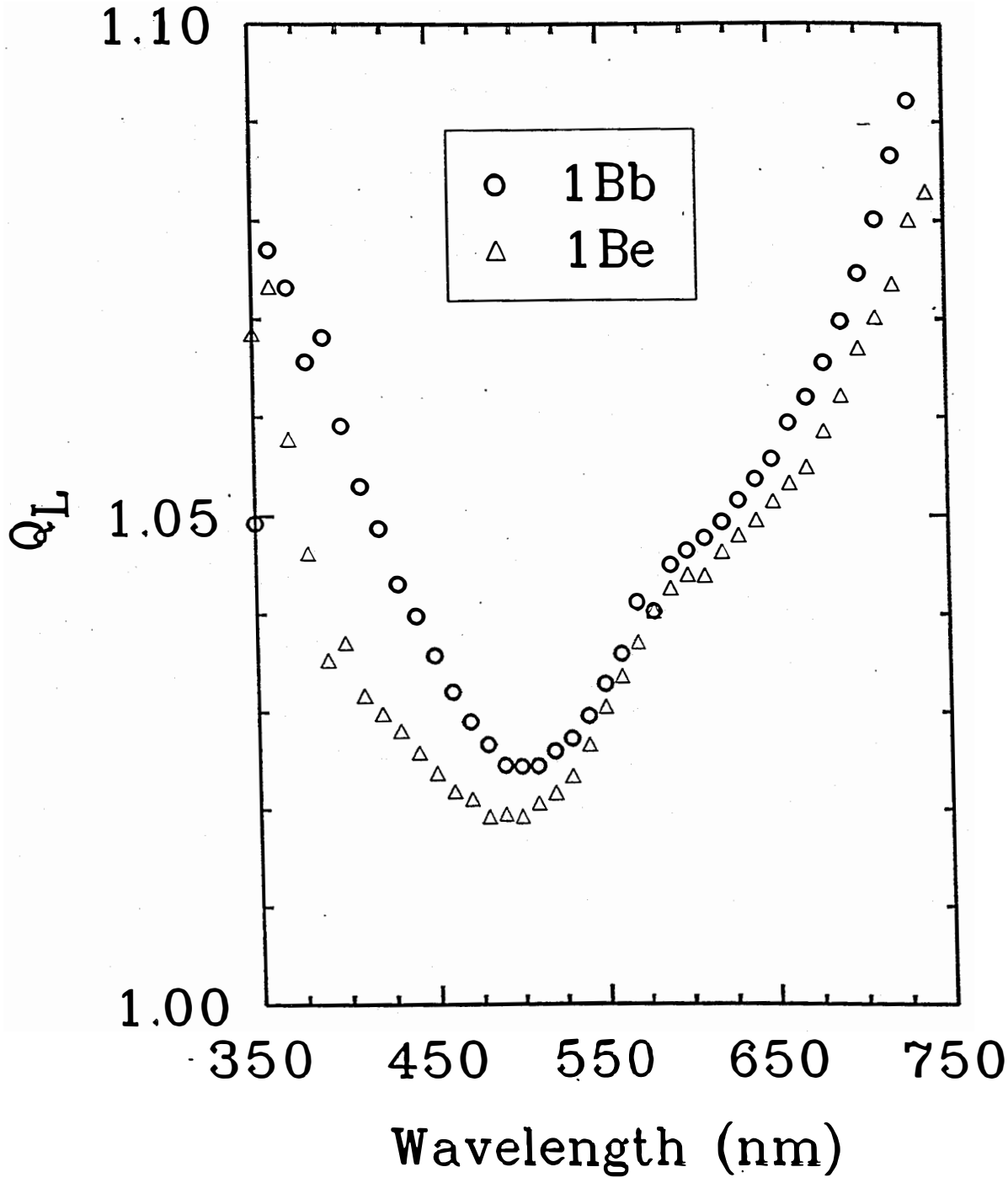

Figure 9. Q_L curves of the a-Si alloy cells with and without interfacial layer.

enhanced effective *p/i* junction area. The higher Q_L at wavelengths ≥500 nm is attributed to poorer carrier collection in the *i* layer. The role of the interfacial layers is to introduce wide bandgap layers at the junctions. The *p/i* interfacial layer leads to higher FF_b and lower Q_L in the blue part and this is attributed to reduced back diffusion effects in view of less carrier generation. The effect of the *n/i* interfacial layer is the enhancement of FF_r and reduction in Q_L over the entire wavelength range. The role of the *n/i* layer is more difficult to interpret but it appears that it improves the carrier collection in the bulk of the *i* layer.

Figure 10 shows the Q_L curves of the intermediate bandgap a-SiGe alloy cells. Sample 2Sa and 2Bb are equivalent devices on ss and BR substrates, respectively. Sample 2Zc is a cell on a textured ZnO film deposited on ss substrate: this substrate provides a poorly reflecting textured surface. Sample 2Bd is similar to 2Bb except that it has two thin interfacial *i* layers at the *p/i* and *n/i* junctions. The results are qualitatively similar to the a-Si alloy cells shown in Figs. 8 and 9. The losses are higher at the low and high wavelengths. Comparison of samples 2Bb and 2Zc with 2Sa shows that the substrate texture has a deleterious impact on Q_L over the entire spectrum. The Q_L for samples 2Bb and 2Zc are almost similar: sample 2Zc exhibits slightly lower loss at ~670 nm (wavelength at which FF_r is measured). Incorporation of the interfacial layers has an alleviating effect on Q_L: sample 2Bd exhibits Q_L as low as 2Sa except in the blue where it is slightly higher.

The IV characteristics of the cells shown in Fig. 10 are summarized in Table 23. The qualitative results are again similar to the a-Si alloy cells tabulated in Table 22. The ss sample 2Sa has V_{oc}, FF_b, and FF_r values of 0.793 V, 0.714, and 0.697, respectively. The BR sample 2Bb exhibits a deterioration in the values of FF_b and FF_r to 0.645 and 0.666, respectively. The value of V_{oc} is similar. The ZnO sample has similar values of V_{oc} and FF_b of 0.785 and 0.635, respectively, and slightly higher value of FF_r, 0.684, compared to sample 2Bb. The sample 2Bd with the interfacial layers leads to a partial recovery of FF_b and FF_r to 0.685 and 0.690, respectively. The V_{oc} is higher, 0.818 V.

The correlation and explanation of the inter-relationship between FF_b and Q_L in the blue part and between FF_r and Q_L in the higher wavelength regime is similar to the one offered earlier for the a-Si alloy cells. The texture of the substrate due to the ZnO film is primarily responsible for the degradation of the cell characteristics as shown by the similar results of samples 2Bb and 2Zc. The Ag film has a small effect as seen by the comparison of the FF_r.

The Q_L curves and the summary of the IV characteristics of the narrow bandgap a-SiGe alloy cells are shown in Fig. 11 and Table 23, respectively. The Q_L curves are similar to the ones presented earlier. It may be noted that the reverse bias applied for the Q(-) measurements for all the data presented in this paper is the same. This leads to the underestimation of the value of Q_L for the poorer quality a-SiGe alloy samples but the results are still valid. The BR sample 3Bb has lower values of FF_b, 0.648, and FF_r, 0.656, compared to the corresponding values of 0.698 and 0.687, respectively, for the ss sample 3Sa. The effect of the interfacial layers is less: the FF_r does not change and the FF_b increases marginally to 0.661. This is attributed to the poorer quality of the films limiting the device performance. For both series 2 and 3 samples, FF_b and FF_r for the interfacial layer cases are lower than the corresponding ss values.

Conclusion

In conclusion, the Q_L measurement technique provides a strong correlation with the cell performance under colored light. Higher values of Q_L in the low wavelength regime is associated with back diffusion losses at the *p/i* interface and affects FF_b. Higher Q_L values in the high wavelength regime is mainly due to bulk losses in the *i* layer and is accompanied by inferior FF_r. The technique has been used to understand some of the causes for the poorer cell results on textured substrates. The analysis has helped in finding ways to improve the device performance on textured back reflectors.

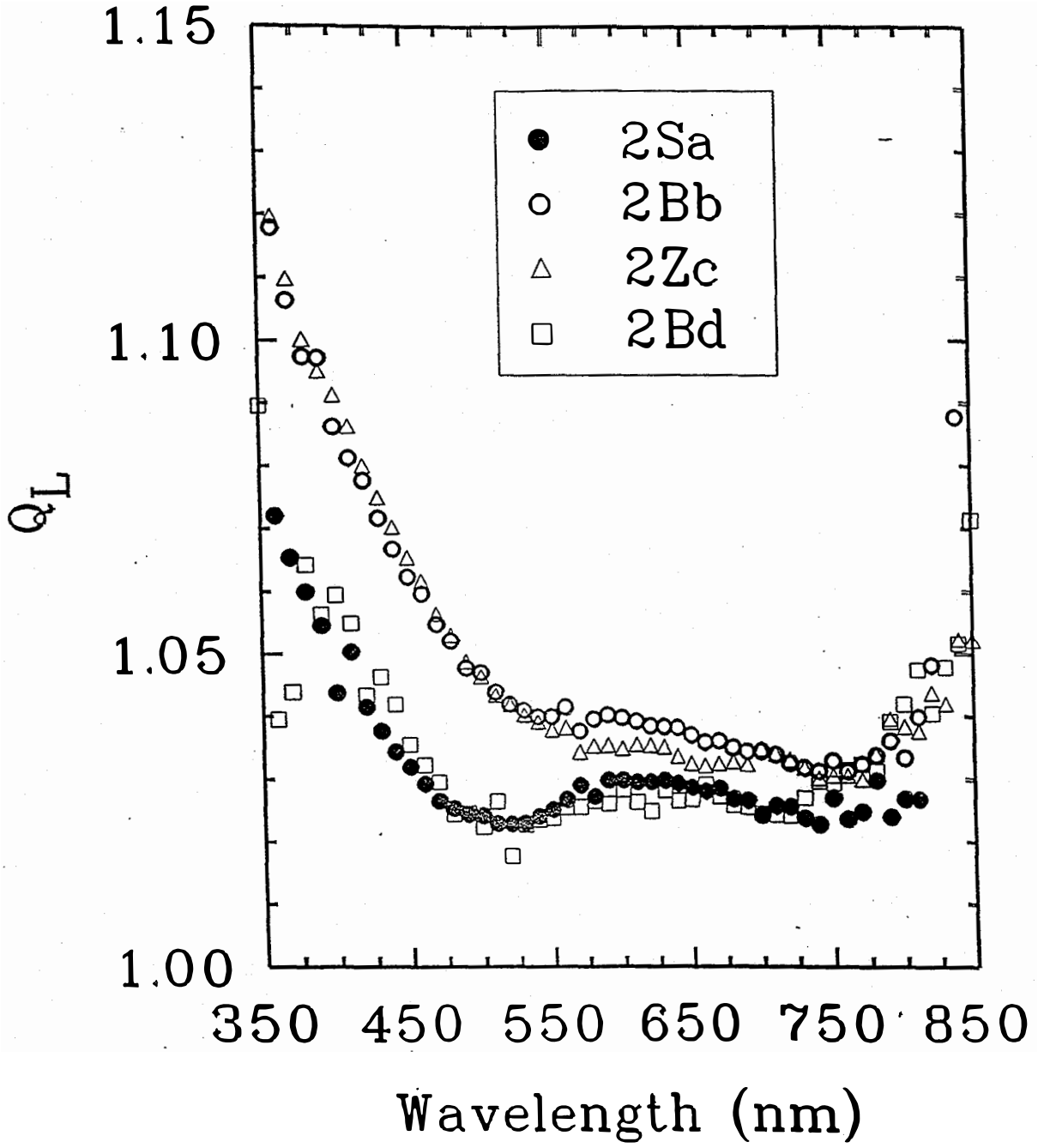

Figure 10. **Q_L curves of Intermediate bandgap a-SiGe alloy cells.** Refer to Table 23 for sample description.

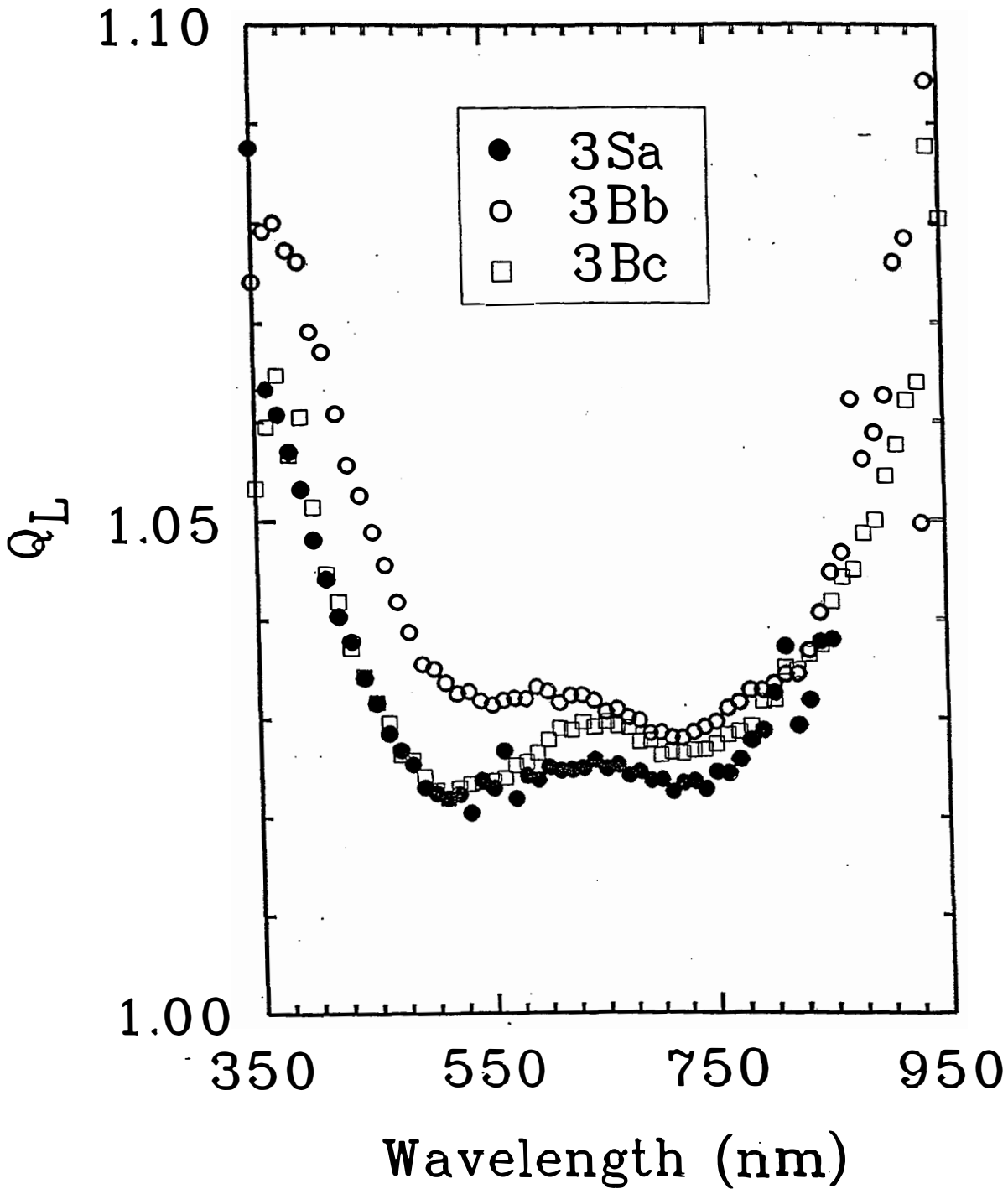

Figure 11. **Q_L curves of narrow bandgap a-SiGe alloy cells.**
Refer to Table 23 for sample description.

Table 22. V_{oc}, FF_b, and FF_r of the a-SI Alloy Cells.

Sample	Sub.	Description	V_{oc} (Volts)	FF_b	FF_r
1Sa	ss	standard	0.975	0.767	0.701
1Bb	BR	standard	0.949	0.696	0.683
1Bc	BR	p/i, n/i interface layers	0.977	0.732	0.719
1Sd	ss	p/i, n/i interface layers	0.995	0.788	0.725
1Be	BR	p/i interface layer	0.964	0.718	0.687

Table 23. V_{oc}, FF_b, and FF_r of the Intermediate (I) and Narrow (N) Bandgap a-SiGe Alloy Cells.

Sample	Bandgap	Description	Sub.	V_{oc} (Volts)	FF_b	FF_r
2Sa	I	standard	ss	0.793	0.714	0.697
2Bb	I	standard	BR	0.787	0.645	0.666
2Zc	I	standard	ZnO	0.785	0.635	0.684
2Bd	I	*p/i*, *n/i* interface layers	BR	0.818	0.685	0.690
3Sa	N	standard	ss	0.687	0.698	0.687
3Bb	N	standard	BR	0.688	0.648	0.656
3Bc	N	*p/i*, *n/i* interface layers	BR	0.719	0.661	0.655

Section 9

Analysis of Carrier Collection Losses in a-Si and a-SiGe Alloy Solar Cells

Introduction

In recent years, the gap between the highest small area cell efficiency (Yang et al. 1988) and the highest module efficiency (Guha et al. 1994) has been narrowed considerably. In order to make any significant improvement in the module efficiency, it is necessary to improve the small area cell efficiency first. In our continuing effort towards achieving this objective, we have explored (Banerjee et al. 1994-1, Banerjee et al. 1994-2, Banerjee 1995) different loss mechanisms occurring in the cells. This paper presents experimental evidence of losses existing in the bulk *i* layer and near the *p/i* interface of both a-Si and a-SiGe alloy *p i n* cells.

There have been some studies carried out on the *p/i* junction loss. It was experimentally demonstrated (Arya et al. 1986, Schropp et al. 1993, Xi et al. 1994) that the open-circuit voltage, V_{oc}, the fill factor, FF, and the stability could be increased by interposing a thin interfacial graded layer and/or insulator layer between the *p* and the *i* layers of a *p i n* cell in which a-SiC was used as the *p* layer. Some modelling studies (Fantoni et al. 1994) of the role of thin defective buffer layers at both the *p/i* and *n/i* interfaces of *p i n* cells have been done. As discussed in Section 8, all work done to date on *p/i* and *n/i* junction losses have been carried out on cells made in the superstrate structure (glass/TCO/*p/i/n*/metal) in which the light is incident through the glass. In this configuration, the conventional *p* layer is either microcrystalline or amorphous SiC alloy. The inherent disadvantage is that the *p* layer is subjected to thermal stresses during the subsequent deposition of the overlying *i* and *n* layers which are normally done at higher temperatures. The microcrystalline *p* layer is especially susceptible to degradation during high temperature processing. Further, interdiffusion between the *p* and *i* layers elements is very likely. Use of C in the *p* layers makes the *p/i* junction even more complex. Thus, the superstrate structure is more difficult to analyze.

In this study, we have used the substrate configuration (metal/*n/i/p*/TCO), where the *p* layer is the last glow-deposited layer, to study the losses using reverse biased quantum efficiency, Q, and FF under blue and red light measurements. The paper describes the collection loss near the *p/i* junction and the bulk of the *i* layer and interface passivation techniques to improve the cell performance. The results have uncovered possible inhomogeneities in the direction of a-Si alloy film growth which are dependent on the deposition conditions.

Experimental

Both a-Si and a-SiGe alloy cells were deposited on stainless steel substrates (without any back reflector) by conventional glow discharge technique. The loss in the *i* layer was studied as a function of four variables: (1) optical bandgap, (2) thickness, (3) material quality, and (4) plasma treatment of the *n* surface. Two optical gap materials a-Si (~1.77 eV) and a-SiGe (~1.45 eV) alloys were used. Three different material qualities were investigated: a-Si, a-SiGe, and light-degraded a-SiGe alloy cells. The thicknesses of the *i* layers of the a-Si alloy cells were 120 nm for samples 1 and 2 and 250 nm for sample 3 and those of the a-SiGe alloy cells 4, 5, and 6 were 140, 280, and 560 nm, respectively. Sample 2 was subjected to a plasma treatment after the *n* layer deposition. The values of FF under blue and red light illumination, FF_b and FF_r, respectively, were measured using narrow-band-pass filters centered at 390 nm

and 670 nm, respectively. The values of Q versus wavelength were obtained for both zero bias, Q(0), and negative bias, Q(-) and the Q_{loss}, defined as the ratio of Q(-) to Q(0) was plotted. The values of the negative bias for the 120 nm a-Si alloy, 250 nm a-Si alloy, and the a-SiGe alloy cells were -1V, -2V, and -3V, respectively. The a-SiGe alloy cells 5 and 6 were light soaked for over 1000 hours and then remeasured.

Results and Discussion

The results of the Q_{loss} versus wavelength measurements for the a-Si alloy cells are shown in Fig. 12 All the samples exhibit a similar behavior: the Q_{loss} is higher at the low and high wavelength regimes with a minimum at intermediate wavelengths. The blue light is strongly absorbed near the front surface of the cell. The higher loss at these wavelengths has been shown (Banerjee et al. 1995) to be due to the back diffusion of the relatively high concentration of electrons from near the *p/i* interface. Intermediate wavelength ~500 nm light is also absorbed, but less strongly, near the front surface of the cell and results in a lower loss since back diffusion effects are less important at this wavelength. The excess loss at higher wavelengths >470 nm for samples 1 and 3 is difficult to interpret since the red light is uniformly absorbed in the *i* layer. In general, the red Q_{loss} can be attributed to losses across the entire thickness (bulk) of the sample.

The values of FF_b and FF_r of the a-Si alloy cells are summarized in Table 24. FF_b, measured using 390 nm light, is a measure of electron transport from the front surface of the cell where the monochromatic light is strongly absorbed to the back. Similarly, FF_r is a measure of the hole transport property in the bulk of the *i* layer. As reported (Banerjee et al. 1995), the values of FF_b and FF_r have a correlation with the Q_{loss} values at 390 nm and 670 nm, respectively. High values of FF_b and FF_r are associated with low values of Q_{loss} at 390 nm and 670 nm, respectively, and vice versa.

Table 24. Thickness, FF_b, and FF_r of a-Si and a-SiGe Alloy Cells.

Sample	*i* layer	*i* thickness (nm)	FF_b		FF_r	
			Initial	Degraded	Initial	Degraded
1	a-Si alloy	120	0.77		0.69	
2	a-Si alloy	120	0.78		0.77	
3	a-Si alloy	250	0.79		0.72	
4	a-SiGe alloy	150	0.69		0.68	
5	a-SiGe alloy	280	0.67	0.58	0.69	0.56
6	a-SiGe alloy	560	0.65	0.46	0.59	0.48

Sample 2 exhibits anomalous low Q_{loss} at wavelengths >470 nm (see Fig. 12) and high FF_r (see Table 24) compared to sample 1. The FF_r of samples 1 and 2 are 0.69 and 0.77, respectively, even though the FF_b for both samples are similar, 0.77 - 0.78. This result implies that the carrier collection in the bulk of the *i* layer is superior for sample 2. This is a surprising result since the only difference between the two samples is that sample 2 has been subjected to an additional plasma treatment after the *n* layer. There are three possible roles of the plasma treatment: (1) it reduces/eliminates any potential barrier at the *n/i* interface, (2) it produces a thin layer with very different material properties which readjusts the electric field distribution in the *i* layer resulting in superior current collection, and (3) it creates a surface which

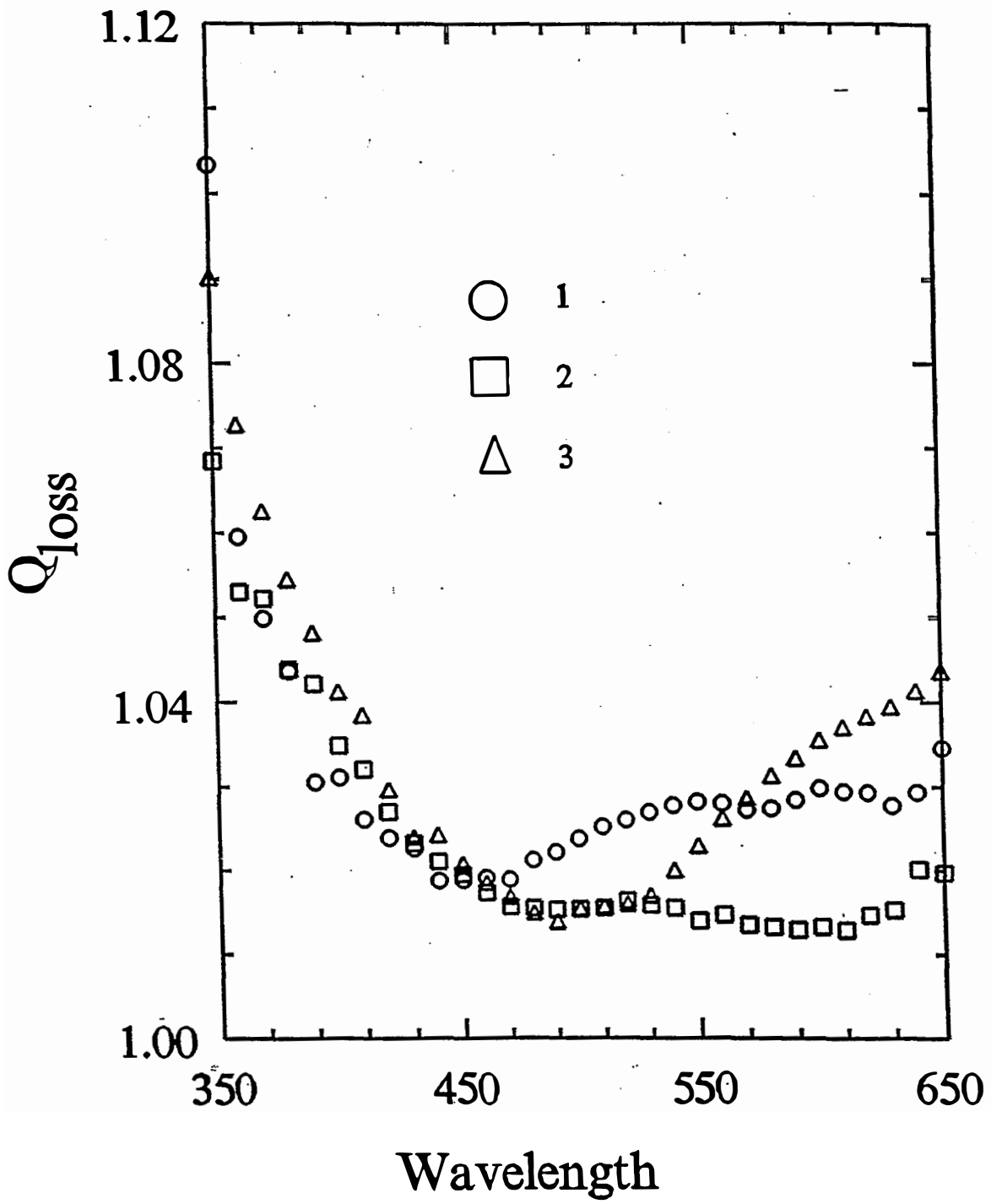

Figure 12. Q_{loss} versus wavelength of the a-Si alloy cells.
Refer to Table 24 for sample description.

is congenial for the growth of low defect density *i* layer material. The first phenomenon is unlikely since the respective band edges on both sides of the amorphous *n/i* junction are expected to line up. In such a scenario it is not possible to have any significant barrier at the junction. In order to test the second hypothesis, we have simulated the values of Q_{loss} and fill factor of cells with and without a thin interfacial layer at the *n/i* junction using the AMPS model developed by Penn State University (Arch et al. 1991). In the model, the *i* layer was assigned a certain defect density and the defect density of the thin *n/i* interfacial layer was varied over one order of magnitude both lower and higher than the designated value for the *i* layer. The parameters were selected such that the model simulated the results of sample 1 fairly well. However, it failed to match the experimental values of Q_{loss}, FF_b, and FF_r of sample 2. In fact, the modelling showed that the effect of the interface layer on the device characteristics was small despite the large changes (two orders of magnitude) in the properties of the interfacial layer. This result eliminates the second hypothesis. Thus, the only viable explanation of the low Q_{loss} in the red and high FF_r of sample 2 is the improvement of the material quality in the bulk of the *i* layer. This result has an important implication: the quality of the *i* layer and thereby the film growth mechanism is dependent on the surface properties of the substrate and predeposition conditions. The *i* layer deposited directly on an *n* layer possesses a higher concentration of defect density than on a "passivated" surface. On a textured surface the losses have been reported (Banerjee et al. 1995) to be even higher.

It may be expected that the properties of the *i* layer become independent of the substrate material beyond a certain thickness which in turn would imply an inhomogeneity in the material properties in the direction of film growth. In fact, this is borne out by the shape of the Q_{loss} curve of the thicker sample 3. The loss is as low as that of sample 2 at the wavelength ~500 nm (see Fig. 12), even though the sample is thicker and no "passivation" was done after the *n* layer. It is not clear why the value of FF_r, 0.72, is higher than that of sample 1. Tentatively, based on the earlier hypothesis that the *i* layer initially grows on an untreated *n* layer with higher defect density, the thicker sample is expected to absorb a certain portion of the light in the better quality top half of the cell which would then lead to a superior "average" value of FF_r results. The Q_{loss} exhibits steeper "wings" in the low and high wavelength regimes: the losses rise faster in these two regions. The increase in losses in the wavelength ranges 400 - 500 nm and 500 - 650 nm are attributed to the extra thickness (compared to samples 1 and 2) the photogenerated electrons and holes, respectively, have to travel before they are collected.

The above results imply that at least in the device configuration the *i* layer suffers from inhomogeneities in the transverse direction: the defect density initially decreases with increasing thickness before reaching a saturation value after a decay length of a few tens of nanometers. Curtins and Favre (1989) have reported a similar phenomenon in very high frequency glow discharge intrinsic a-Si alloy films deposited at a high rate of 1 - 2 nm/s. Their conclusion was derived from trying to model the deep and shallow defect density obtained by photothermal deflection spectroscopy for thick films. They reported a much higher decay length of ~1 μm. In order to reconcile with both the results it may be speculated that the material quality during the initial phase of growth depends on a host of conditions such as nature of the plasma reactor, deposition rate and frequency, plasma treatment, substrate preparation, etc. The scope of the present work is to suggest the existence of the complex interrelationship amongst the parameters listed above. Detailed work is necessary for a better understanding of the phenomena.

Figure 13 displays the Q_{loss} for the a-SiGe alloy cells. The initial characteristics (shown in open symbols) are qualitatively similar to the a-Si alloy results. The differences are discussed. The front surface back diffusion losses extend to higher wavelengths: comparison of the thinnest samples (1, 2, and 4) in Figs. 12 and 13 shows that for the a-Si alloy cells, the losses extend to 450 - 480 nm whereas for the a-SiGe alloy cells, the losses extend beyond to 500 - 550 nm. This is attributed to the higher absorption coefficient of the a-SiGe alloy films. Further, the absolute value of the Q_{loss} over the entire spectrum is higher in view of the poorer quality of the a-SiGe alloy *i* layers. The thickness dependence

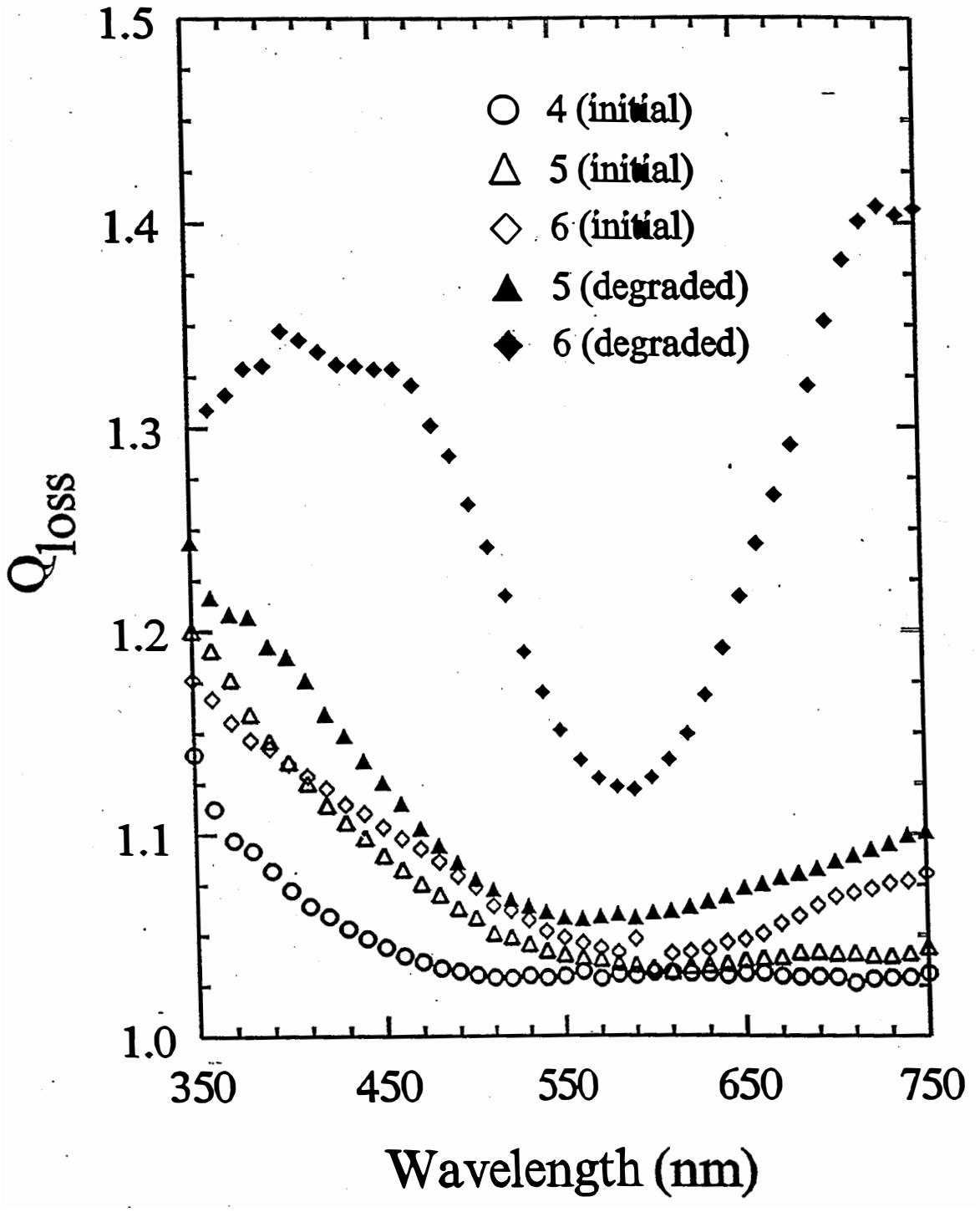

Figure 13. **Q_{loss} versus wavelength of the a-SiGe alloy cells.** Refer to Table 24 for sample description.

and the corresponding explanation of the Q_{loss} in terms of the characteristic steeper "wings" at the lower and higher wavelengths are similar to the a-Si alloy case. The results of the light-degraded a-SiGe alloy samples 5 and 6 are shown in Fig. 13. Compared to the initial values, the degraded results expectedly exhibit greater losses. The losses in the "wings" regions increase faster: the effect in the thicker sample 6 is more pronounced. As explained earlier, the losses in the "wings" are attributed to the bulk where the photogenerated carriers have to travel over long distances before they can be collected. Light soaking adversely affects collection losses for both electrons and holes. The enhanced losses are attributed to the poorer transport properties of the carriers. The behavior of the degraded sample 6 in the wavelength range 350 - 400 nm is anomalous and further work needs to be done to understand it.

The colored FF results of the a-SiGe alloy cells are summarized in Table 24. The initial results show that the value of FF_b deteriorates progressively from 0.69 to 0.65 as the thickness of the *i* layer is increased from sample 4 to sample 6. The Q_{loss} trend (see Fig. 13) is similar. The values of FF_r for samples 4 an 5 are similar ~0.68-0.69; for the thickest sample 6 it is only 0.59. The Q_{loss} curves at 670 nm reflect a similar trend. The lower values of FF_b and FF_r of the light soaked samples also have a good correlation with the corresponding Q_{loss} behavior.

Conclusion

In conclusion, carrier collection losses in the front surface and the bulk of the *i* layer of a-Si and a-SiGe alloy cells have been identified using the Q_{loss} technique. The quality of the a-Si alloy film appears to be dependent on the nature of the surface on which it grows. There is some evidence of inhomogeneity in the material properties of the a-Si alloy film along the direction of film growth in the device configuration. The deposition conditions play an important role in determining the properties of the initial growth phase. The bulk loss increases with increasing *i* layer thickness as well as with decreasing material quality. Light soaking has a deleterious effect on both electron and hole transport. There is a strong correlation between the Q_{loss} and the values of the colored FF.

Section 10

Stability Study of a-Si:D and a-Si:H *p i n* Alloy Solar Cells

Introduction

Light-induced degradation of hydrogenated amorphous silicon (a-Si:H) alloy materials and devices has been the subject of intensive studies. It is generally agreed that recombination of excess electron-hole pairs generated by illumination creates metastable defects in the bulk of the material (Guha et al. 1983). The defect states reduce the mobility-lifetime of the carriers and causes degradation of solar cell performance. The origin of the metastability is not quite understood, and the list of possible causes includes (Wronski and Maley 1991) hydrogen, impurities such as O, N, and C, microvoids, weak bond, or a combination of these. The possible involvement of hydrogen in the light degradation process has motivated several workers to replace hydrogen with its isotope, deuterium, in the a-Si alloy and to investigate stability issues. Stutzmann et al. (Stutzmann et al. 1986) studied the spin density after light exposure for both deuterated and hydrogenated alloys and came to the conclusion that light-induced degradation in both the materials is similar. In a series of experiments, Ganguly et al. (Ganguly et al. 1990, 1991, 1994) have studied light-induced changes in photoconductivity and defect density in hydrogenated and deuterated alloys deposited by using SiH_4 or SiD_4 gases. They reported that in the degraded state, photoconductivity was higher in the deuterated alloy although the defect density from constant photocurrent method (CPM) was larger than the hydrogenated film. They explained this contradiction by postulating the existence of two kinds of defects having different electron capture cross-sections. On the other hand, we have previously reported (Yang et al. 1994) that cells with high hydrogen dilution showed better performance both in the degraded and the initial states than that prepared with low hydrogen dilution, while defect density from CPM measurement showed no difference between them.

We have focused on deuterated amorphous silicon (a-Si:D) alloys deposited with deuterium dilution, which is a totally different regime from what was previously studied. We present here results on deuterated and hydrogenated a-Si alloy solar cells where intrinsic layers were deposited by using the same gas flow rates at the same deposition rate and show reduced light-induced degradation in the deuterated cells. We also present the similarity of hydrogen (deuterium) effusion results between heavily diluted a-Si:H alloy and normally diluted a-Si:D alloy. Possible explanations are discussed.

Experimental

Single-junction *p-i-n* solar cells were grown by the rf glow discharge technique on stainless steel substrates with predeposited silver-zinc oxide back reflector. The intrinsic layers were grown using the following gas mixtures: SiH_4+H_2, SiD_4+D_2, SiH_4+D_2, and SiD_4+H_2. The deposition temperature range investigated was between 150-300 °C. Except for one experiment where the doped layers also used deuterated gases, hydrogenated doped layers prepared under the same conditions were used for all the experiments. Light soaking at 50 °C under one-sun conditions was carried out on pairs of cells in which the intrinsic layer deposition parameters were similar except for the substitution of hydrogen by deuterium. In addition to the measurement of cell parameters in the initial and light-degraded states, the bonding and also the quantity of hydrogen/deuterium in the material were investigated using hydrogen/deuterium effusion, infrared, and secondary ion mass spectroscopy (SIMS) studies. The intrinsic alloy films were deposited on crystalline silicon wafers or bare stainless steel for these experiments.

Results and Discussion

Table 25 shows the performance of a set of three solar cells in which the intrinsic layers were deposited at a substrate temperature of 200 °C. Sample 5742 uses deuterated material for all the layers (both doped and intrinsic), sample 5622 uses deuterated gas mixture only for the intrinsic layer, and sample 5752 has hydrogenated alloys for all the layers. The thicknesses of the three cells were identical. It is apparent from Table 25 that the degradation in efficiency for the all-deuterated cell is similar to that of the cell where only the intrinsic layer is deuterated. Both the cells show lower degradation than the hydrogenated cell. The fill factor (FF) in the light-soaked state for the deuterated cells is higher than that of the hydrogenated cell. This indicates superior stability of the deuterated material. Table 25 also shows a higher open-circuit voltage (V_{oc}) and lower short-circuit current density (J_{sc}) for the deuterated cell (5622) as compared to the hydrogenated cell (5752). Quantum efficiency versus wavelength data of both cells are shown in Fig. 14. It reveals that short wavelength (λ<500 nm) response of the two cells is similar, while the long wavelength (λ>500 nm) response accounts for the 2 mA/cm^2 difference in photocurrent. This indicates that the deuterated cell has a wider bandgap than the hydrogenated cell. Our preliminary measurement of deuterium/hydrogen in the films shows the deuterium content in the deuterated material to be higher than the hydrogen content in the hydrogenated material. This probably explains the change in the bandgap leading to the differences in V_{oc} and J_{sc}. We also find that the degradation in V_{oc} is much lower for the deuterated cell and is absent in the all-deuterated cell. nce the degradation of V_{oc} is believed to be caused both by the bulk and the interface, further investigation of this phenomenon may give us a better understanding of the relative importance of the two factors.

Table 25. Initial and Light-soaked J-V Characteristics for *p i n* Cells Prepared with Different Gas Mixtures at the Same Gas Flow Rate and the Same Deposition Rate.

Sample	Thickness (nm)	Temperature (°C)	Gas Mixture	Light-Soaked (hours)	J_{sc} (mA/cm^2)	V_{oc} (V)	FF	Efficiency (%)
5742	310	200	*p,i,n*-layer:	0	13.72	0.977	0.678	9.09
			D_4+D_2	1010	13.30	0.977	0.632	8.21
				degradation (%)	3.1	0	6.8	9.7
5622	310	200	*p,n*-layer:	0	13.17	1.018	0.704	9.44
			H_4+H_2	1010	12.91	1.005	0.655	8.50
			i-layer:					
			D_4+D_2	degradation (%)	2.0	1.3	7.0	10.0
5752	310	200	*p,i,n*-layer:	0	15.13	0.968	0.676	9.90
			H_4+H_2	1010	14.46	0.930	0.607	8.16
				degradation (%)	4.4	3.9	10.2	17.6

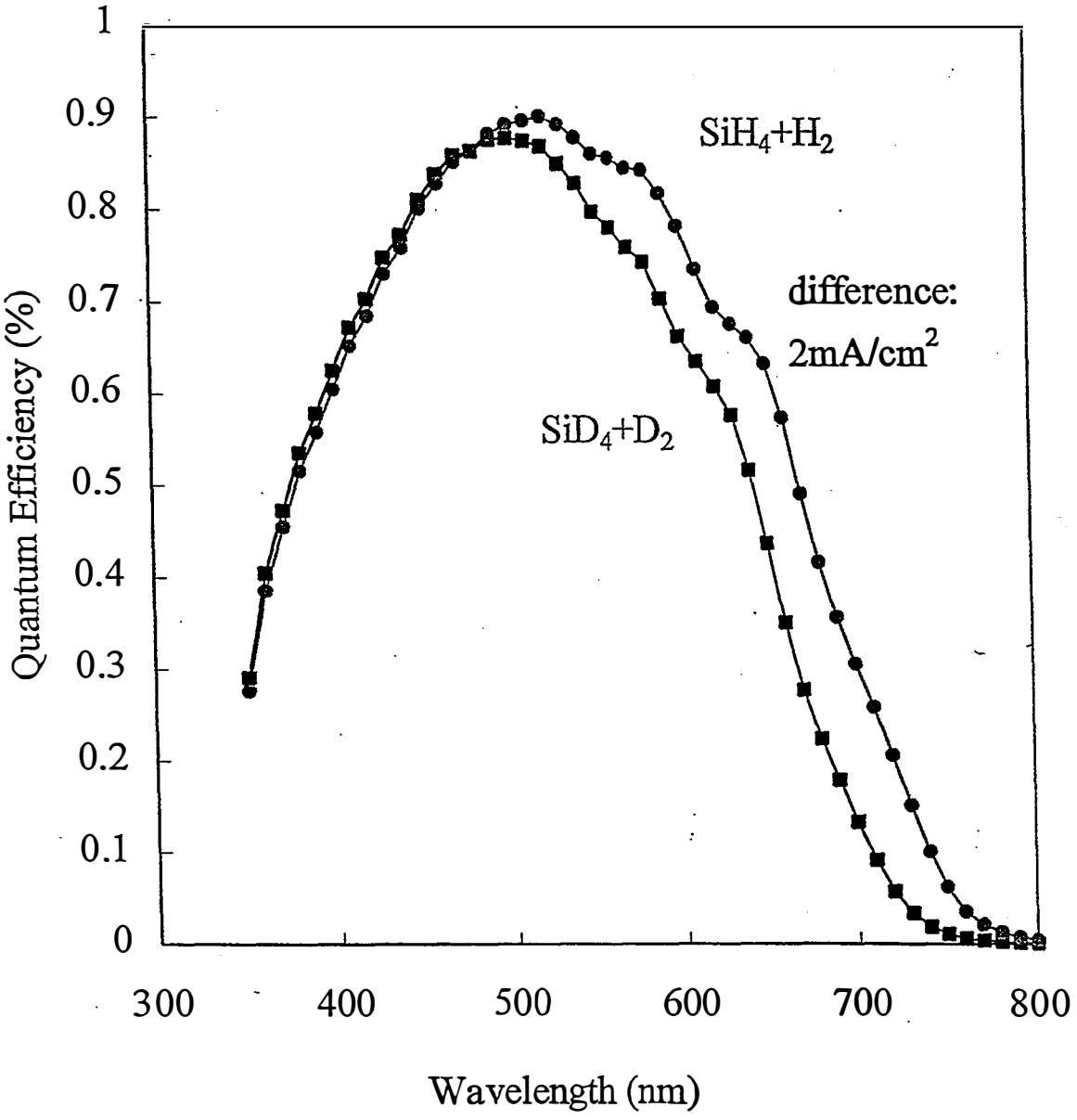

Figure 14. **Quantum efficiency versus wavelength data of hydrogenated and deuterated samples deposited with the same gas flow rates at the same deposition rate.**

In order to investigate if it is necessary to replace hydrogen completely to improve stability, we have also investigated the degradation behavior of cells where the intrinsic layers were made from SiH_4+D_2 and SiD_4+H_2 mixtures. As can be seen from Table 26, the degradation behavior is similar to cells made from SiH_4+H_2, while we have confirmed fairly high deuterium content in both the films by infrared absorption measurement. This result shows that improved stability in a-Si:D cell does not originate from simple replacement of hydrogen with deuterium. The reason why total elimination of hydrogen from the gas mixtures used for depositing the intrinsic layer is necessary for improving stability is not clear, but it is possible that some kind of structural change occurs in the film, and deuterium assists it better than hydrogen. We have also carried out experiments on cells in which the intrinsic layers are deposited at temperatures up to 300 °C and find the same trend in degradation, namely, the deuterated cells degrade less than the hydrogenated cells.

Table 26. Initial and Light-soaked J-V Characteristics for *p i n* Cells Prepared with SiH_4+D_2 and SiD_4+H_2 Gas Mixtures.

Sample	Thickness (nm)	Temperature (°C)	Gas Mixture	Light-Soaked (hours)	J_{sc} (mA/cm^2)	V_{oc} (V)	FF	Efficiency (%)
5744	310	200	*p,n*-layer:	0	15.15	0.975	0.697	10.3
			SiH_4+H_2	1000	14.43	0.938	0.610	8.3
			i-layer:					
			SiH_4+D_2	degradation (%)	4.8	3.8	12.5	19.8
5818	310	200	*p,n*-layer:	0	14.35	1.004	0.665	9.6
			SiH_4+H_2	1000	13.23	0.980	0.602	7.8
			i-layer:					
			SiD_4+H_2	degradation (%)	7.7	2.4	9.5	18.5

Although the deuterated cells degrade less than their hydrogenated counterparts, degradation is not totally eliminated and the stabilized efficiency was not improved. SIMS analysis on our deuterated samples reveals hydrogen content to be about 10^{20}/cc. Since the metastable defect density is less than 10^{17}/cc, we can not rule out the possibility that the presence of this substantial amount of hydrogen may be responsible for the light-induced degradation. We do not know yet the source of the hydrogen contamination. The deuterated gases contain less than 10 ppm hydrogen. It is possible that the hydrogen is coming from the deposition chamber walls which are coated with hydrogenated alloys?

A plausible explanation for the hot electron degradation in transistors was provided (Lyding et al. 1996) in terms of the electron population of the Si-H antibonding states, resulting in a force that accelerates the hydrogen away from the silicon surface. That acceleration, of course, is diminished for deuterium because of its higher mass, giving rise to the lower degradation. While one can not rule out the population of the antibonding states of Si-H (D) by photogenerated electrons, the high value of the energy of such states (~5 eV above conduction band) makes the occupation probability low. A similar mechanism for improved

stability is, therefore, less obvious. Hydrogen/deuterium effusion studies (Fig. 15) show that there is a narrow peak at a lower temperature (~400 °C) in the deuterated material, whereas the corresponding peak does not exist in the hydrogenated material. The difference of this effusion spectra suggests that the structure of the two materials is different. It is interesting to point out that similar effusion at low temperature has also been observed in hydrogenated material grown with heavy hydrogen dilution at the lower deposition rate (Xu et al. 1994). The hydrogen effusion measurement of the hydrogenated films depending on hydrogen dilution and deposition rates is shown in Fig 16. The peak at the lower temperature (~400 °C) does not exist for the film with normal hydrogen dilution and normal deposition rate, but the peak position is shifted to a lower temperature for the film with higher hydrogen dilution and normal deposition rate and the sharp peak at about 400 °C appears at the film with heavy hydrogen dilution and lower deposition rate. Films grown with heavy hydrogen dilution at the lower deposition rate have been found to have more oriented microstructures and low density of isotropic nanovoids as measured by small-angle X-ray scattering (SAXS). It has been speculated that this material is characterized by a more ordered microstructure which also leads to improved stability. The similarity in the effusion characteristics of the deuterated and the hydrogenated alloys deposited with heavy hydrogen dilution therefore indicates that the improved stability of the deuterated cells is also related to improved microstructure. The best stabilized fill factor for the deuterated cell with an *i*-layer thickness of 310 nm is 0.655. The corresponding value obtained for a hydrogenated cell grown with heavy hydrogen dilution and of 270 nm thickness is 0.63. The deuterated cell thus appears to have better stable FF than the best hydrogenated cell even though it is slightly thicker. A somewhat similar result about higher FF in a degraded deuterated cell was reported by Nevin et al. (Nevin et al. 1991). But the film structure, which we regard as very important, in their material must be quite different from ours because the degradation of their cells is very high. Also McElheny et al. (McElheny et al. 1991) reported that the deuterium effusion was greater at temperatures below 400 °C than hydrogen effusion, but their film structure is also different from ours because the effusion spectrum does not show any sharp peak and is only slightly different from the hydrogenated film.

We have also prepared a highly diluted hydrogenated cell by increasing the rf power to match the deposition rate of the deuterated cell. The initial and degraded characteristics of both cells are listed in Table 27. Although we can not compare the characteristics directly because of the different thicknesses, the degradation of hydrogenated cell (6251) is higher even though it is thinner. This result also agrees with hydrogen effusion data shown in Fig 16, where we find that the effusion spectra of the two films are quite different, suggesting that the film structures are also different. Although the reason why deuterium produces stable microstructure more easily than hydrogen is not clear, it is possible that deuterium with a higher mass impinges on the growing surface with a higher energy, forming a denser silicon network structure thus relaxing film stress. On the other hand, it is interesting to point out that the J_{sc} in hydrogenated cell is higher than the deuterated one even though hydrogenated cell has a smaller thickness and similar V_{oc}. We also observed a higher stable efficiency in hydrogenated cell, mainly due to its higher J_{sc}.

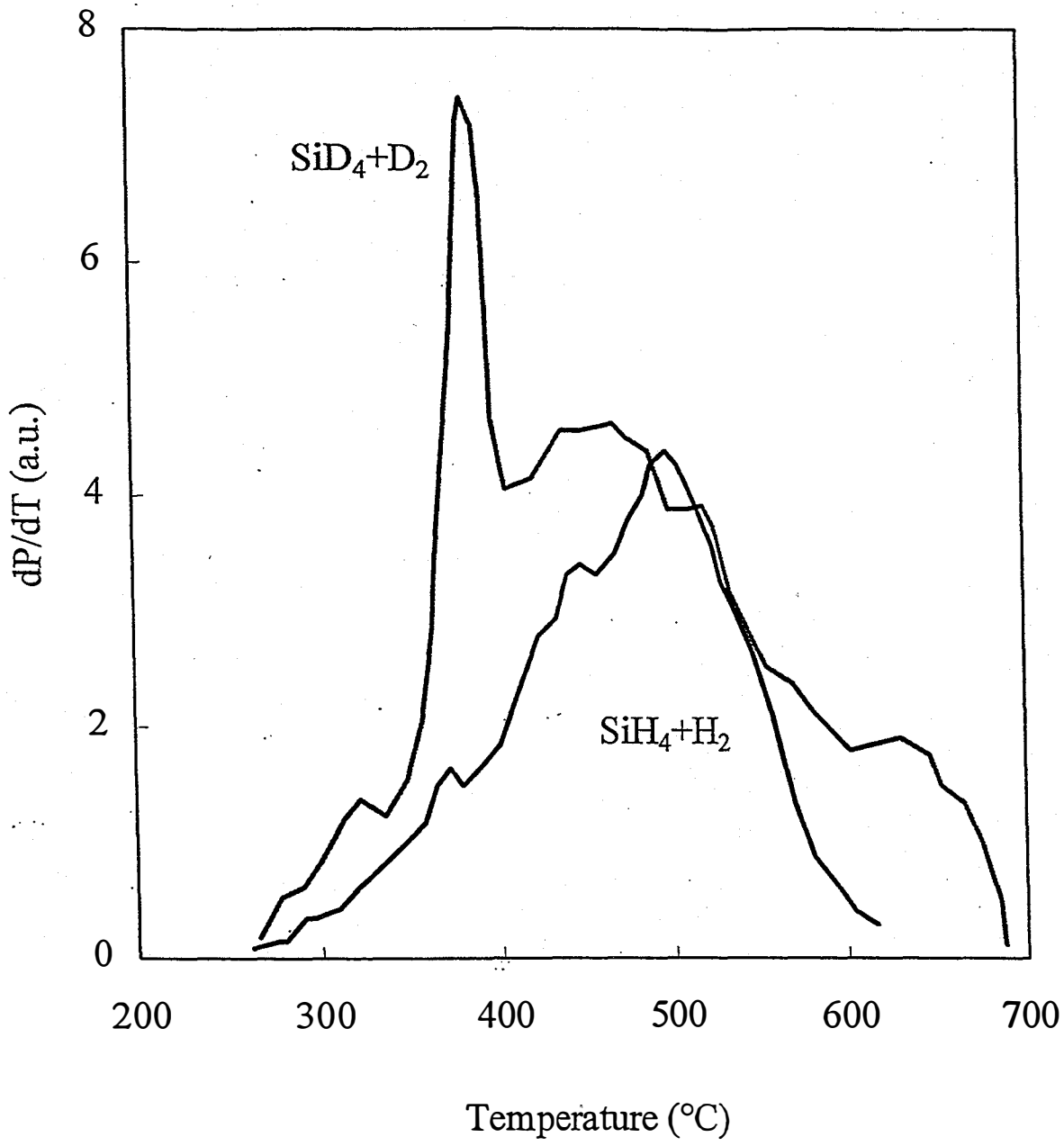

Figure 15. **Hydrogen (deuterium) effusion spectra from hydrogenated (deuterated) samples deposited by the same gas flow rate at the same deposition rate.**

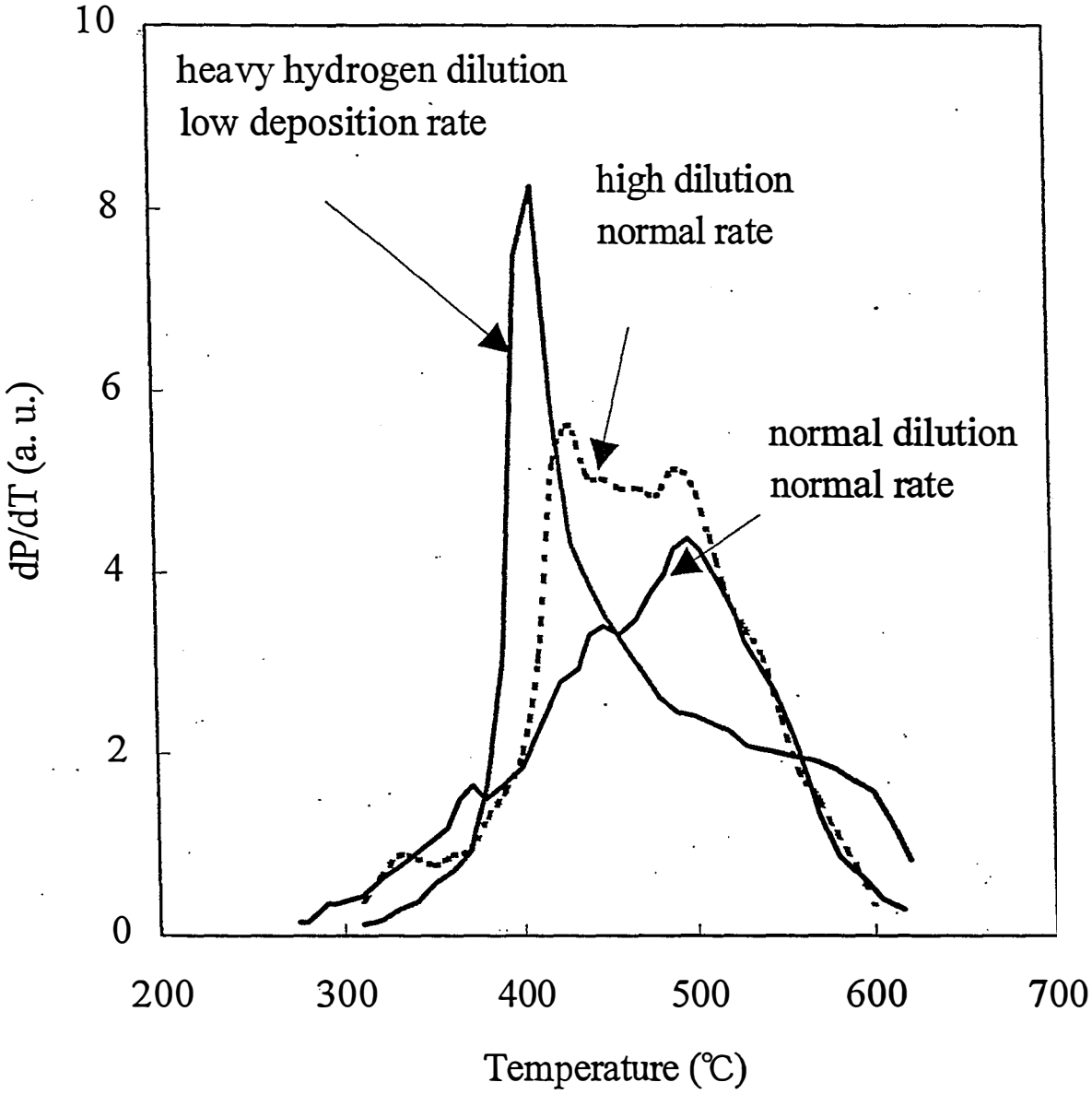

Figure 16. Hydrogen effusion spectra from hydrogenated samples.

Table 27. Initial and Light-soaked J-V Characteristics for *p i n* Cells Prepared with D_4+D_2 and Highly Diluted H_4+H_2 Gas Mixtures at the Same Deposition Rate.

Sample	Thickness (nm)	Dilution D_2 (H_2)	Gas Mixture	Light-Soaked (hours)	J_{sc} (mA/cm^2)	V_{oc} (V)	FF	Efficiency (%)
5622	310	normal	*p,n*-layer:	0	13.17	1.018	0.704	9.44
			H_4+H_2	1010	12.91	1.005	0.655	8.50
			i-layer:					
			D_4+D_2	degradation (%)	2.0	1.3	7.0	10.0
6251	230	high	*p,i,n*-layer:	0	14.69	1.012	0.707	10.51
			H_4+H_2	1010	13.82	0.980	0.646	8.75
				degradation (%)	5.9	3.2	8.6	16.7

The correlation between effusion at low temperature and stability of both hydrogenated and deuterated alloys strongly indicates that microstructure of the material plays a key role in improving the stability. Based on electron microscope and Raman studies, we have now found more direct evidences about the structural change related with film stability against light-exposure (Tsu et al. 1997). It is well-known that hydrogen etches the growing surface and, in the extreme case of high dilution and high applied power, can induce greater order. Our experiments on doped microcrystalline deuterated alloys presented earlier show that deuterium also behaves the same way. What is interesting, however, is the fact that in a very limited number of experiments, the deuterated cells show higher stabilized fill factor than the hydrogenated cells in spite of the wealth of experimentation done on the latter. This leads to the possibility of obtaining even better stability with the deuterated alloy as our understanding is further enhanced. It is also interesting that deuterium seems to produce this kind of microstructure at a higher deposition rate than hydrogen. Further understanding of this mechanism will help to develop deposition processes for production in which high deposition rate is desirable.

Section 11

Effect of μc-*n* Layer on a-Si/a-Si and a-Si/a-SiGe Alloy Double-junction Cells

Introduction

It is well known that microcrystalline (μc) boron-doped layer plays a key role in improving the efficiency of a-Si alloy solar cells. Compared to their amorphous counterpart, μc *p*-type layers show lower conductivity activation energy and higher optical transmission, giving rise to higher open-circuit voltage and short-circuit current for the solar cell. On the other hand, phosphorus-doped *n*-type amorphous silicon alloy films exhibit lower activation energy and higher transmission than *p*-type a-Si alloy films; therefore, we have been using *n*-type a-Si alloy layers in our multijunction cells.

In a continuous effort to improve the multijunction solar cell efficiency, we have examined the possibility of reducing light absorption caused by a-Si alloy *n* layers and lowering contact resistance. Specifically, we have studied the effect of replacing the amorphous *n* layers by μc-*n* layers on the performance of multijunction cells by carrying out a set of experiments incorporating μc-*n* layers in the tunnel junction.

Effect of Microcrystalline *n* Layer in the Tunnel Junction of *n i p n* and $n_1i_1p_1n_2i_2p_2$ Structure

We have reported before that *n i p n* is a very effective structure to evaluate properties of tunnel junctions for multijunction a-Si alloy cells (Guha 1994). Therefore, our first experiment is to compare the properties of the $n_1i_1p_1n_2$ structure with an amorphous n_2 layer to that with a microcrystalline n_2 layer. To reduce the variation caused by the "bottom" cell, all the $n_1i_1p_1$ component cells were cut from the same sample deposited over 1 ft x 1 ft area (2B3857). The results on $n_1i_1p_1n_2$ structures are tabulated in Table 28. Two different recipes were employed to deposit μc-n_2 layers, i.e., low and high H_2 dilution. Compared with the sample with a-n_2 layer, the two samples with μc-n_2 layers show higher J_{sc}, V_{oc}, FF, and Q at 550 nm. It appears that μc-n_2 layers give rise to better performance than a-n_2 layers.

As a natural extension of the experiment described above, i_2 and p_2 layers were subsequently deposited on the top of the $n_1i_1p_1n_2$ structure to complete the a-Si alloy double-junction solar cell. Surprisingly, the double-junction a-Si alloy cells with μc-n_2 layers show lower V_{oc} than the cell with a-n_2 layer (see Table 29). To check if the thickness of the μc-n_2 layer was large enough for double-junction cells, thicker μc-n_2 layers were deposited for some double-junction cells. It turned out that thicker μc-n_2 layers resulted in lower V_{oc} for double-junction cells than thin μc-n_2 layers. In extreme cases, thick μc-n_2 layer deposited with high H_2 dilution reduced double-junction cell V_{oc} by as much as 160 mV.

We postulated that there could be some incompatibility between the μc-n_2 and i_2 layers, and a thin proprietary buffer layer is inserted between μc-n_2 and a-i_2 layers. Characteristics of the double-junction cells with such combined μc-n_2/buffer layers are also listed in Table 29. The values of V_{oc} of the double-junction cells (#5403 and 5401) with μc-n_2/buffer layers are comparable to the cells with single a-n_2 layers (#5376 and #5402).

Experiments on $n_1i_1p_1n_2$ structure using the combination of μc-n_2 /buffer layers were performed to check whether there is still gain in Q. It is clear from Table 30 that the samples with combined μc-n_2/buffer layers show slightly higher values of Q at 550 nm, which indicates that the combined n_2 layers absorb less light than single a-n_2 layer (#5409).

We thus conclude that compared with amorphous *n* layers, μc-*n* layers have less absorption which reduces optical loss of the tunnel junction. Using a single μc-n_2 layer in the tunnel junction, double-junction cells show V_{oc} lowered by as much as 160 mV. The combination of μc-*n* and a thin buffer layer can provide the V_{oc} comparable to a-*n* layers with less absorption. Moreover, preliminary experimental results indicate that the combined μc-n_2/buffer layers may improve the quality of the tunnel junction in terms of lower contact resistance. We, therefore, decided to incorporate μc-*n* layers into the state-of-the-art multijunction cells.

Table 28. J-V Characteristics of $n_1i_1p_1n_2$ Structures.

Run #	J_{sc}	Q_{550}	V_{oc}	FF	Remarks
5369	11.2	0.70	0.916	0.592	a-n_2
5370	11.5	0.72	0.948	0.643	μc-n_2, Low H_2 dilution
5371	11.9	0.74	0.938	0.610	μc-n_2, High H_2 dilution

Table 29. Characteristics of a-/a- Alloy $n_1i_1p_1n_2i_2p_2$ Double-junction Structures.

Run #	V_{oc}	FF	Remarks
5376	1.804	0.652	a-n_2
5377	1.755	0.659	μc-n_2, Low H_2 dilution
5382	1.657	0.666	μc-n_2, High H_2 dilution
5384	1.782	0.640	μc-n_2, High H_2 dilution + buffer layer
5403	1.810	0.690	μc-n_2, High H_2 dilution + buffer layer
5401	1.819	0.645	μc-n_2, Low H_2 dilution + buffer layer
5402	1.797	0.636	a-n_2

Table 30. Q_{550} Characteristics of $n_1i_1p_1n_2$ Structures.

Run #	Q_{550}	Remarks
5409	0.67	a-n_2
5408	0.70	μc-n_2, Low H_2 dilution + buffer layer
5410	0.71	μc-n_2, High H_2 dilution + buffer layer

Effect of Microcrystalline *n* Layer in the Tunnel Junction of Double-junction Cells

As we have discussed above, there appears to be an advantage in replacing the amorphous *n* layer in the tunnel junction with a combination of microcrystalline *n* layer with buffer layers. The motivation is to see if the combination structure can provide an improved optical property (less optical loss) and/or an improved electrical property (less electrical loss) in the tunnel junction of a multijunction structure.

We have carried out a series of experiments on a-Si/a-Si and a-Si/a-SiGe alloy double-junction structures using conventional amorphous *n* layer and a combination of microcrystalline/ buffer layers in the tunnel junction. We have taken care to deposit the companion pairs onto the same back reflector; the pairs also have the same ITO deposited onto them. For the a-Si/a-SiGe alloy structure, we have used middle cell/top cell parameters from a typical triple-junction structure. The J-V characteristics are listed in Table 31, and the quantum efficiency curves are shown in Figs. 17-20. It is observed that the double-junction cells with microcrystalline n_2/buffer layer in the tunnel junction give rise to higher efficiencies; the series resistance is lower and the quantum efficiency is higher. The effect of incorporating this structure in a triple junction is discussed in Section 13.

Table 31. Characteristics of Double-junction Cells with Amorphous and Microcrystalline/Buffer *n* Layers in the Tunnel Junction.

Structure	*n* Layer in Tunnel Junction	J_{sc} (mA/cm^2)	V_{oc} (V)	FF	η (%)	Qtop/ Qbtm (mA/cm^2)	Qtotal (mA/cm^2)	R_s (Ω cm^2)
L8314 a-Si/a-Si	amorphous	7.80	1.901	0.752	11.15	7.97/ 7.8	15.77	15.0
L8317 a-Si/a-Si	microcrystalline/ buffer	8.06	1.919	0.766	11.85	8.06/ 8.28	16.34	14.3
L8375 a-Si/a-SiGe	amorphous	8.29	1.694	0.772	10.84	8.29/ 14.33	22.72	14.1
L8376 a-Si/a-SiGe	microcrystalline/ buffer	8.52	1.710	0.770	11.22	8.52/ 14.56	23.08	13.1

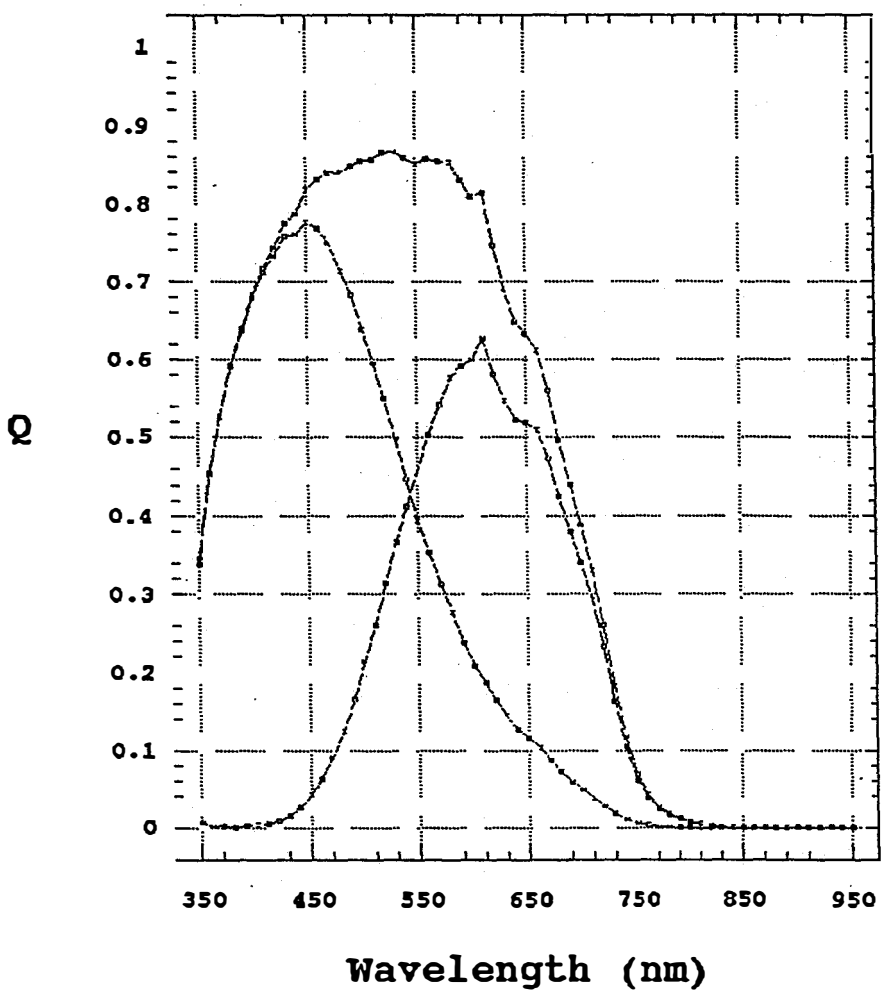

Figure 17. **Quantum efficiency versus wavelength of an a-Si/a-Si alloy double-junction cell (L8314) with an amorphous *n* layer in the tunnel junction.**

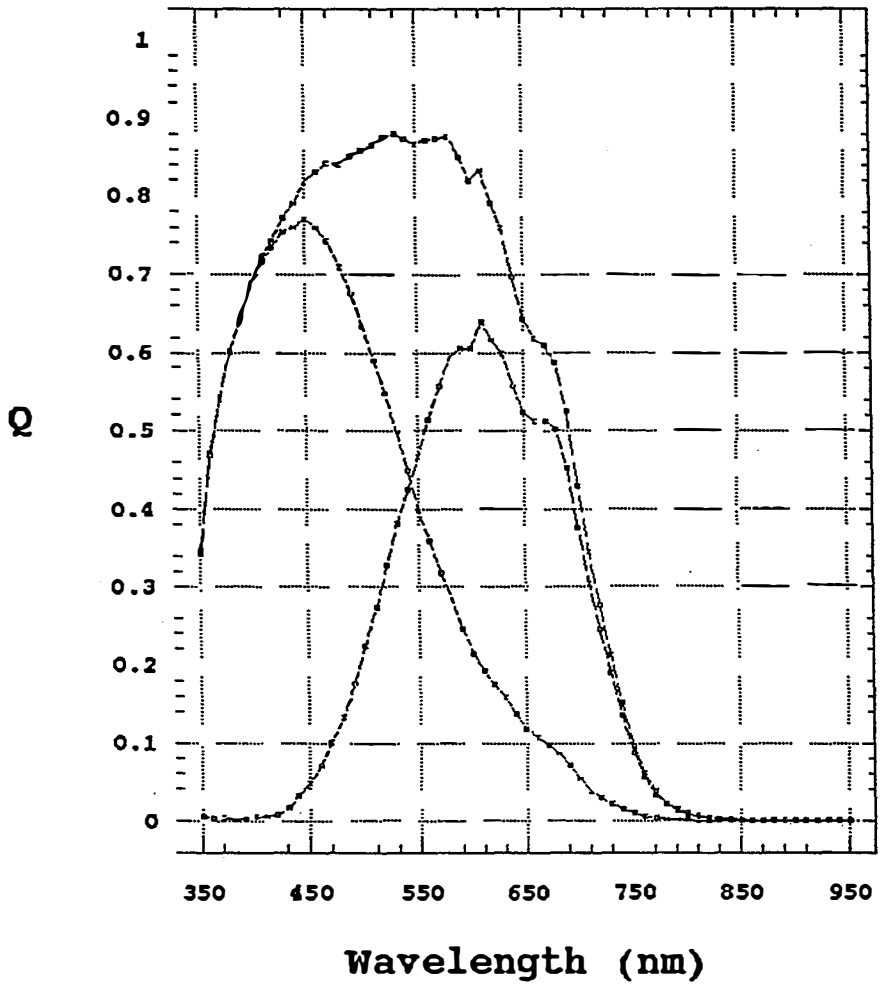

Figure 18. **Quantum efficiency versus wavelength of an a-Si/a-Si alloy double-junction cell (L8317) with a microcrystalline *n*/buffer combination in the tunnel junction.**

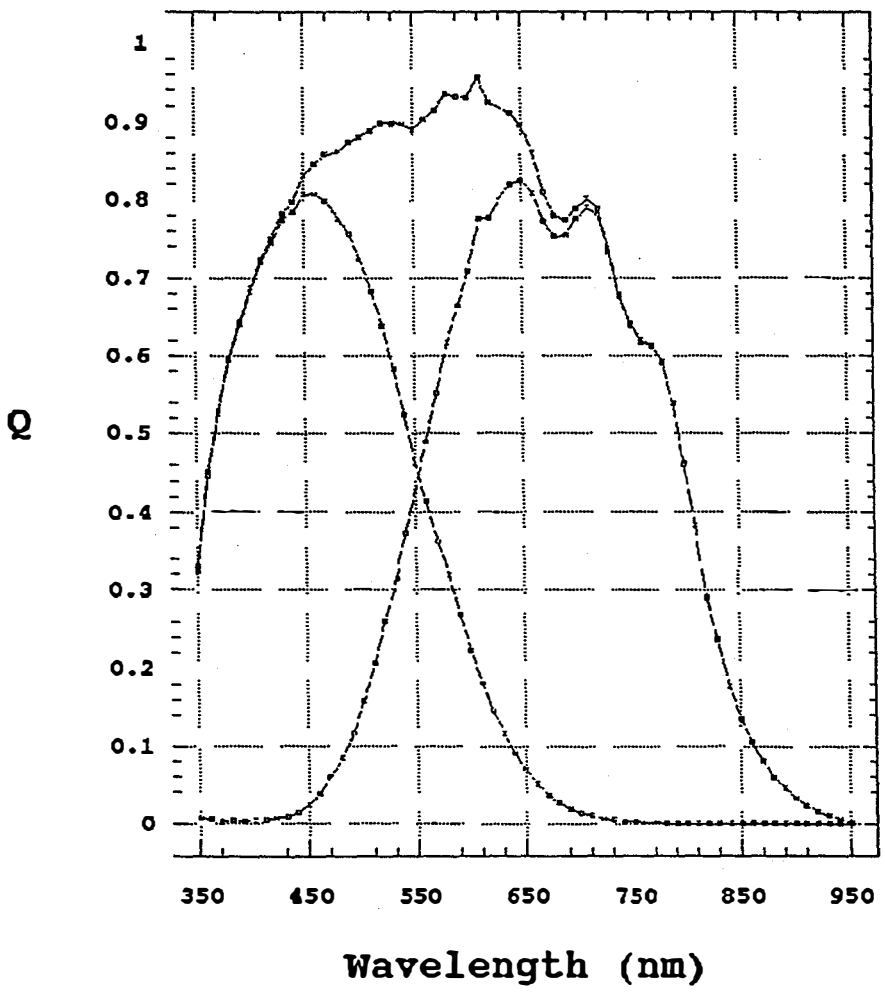

Figure 19. **Quantum efficiency versus wavelength of an a-Si/a-SiGe alloy double-junction cell (L8375) with an amorphous *n* layer in the tunnel junction.**

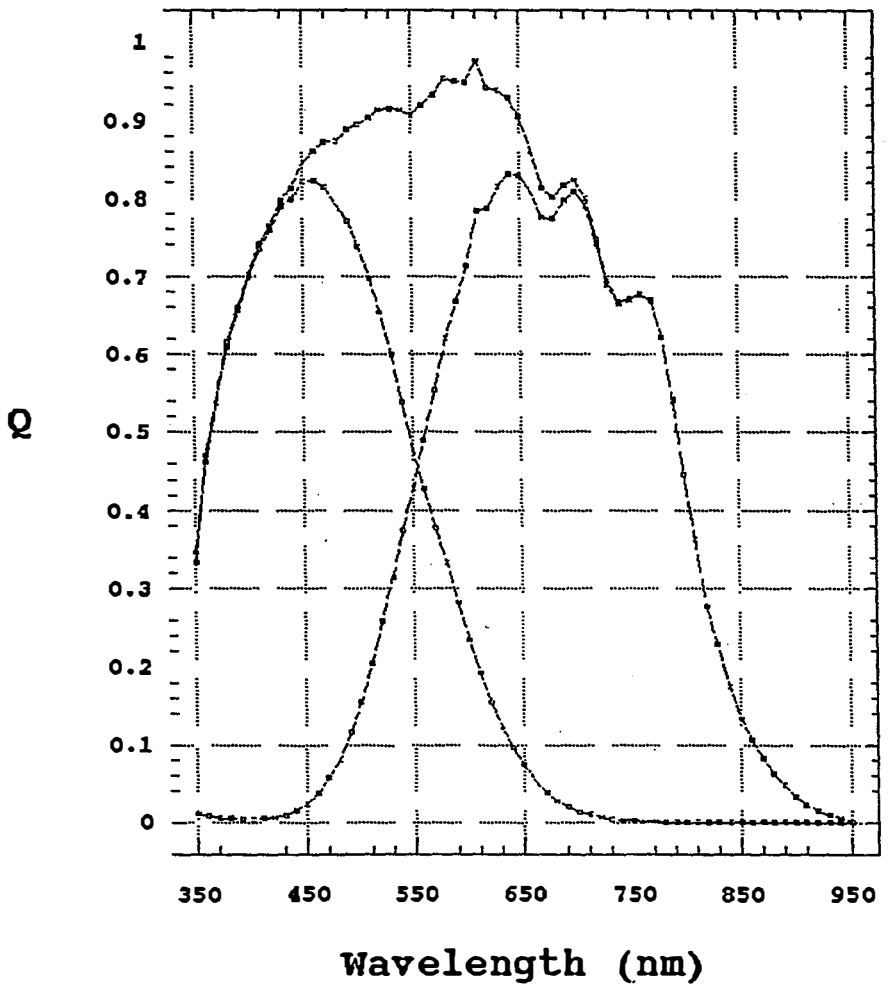

Figure 20. **Quantum efficiency versus wavelength of an a-Si/a-SiGe alloy double-junction cell (L8376) with a microcrystalline *n*/buffer combination in the tunnel junction.**

Section 12

Status of Component Cells for High Efficiency Triple-junction Solar Cells

Introduction

To achieve high efficiency triple-junction cells, several key issues need to be addressed. These include high quality (1) back reflectors, (2) top, middle, and bottom component cells, (3) "tunnel" junctions, (4) transparent conducting oxide, and (5) cell matching. This section discusses the status of component cells, Section 13 will address tunnel junction, transparent conducting oxide, and cell matching; back reflector optimization is within the scope of another NREL subcontract and will be reported separately.

Status of Component Cells

We should first mention that for the design of the component cells, our goal is to obtain high efficiency triple-junction cells having a J_{sc} of ≥8 mA/cm^2. This implies that each component cell should produce at least 8 mA/cm^2. nce the top and middle cells in a triple-junction configuration do not receive much reflected light, we deposited the top cell onto bare stainless steel substrates without any back reflector and the middle cell onto Cr coated textured back reflectors for evaluation.

For the top cell, we used a- alloy in the intrinsic layer made with high hydrogen dilution to improve the quality of the material. A microcrystalline *p* layer is used to enhance the built-in potential, reduce the optical loss, and improve the cell performance. The J-V characteristic of such a top cell exhibits an initial V_{oc} of 1.038 V, J_{sc} of 10.13 mA/cm^2, FF of 0.740, and efficiency of 7.78%. This is the highest efficiency value reported for a top cell for triple-junction applications and represents a significant improvement over Phase II status of 6.2%. The J_{sc} value of 10.13 mA/cm^2 is certainly sufficient for the top cell requirement.

For the middle cell, we used a high hydrogen diluted gas mixture of $_2H_6$ and GeH_4 in the *i* layer. The cell was deposited onto a standard back reflector but coated with Cr to reflect the fact that the middle cell does not receive much reflection from the substrate. The initial J-V characteristic measured with AM1.5 through a 530 nm cut-on filter shows V_{oc} = 0.753 V, J_{sc} = 9.30 mA/cm^2, FF = 0.687, and P_{max} = 4.81 mW/cm^2. The 530 nm filter was used to simulate the middle cell's insolation in a triple-junction structure. The current density of 9.3 mA/cm^2 measured through a 530 nm filter is appropriate for the middle cell in a triple-junction structure.

The bottom cell was deposited onto a textured Ag/ZnO back reflector and incorporated an a-Ge alloy *i* layer made using high hydrogen dilution and band gap profiling techniques. The initial J-V characteristic measured with AM1.5 through a 630 nm cut-on filter shows V_{oc} = 0.631 V, J_{sc} = 12.2 mA/cm^2, FF = 0.671, and P_{max} = 5.17 mW/cm^2. The initial power output of 5.17 mW/cm^2 is the highest reported to date and represents a significant improvement over Phase II status of 4.64 mW/cm^2. The quantum efficiency versus wavelength plot is shown in Fig. 21. It is noted that at 850 nm, the quantum efficiency is 45%, indicative of a high quality back reflector. Table 32 summarizes the initial characteristics of the component cells.

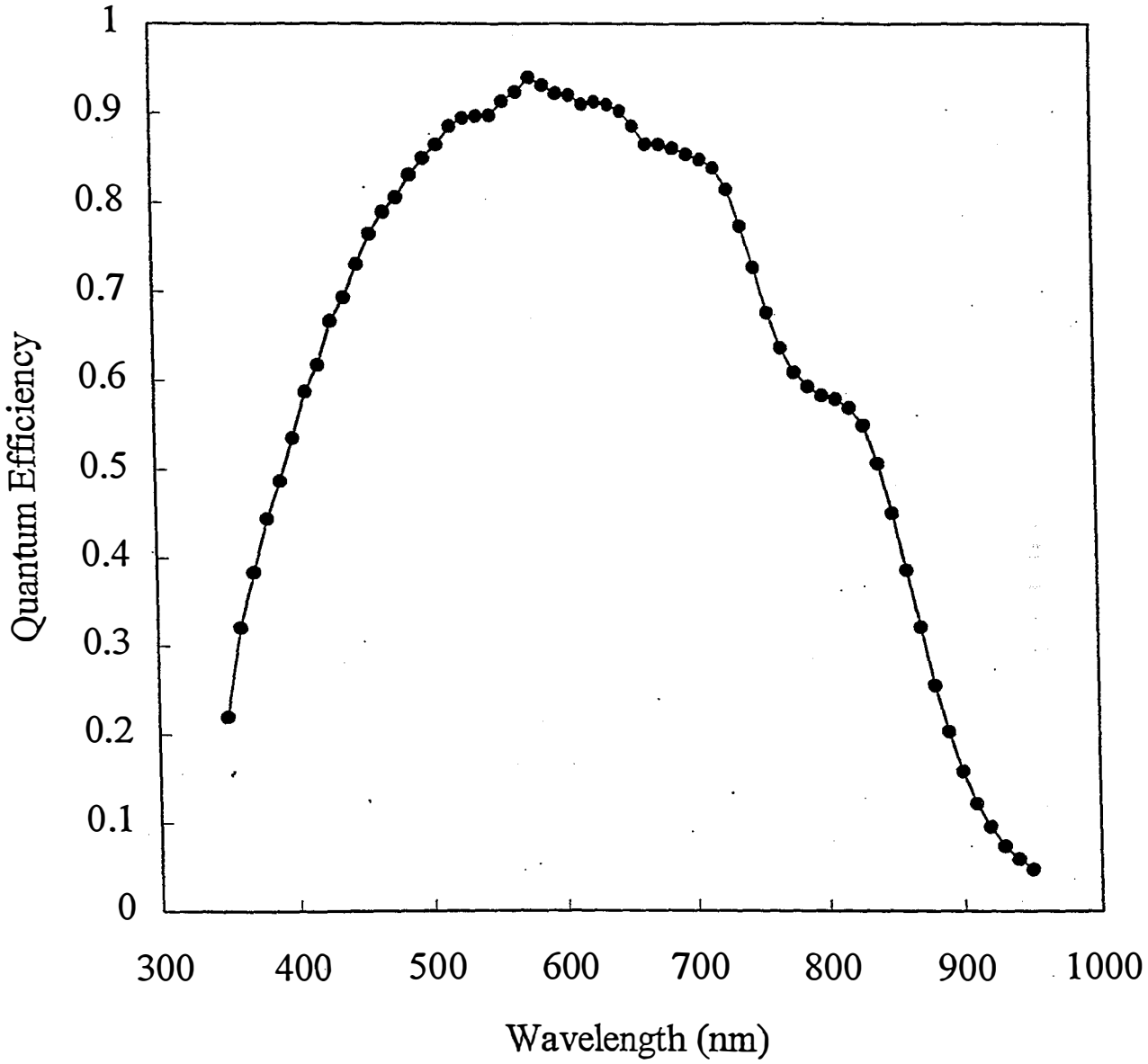

Figure 21. **Quantum efficiency of an a-SiGe alloy bottom cell on Ag/ZnO back reflector showing a 45% value at 850 nm.**

Table 32. Initial J-V Characteristics of the Top, Middle, and Bottom Component Cells.

Component Cell	J_{sc} (mA/cm^2)	V_{oc} (V)	FF	P_{max} (mW/cm^2)
Top[ad]	10.13	1.038	0.740	7.78
Middle[bc]	9.30	0.753	0.687	4.81
Bottom[cf]	12.2	0.631	0.671	5.17

[a] deposited onto bare stainless steel without back reflector

[b] deposited onto textured back reflector coated with Cr

[c] deposited onto textured Ag/ZnO back reflector

[d] measured under AM1.5 illumination

[e] measured under AM1.5 illumination with a 530 nm cut-on filter

[f] measured under AM1.5 illumination with a 630 nm cut-on filter

Stability of Component Cells

We used a metal-halide lamp with the intensity adjusted to one sun to study the stability of the component cells. For J-V measurements, the top cell was measured with AM1.5 illumination, while the middle and bottom cells were measured through 530 and 630 nm cut-on filters, respectively. All the component cells were light-soaked in the open-circuit mode and the temperature was maintained at 50 °C.

In general, the component cells show substantial saturation after ~200 hours of light-soaking, typical of high quality amorphous silicon alloy solar cells. Table 33 compares stabilized active-area cell efficiency for the top, middle, and bottom component cells to date and at the beginning of the program. One can easily note that significant progress has been made in the stabilized performance and should be reflected in the performance of the triple-junction structures to be discussed in the next section.

In order to obtain a 15% stable module efficiency, Guha et al. (Guha et al. 1994) has estimated that a 16% stabilized small-area cell efficiency is necessary. Table 33 also lists values estimated for reaching the 16% goal. One can see from Table 33 that J_{sc} values have substantially surpassed the goal while improvement needs to be made on V_{oc} and FF. This can only be met by innovative material research and device design with continued focused effort. This is particularly true for a-SiGe alloy material.

Table 33. Stabilized Active-area Component Cell Status at United Solar at the Beginning of the Program and Present.

Component Cell	Status	J_{sc} (mA/cm^2)	V_{oc} (V)	FF	P_{max} (mW/cm^2)
Top[a]	beginning[d]	7.2	0.98	0.71	5.0
	present[e]	8.78	0.953	0.709	5.93
	goal	8.2	1.10	0.75	6.8
Middle[b]	beginning[d]	6.9	0.74	0.57	2.9
	present[d]	8.92	0.717	0.587	3.75
	goal	8.4	0.89	0.70	5.2
Bottom[c]	beginning[f]	7.7	0.65	0.56	2.8
	present[f]	11.12	0.609	0.622	4.21
	goal	8.6	0.68	0.68	4.0

[a] measured under AM1.5
[b] measured under AM1.5 with a λ>530 nm filter
[c] measured under AM1.5 with a λ>630 nm filter
[d] deposited onto a textured substrate coated with Cr
[e] deposited onto a bare ss substrate
[f] deposited onto a textured Ag/ZnO substrate

Achieving Highest Stable a-Si Alloy Single-junction Cell Efficiency

The highest stable single-junction a-Si alloy solar cell efficiency of 8.9% was reported recently by Kameda et al. (Kameda et al. 1996). Since we have shown that hydrogen dilution improves the cell stability, we have recently conducted light-soaking experiments in single-junction a-Si alloy *p i n* solar cells on Ag/ZnO back reflector. After 1500 hours of one-sun light soaking at 50 °C, the degraded efficiency is 9.2%, establishing a new world record for this structure. Table 34 lists the initial and degraded J-V characteristics of the cells.

Table 34. Initial and Degraded (1500 hours) J-V Characteristics of a-Si Alloy Single-junction Cell with High Hydrogen Dilution and Deposited on Ag/ZnO Back Reflector.

Sample	Status	J_{sc} (mA/cm^2)	V_{oc} (V)	FF	P_{max} (mW/cm^2)
8934 #33	Initial	15.6	0.983	0.692	10.6
	Degraded (1500 hours)	15.0	0.949	0.645	9.2
	Degradation (%)	3.8	3.5	6.8	13.4

Section 13

Achievement of 13% Stable Active-area Efficiency

Introduction

As discussed in the previous section, significant improvement has been made in the performance of component cells. In addition to incorporating the component cell results into the triple-junction structure, component cell current mismatch and tunnel junction characteristics need to be optimized. At the end of Phase II of this program, we reported the achievement of an 11.8% stable active-area cell efficiency. In this section, we discuss the three key improvements that enabled us to achieve record 14.6% initial and 13.0% stable active-area cell efficiencies.

Experimental Results and Discussion

Figure 22 shows a schematic diagram of the triple-junction structure. The top intrinsic (*i*) layer uses wide bandgap a-Si alloy for absorbing the blue photons, while the middle and bottom *i* layers incorporate intermediate and narrow bandgap amorphous silicon-germanium (a-SiGe) alloys for absorbing the green and red photons, respectively. A textured silver/zinc-oxide back reflector is used to facilitate light trapping (Ross et al. 1987). The red photons that reach the back surface are scattered back at an oblique angle so as to enhance the optical path and provide additional absorption. The top contact uses indium-tin-oxide (ITO) which also serves as an antireflection coating. Finally, a metal grid is deposited on top of ITO for collecting current.

All the three *i* layers use high hydrogen dilution during film growth to obtain superior quality (Yang et al. 1994), and the middle and bottom a-SiGe *i* layers employ bandgap profiling for better carrier collection (Guha et al. 1989). Microcrystalline *p* layers with high conductivity and low optical absorption (Guha et al. 1986) are used as the window layer as well as in the tunnel junctions.

Using the above approach, along with an appropriate current mismatching cell design, we recently obtained a triple-junction cell with 13.2% initial and 11.8% stable efficiencies (Yang et al. 1996). Figure 23 plots the initial quantum efficiency data for this device. It is noted that the total photocurrent generated in the triple stack is ~25 mA/cm^2.

A careful analysis of Fig. 23 reveals that one can possibly further improve the spectrum response in three areas: (a) the red response in the long wavelength (λ>800 nm) region, (b) the response associated with the absorption of the tunnel junction between the top and the middle cells in λ~500-600 nm region, and (c) the blue response in the short wavelength (λ<450 nm) region.

The Red Response

One way to enhance the red response, hence increasing the triple-cell current with desired current mismatch, is to increase the germanium content in the bottom cell. This, however, often results in a poorer material quality and deteriorates the cell performance. Using high hydrogen dilution during film growth and incorporating proper bandgap profiling, we have improved the bottom component cell with an enhanced red performance. Table 35 compares the performance of the previous and recent bottom cells measured under AM1.5 illumination through a λ>630 nm red filter. It is readily observed that the recent

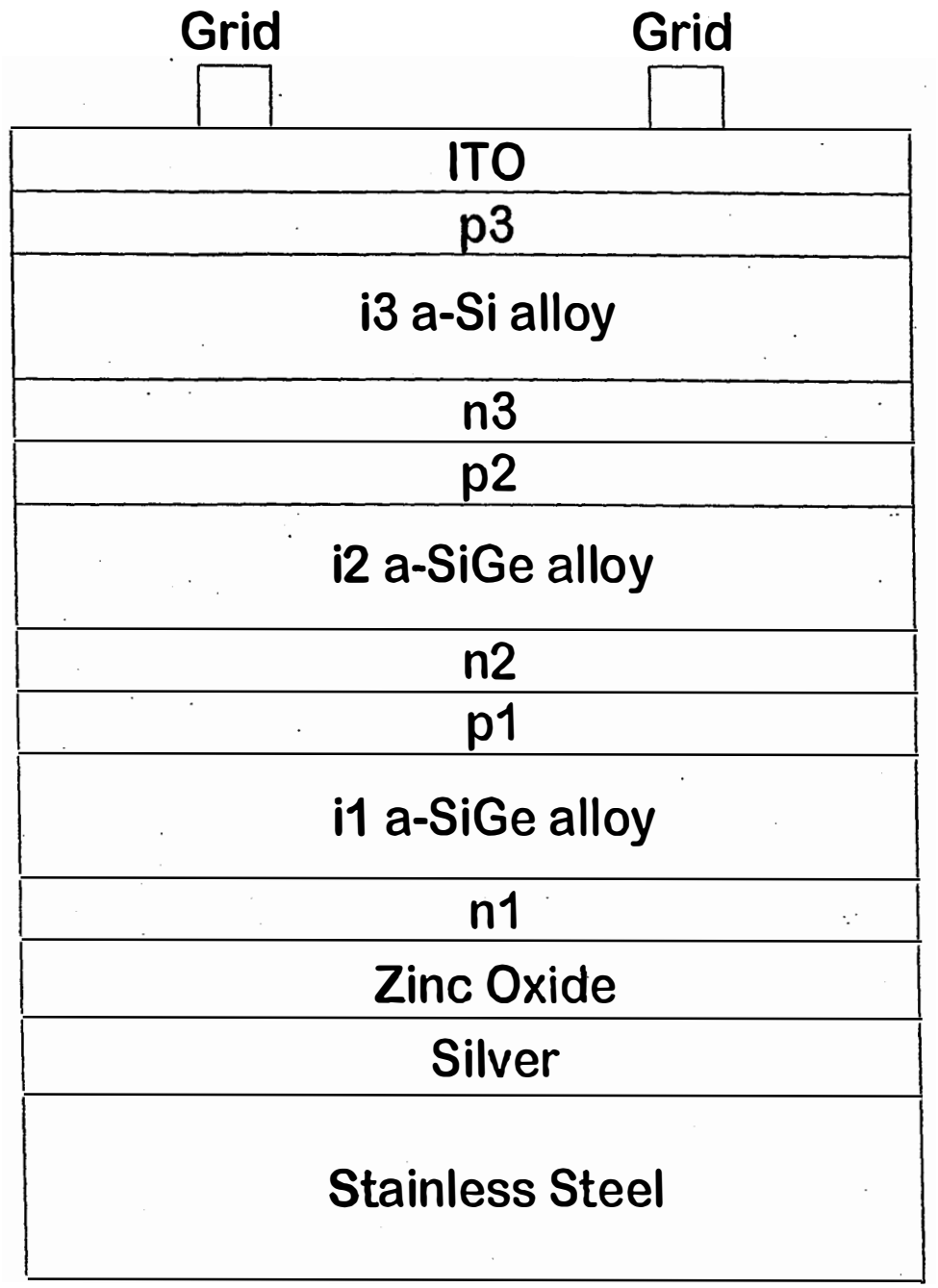

Figure. 22. Schematic diagram of a triple-junction cell structure.

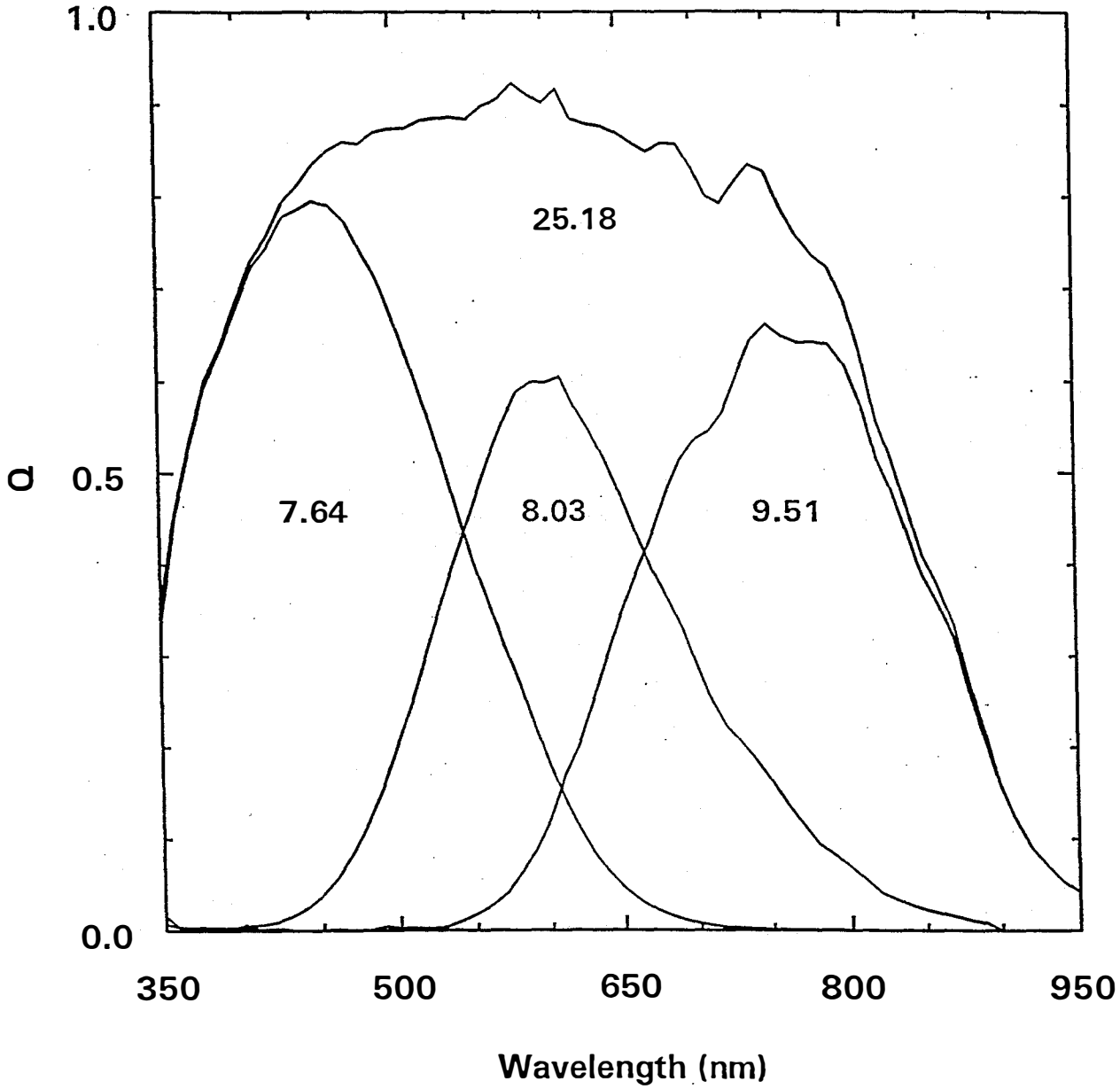

Figure 23. Initial quantum efficiency of the previous best triple cell.

cell has a higher red current and improved output power. The higher V_{oc} and FF demonstrate the benefit of proper hydrogen dilution and bandgap profiling. Since the previous cell was used to obtain the 11.8% stable device, the improved cell should set a good foundation for a triple-junction structure. The improved bottom cell under AM1.5 illumination shows J_{sc} = 24.4 mA/cm^2, V_{oc} = 0.662 V, FF = 0.643, and an AM1.5 efficiency of 10.4%. The quantum efficiency data for this device reveal that at 850 nm the collection is 45%, a significant improvement over the 35% value reported for the previous bottom cell (Yang et al. 1996).

Table 35. Initial J-V Characteristics of Previous and Recent Bottom a-SiGe Cells Measured under AM1.5 Illumination with a λ>630 nm Filter.

	J_{sc} (mA/cm^2)	V_{oc} (V)	FF	P_{max} (mW/cm^2)
Previous	11.9	0.611	0.634	4.6
Recent	12.2	0.631	0.671	5.2

The Tunnel Junction

There are two tunnel junctions in the triple structure (see Fig. 22). One is p_2n_3 between the top and the middle cells, and the other is p_1n_2 between the middle and the bottom cells. These tunnel junctions, while essential in the triple-cell operation, result in optical and electrical losses. Any reduction in their optical absorption or electrical resistance, for example, by using microcrystalline doped layers, should give rise to a better cell performance. In our earlier triple-junction cells, we have used microcrystalline *p* layer but amorphous *n* layer in the tunnel junctions.

Since the p_2n_3 top tunnel junction is closer to where light enters the device than the p_1n_2 junction, any improvement in the top tunnel junction is expected to result in a larger improvement in the cell performance. To evaluate the top tunnel junction, we first studied two a-Si/a-Si double-junction cells. The only difference between the two cells is that one uses an amorphous *n* layer while the other uses a microcrystalline *n* layer in the tunnel junction. To our surprise, we find that the V_{oc} value for the tandem cell having a microcrystalline *pn* junction is much lower (V_{oc}=1.657 V) than the corresponding one (V_{oc}=1.804 V). We attribute the lowering of V_{oc} to the following two reasons: (a) The microcrystalline *n* layer may have much lower bandgap than the amorphous *i* layer, and the band edge discontinuity (Xu et al. 1995) may cause the lowering of V_{oc}. (b) The deposition conditions for microcrystalline material generally require high rf power and high hydrogen dilution (Guha et al. 1986). These conditions can cause the intermixing of the dopants in the thin doped layers, thus lowering the V_{oc}.

We have developed novel buffer layers and inserted them between the microcrystalline *p* and *n* layers, and between the microcrystalline *n* and amorphous *i* layers. We then compared the a-Si/a-Si double-junction performance by using a conventional amorphous *n* layer, and a microcrystalline *n* layer sandwiched between buffer layers in the tunnel junction. We have taken care to deposit the companion pairs onto the same back reflector; the pairs also have the same ITO deposited onto them. The results are listed in Table 36. It is observed that the microcrystalline *pn* multilayered structure gives rise to cells with higher J_{sc}, V_{oc}, FF, total current, and efficiency. The higher total current and lower series resistance demonstrate the improvement due to the new tunnel junction structure.

Table 36. Characteristics of a-Si/a-Si Double Junctions with Different Tunnel Junction Structures.

Tunnel Junction Structures	J_{sc} (mA/cm^2)	V_{oc} (V)	FF	η (%)	Qtop/Qbtm (mA/cm^2)	Qtotal (mA/cm^2)	R_s (Ω cm^2)
microcrystalline *p* amorphous *n*	7.80	1.901	0.752	11.15	7.97/7.80	15.77	15.0
microcrystalline *p* multilayered *n*	8.06	1.919	0.766	11.85	8.06/8.28	16.34	14.3

The Blue Response

As mentioned earlier, the top conducting oxide serves as the top contact (see Fig. 22) as well as an antireflecting coating. If one can reduce the absorption in ITO without sacrificing its conductivity, one can gain in photocurrent. This will benefit the entire triple stack with the top cell receiving the most advantage. We have reoptimized the ITO deposition conditions by adjusting the oxygen partial pressure and obtained a higher ITO transmission. A top cell with the improved ITO shows a J_{sc} value ~0.5 mA/cm^2 higher than that obtained with previous ITO. The higher current is achieved without increasing the *i* layer thickness, which is certainly desirable from the stability point of view. A J_{sc} value of ~8.5 mA/cm^2 is also suitable for the top cell of a triple structure with the improved bottom component cell.

The Triple-junction Cell

Incorporating the improvements described above, we then proceeded to make triple-junction cells with microcrystalline *p* and multilayered *n* structure in both tunnel junctions. Several triple cells with initial efficiencies exceeding 14% were obtained. The highest efficiency achieved is 14.6%, representing a 10% improvement over our previous record of 13.2% (Yang et al. 1996).

Figure 24 shows the J-V characteristic of the 14.6% triple-junction cell. Compared to our earlier best triple cell, J_{sc} is increased significantly from 7.64 to 8.57 mA/cm^2, while V_{oc} and FF have similar values. Quantum efficiency data shown in Fig. 25 reveal that the total photocurrent from the triple stack is 26.88 mA/cm^2, a significant increase from our earlier value of 25.18 mA/cm^2.

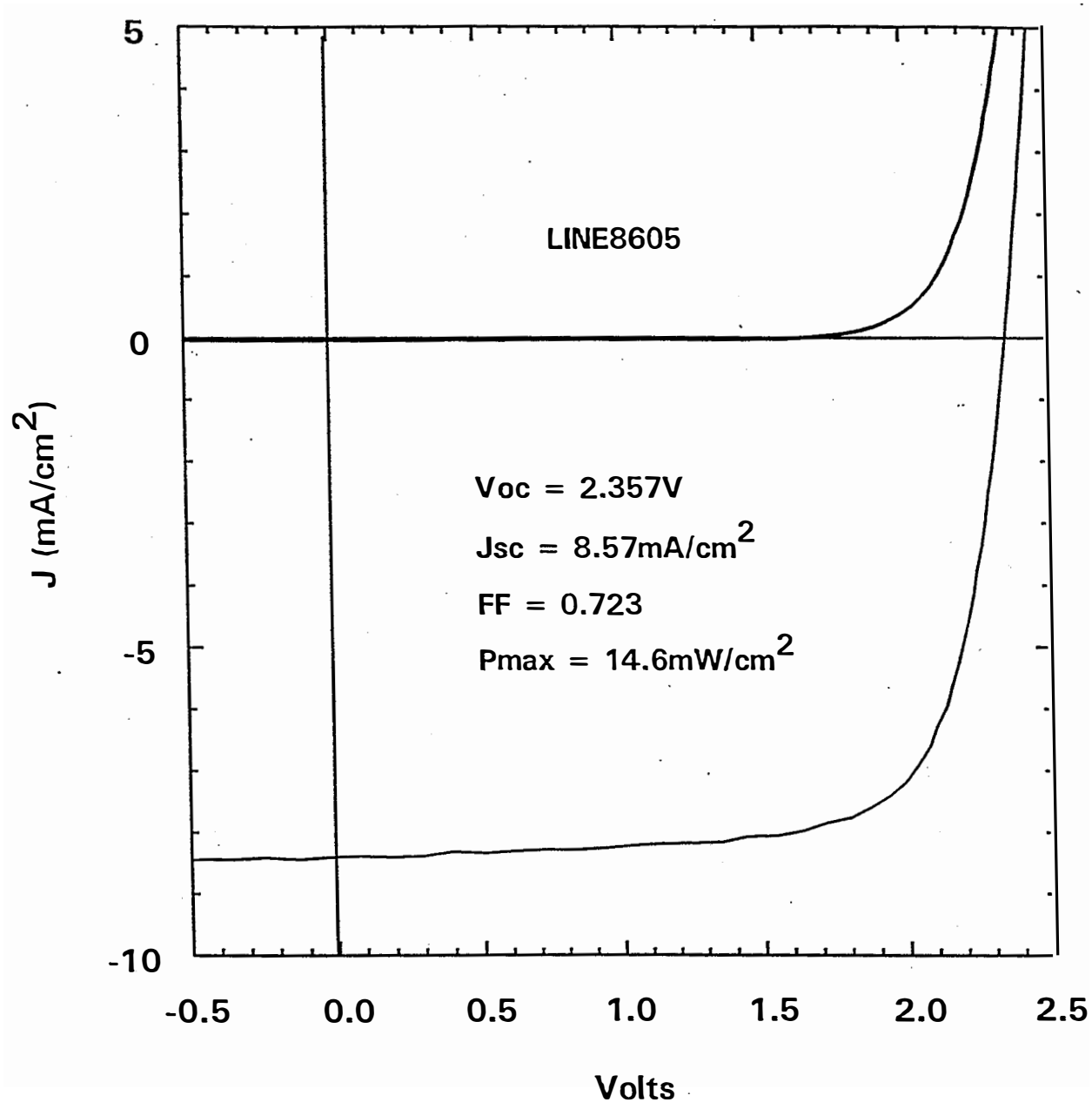

Figure 24. Initial J-V characteristics of the 14.6% triple-junction cell.

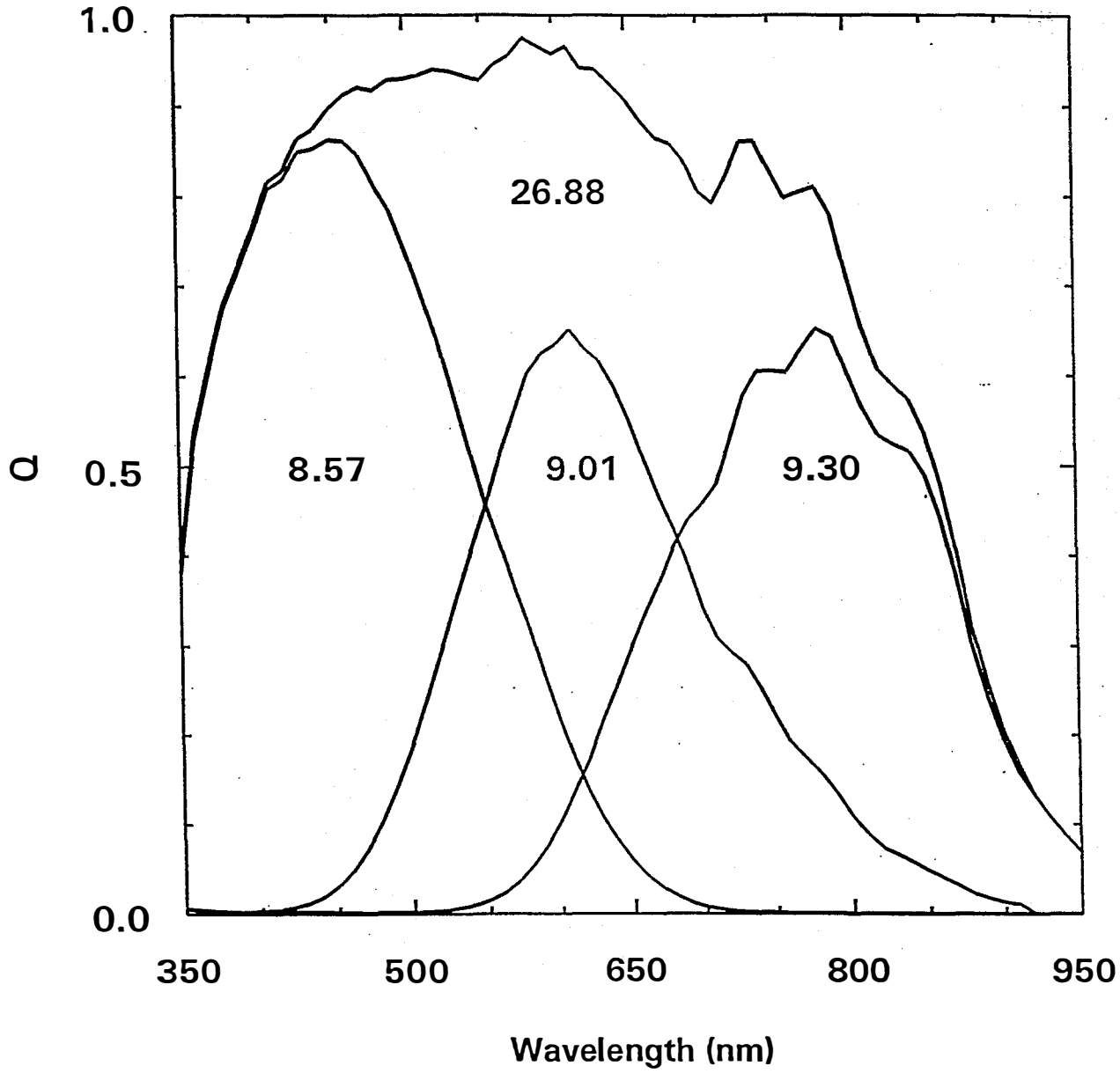

Figure 25. Quantum efficiency of the triple cell in Fig. 24.

Comparing Figs. 23 and 25, one can readily see that (a) the quantum efficiency for λ>800 nm is increased significantly due to the improvement in the red response; (b) the quantum efficiency for λ~500-600 nm region is improved due to the new tunnel junction structure; and (c) the overall quantum efficiency is enhanced, especially for the λ<450 nm region, due to the improvement in ITO. We indeed benefit from the three improvements discussed above.

Several devices were sent to NREL for triple-source measurement. Table 37 summarizes the data obtained at NREL and United Solar, demonstrating an excellent agreement between the two laboratories. It should be pointed out that the J_{sc} value at United Solar is based on quantum efficiency measurement. NREL measures the total area efficiency only; the active-area current density is obtained by subtracting the grid coverage from the total area.

Table 37. Initial and Stable Triple Cell Efficiency (active area of ~0.25 cm^2) as Measured at United Solar and NREL.

Device L8605	V_{oc} (V)	I_{sc} (mA)	FF (%)	J_{sc} (total area) (mA/cm^2)	η (%)	J_{sc} (active area) (mA/cm^2)	η (%)	Measurement Laboratory
Initial	2.357		72.3			8.57	14.6	United Solar
Initial	2.357	2.104	74.39	7.721	13.5	8.28	14.5	NREL
Stable	2.294		68.4			8.27	13.0	United Solar
Stable	2.297	2.061	69.7	7.563	12.1	8.11	13.0	NREL

These devices were subsequently subjected to light soaking under one-sun, 50 °C, and open-circuit conditions. After ~300 hours of light soaking, their performance was substantially stabilized. The best stabilized efficiency after 1000 hours is 13.0%; it is again independently confirmed by NREL (Table 37). This is the highest stable efficiency achieved for amorphous silicon alloy solar cells.

Analysis of High Efficiency Triple Cells

In order to evaluate the impact of the individual component cell on the performance of the high-efficiency device, we have analyzed the photovoltaic characteristics of the component cells made using the same parameters as those incorporated into the triple structure. The initial J-V characteristics measured under various illumination conditions are summarized in Table 38. The following observations are made for the initial performance:

1. The top cell exhibits the best fill factor. Therefore, it is desirable to design the triple structure using the top cell as the current-limiting cell, especially in the degraded state. Although the top cell is deposited onto a bare stainless steel substrate without any back reflector, it still receives some reflection from the substrate. This explains the somewhat smaller J_{sc} value in the triple configuration.

Table 38. Initial and Light-soaked J-V Characteristics of the Component and Triple-junction Cells at United Solar.

Cell	Status	J_{sc} (mA/cm^2)	V_{oc} (V)	FF	P_{max} (mW/cm^2)
top[d]	initial[a]	8.97	0.980	0.761	6.69
middle[e]	initial[b]	9.30	0.753	0.687	4.81
bottom[f]	initial[c]	12.2	0.631	0.671	5.17
triple[d]	initial[c]	8.57	2.357	0.723	14.6
top[d]	1994 stable[b]	7.3	0.97	0.72	5.1
	1997 stable[a]	8.78	0.953	0.709	5.93
middle[e]	1994 stable[b]	7.6	0.76	0.60	3.5
	1997 stable[b]	8.92	0.717	0.587	3.75
bottom[f]	1994 stable[c]	9.84	0.67	0.55	3.60
	1996 stable[c]	11.4	0.60	0.56	3.80
	1997 stable[c]	11.12	0.609	0.622	4.21
triple[d]	1995 stable[c]	6.87	2.38	0.68	11.1
	1996 stable[c]	7.49	2.283	0.692	11.8
	1997 stable[c]	8.27	2.294	0.684	13.0

a deposited on a bare stainless steel substrate
b deposited on a textured substrate coated with Cr
c deposited on textured Ag/ZnO back reflector
d measured under AM1.5 illumination
e measured under AM1.5 with a λ>530 nm filter
f measured under AM1.5 with a λ>630 nm filter

2. The photocurrent generated by the top, middle, and bottom component cells for the 14.6% triple cell are respectively 8.57, 9.01, and 9.30 mA/cm^2. The bottom component cell in Table 38 shows 12.2 mA/cm^2 for J_{sc}, much higher than 9.30 mA/cm^2 obtained from the quantum efficiency measurement. The 630 nm filter used to evaluate the bottom cell may be insufficient for the narrow bandgap amorphous silicon-germanium bottom cell that we have recently developed. We need to use a longer wavelength filter so that the J_{sc} value will more appropriately simulate the operation of the bottom cell in a triple stack. However, to evaluate the progress in cell technology, the 630 nm filter is still used.

3. A simple arithmetic sum of the V_{oc} values of the component cells in the initial and light-soaked states give composite V_{oc} values within 1% of the corresponding triple-junction V_{oc} values.

4. Based on the above observations, one notices that in the triple-junction operation, J_{sc} is basically dictated by the top cell, V_{oc} is simply the sum of the individual V_{oc} values, and FF is governed by the top cell and the mismatch of the component cells. The initial triple-cell performance can be projected using the component cell characteristics.

To corroborate the performance of the triple cell after light soaking and the above analysis, we have carried out indoor light-soaking experiments using the same procedure as reported previously. The stable characteristics are tabulated in Table 38 under 1997 values. The observations made for the initial states hold true for the degraded states as well. We have also listed in Table 38 stabilized performance obtained at United Solar since the beginning of the Thin Film Partnership Program in 1994. The component cells in 1994 led to the achievement of 11.1% stable triple cell in 1995. The improvement in the bottom cell in 1996 as well as the current mismatch consideration resulted in the 11.8% stable triple-cell efficiency in 1996. The advances in the stabilized component cells, particularly the enhancement of J_{sc} resulted from improving the spectral response in the wavelength range of 300 to 1000 nm, help achieve the high efficiency.

Temperature Coefficient of High Efficiency Triple-junction Solar Cells

The three critical parameters that determine the efficiency of a solar cell, namely, open-circuit voltage, short-circuit current density and fill factor, all depend on the operating temperature. As the temperature increases, the open-circuit voltage decreases, the short-circuit current density increases, and the fill factor may increase or decrease depending on the design of the cell. For a triple-junction cell, the situation is more complex since the fill factor quite often is determined by that of the limiting cell and the degree of current mismatch among the different cells. It is, therefore, of interest to study the effect of current mismatch on the temperature coefficient of high efficiency triple-junction cells.

We have selected three devices with current matching conditions obtained from quantum efficiency measurements (Table 39). It is noted from Table 39 that while the devices exhibit different component cell current distributions, their total current remains constant. For L9323, Q_{top}, Q_{middle} and Q_{bottom} have similar values; for L9329, Q_{top} and Q_{middle} have similar values, but Q_{bottom} is substantially larger; for L9330, Q_{middle} and Q_{bottom} have similar values, and Q_{top} is substantially smaller.

Table 39. Component Cell Current Distribution for Three Triple-junction Solar Cells.

Device	Q_{top} (mA/cm^2)	Q_{middle} (mA/cm^2)	Q_{bottom} (mA/cm^2)	Q_{total} (mA/cm^2)
L9323	8.27	8.47	8.74	25.5
L9329	7.81	8.18	9.41	25.4
L9330	7.86	8.77	8.89	25.5

We measured the J-V characteristics for the three devices in the temperature range of 25 °C to 65 °C and plotted their characteristics in Figs. 26 and 27. From these two figures, we observe that the slope of efficiency versus temperature, i.e., the temperature coefficient, is similar for all three samples. In other words, the temperature coefficiency is rather insensitive to the current mismatch conditions. We plan to study the temperature coefficient of these devices in the light-soaked state. The experimental result will be useful in the component cell mismatch design for photovoltaic products.

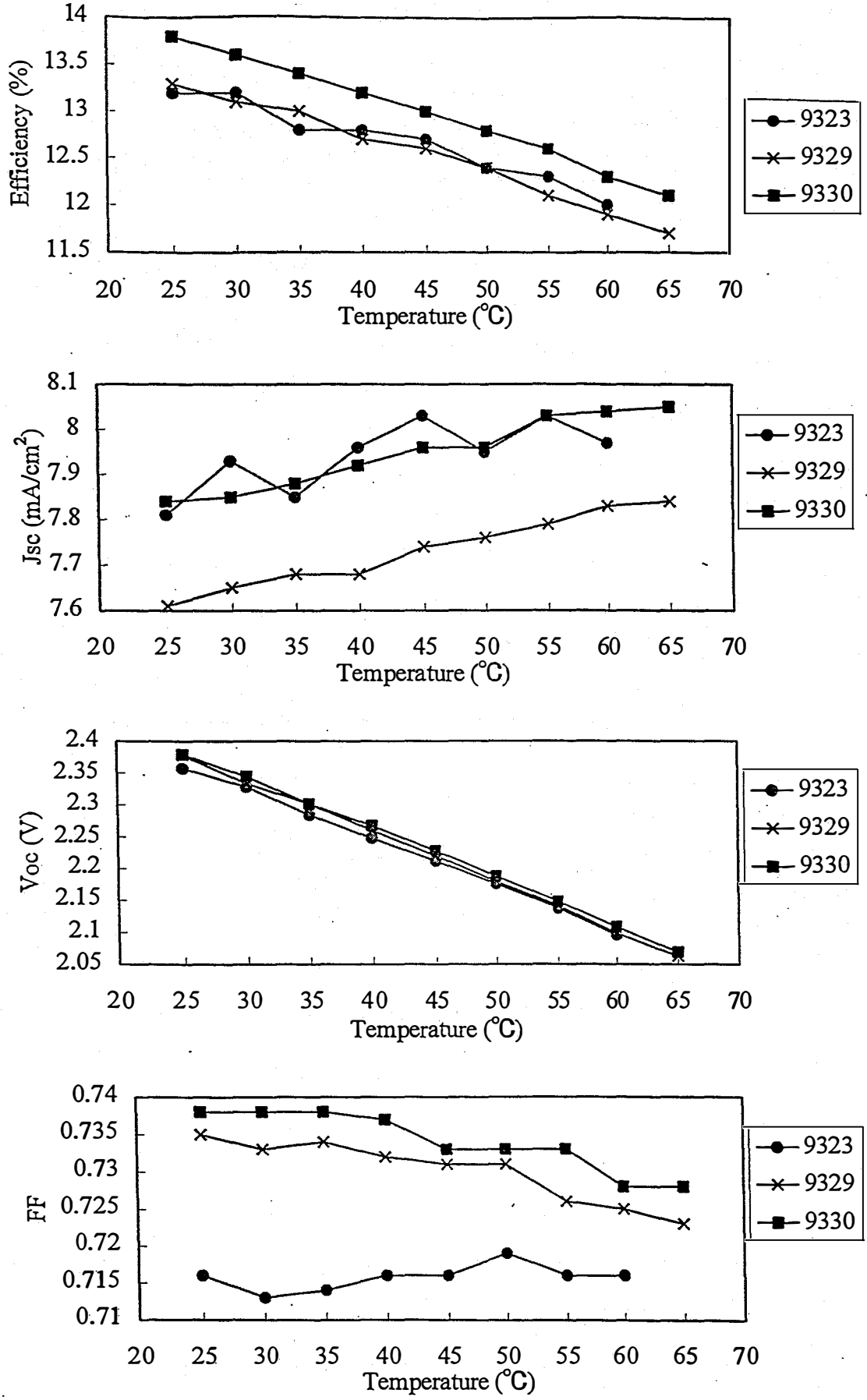

Figure 26. Temperature dependence of Eff., J_{sc}, V_{oc}, and FF of samples L9323, L9329, and L9330.

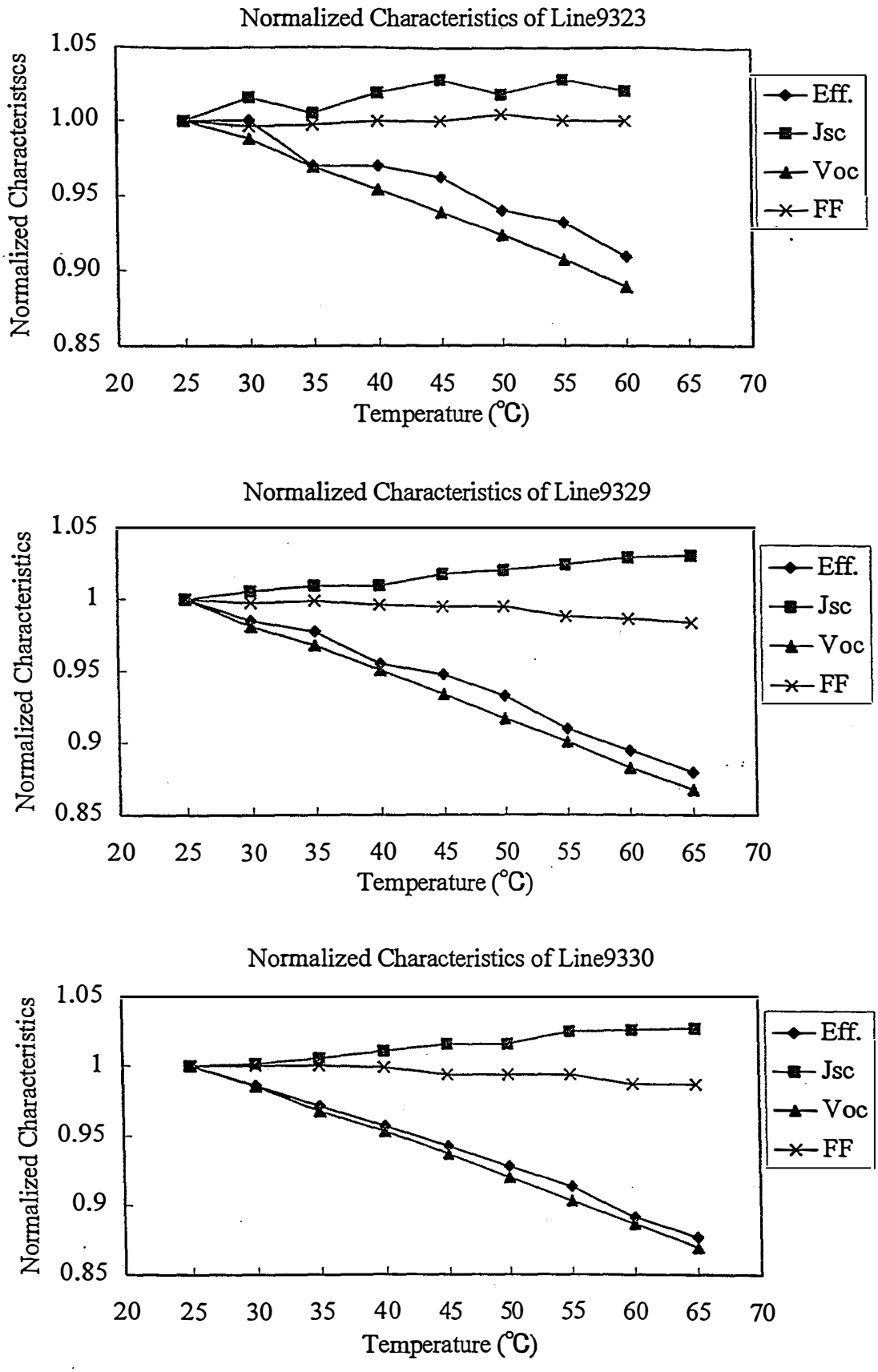

Figure 27. Temperature dependence of Eff., J_{sc}, V_{oc}, and FF of samples L9323, L9329, and L9330.

Section 14

Status of Component Cells and Triple-junction Devices with Intrinsic Layers Deposited at 3 Å/s

Introduction

As can be seen from the previous sections, significant progress has been made in increasing the stable efficiency of a-Si alloy solar cells. The highest efficiency values are usually obtained when the intrinsic layers in the cells are deposited at a rather low rate (typically 1 Å/s). Increasing the deposition rate usually lowers the efficiency, but a significant reduction in manufacturing cost can be achieved if high efficiency cells with good stability can be made at higher deposition rates. We have investigated the top, middle, and bottom component cells as well as triple-junction devices in which the intrinsic layers are deposited at ~3 Å/s, and will summarize the preliminary results in this section.

Results and Discussion

During the optimization process, we have used hydrogen dilution in the gas mixture, and incorporate all the know-how that we have developed for achieving high efficiency multijunction solar cells. Table 40 summarizes the best component cells and triple-junction devices in both the initial and stabilized states. It is obvious that cells made at higher rates show poorer stabilized efficiencies compared to those made at lower rates. With focused effort and innovative approach, one may be able to bridge the gap and achieve higher performance.

Table 40. Status of Initial and Stabilized Solar Cells Deposited at 3 Å/s.

Cell	Status	Active-area J_{sc} (mA/cm^2)	V_{oc} (V)	FF	P_{max} (mW/cm^2)
Top[ad]	Initial	8.73	0.967	0.749	6.32
	Stabilized	8.56	0.904	0.646	5.00
Middle[bd]	Initial	8.73	0.742	0.666	4.31
	Stabilized	8.17	0.694	0.539	3.06
Bottom[ce]	Initial	10.62	0.62	0.63	4.15
	Stabilized	10.11	0.594	0.564	3.39
Triple[ae]	Initial	8.09	2.265	0.689	12.6
	Stabilized	7.63	2.18	0.614	10.2

[a] measured under AM1.5
[b] measured under AM1.5 with a λ>530 nm filter
[c] measured under AM1.5 with a λ>630 nm filter
[d] deposited onto a bare ss substrate
[e] deposited onto a textured Ag/ZnO substrate

Section 15

Future Directions

Significant progress in stable efficiency of both component and triple cell structures has been shown during this program. The increase in efficiency has been achieved through a better understanding of the role of precursor gases and their effect on growth kinetics. Innovative device design to reduce tunnel junction losses has also played an important role. Our fundamental studies will continue, and we expect to see continuous improvements in efficiency through these efforts.

A major focus of the future programs will, however, be devoted toward the improvement of cell performance at higher deposition rates. The best cells are made at around 1 Å/s; to reduce capital cost for a given throughput, the production machines typically use deposition rates of around 3 Å/s. The higher deposition rates give rise to poorer efficiency. Improvement of efficiency for cells deposited at high rates will have a significant effect on product cost and acceptability. We shall investigate different deposition regimes to understand the plasma chemistry and growth kinetics at high rates so as to optimize cells at rates between 3-5 Å/s.

References

Arch, J.K.; Rubinelli, F.A.; Hou, J.Y.; Fonash, S.J. (1991). *J. Appl. Phys.*; Vol. 69, p. 7057.

Arya, R.R.; Catalano, A.; Oswald, R.S. (1986). *Appl. Phys. Lett.;* Vol. 49, p. 1089.

Banerjee, A.; Yang J.; Glatfelter, T.; Hoffman K.; Guha, S. (1994). *Appl. Phys. Lett.;* Vol. 64, p. 1517.

Banerjee, A.; Yang, J.; Hoffman, K.; Guha, S. (1994). *Appl. Phys. Lett.*; Vol. 65, p. 472.

Banerjee, A.; Hoffman, K.; Xu, X.; Yang, J.; Guha, S. (1994). *First World Conference on Photovoltaic Energy Conversion Proc.;* p. 539.

Banerjee, A. (1995). *Solar Energy Materials and Solar Cells;* Vol. 36, p. 295.

Banerjee, A.; Xu, X.; Yang, J.; Guha, S. (1995). *Mat. Res. Soc. Proc.*; Vol. 377, p. 675.

Cabarrocas, P. Roca i.; Morin, P.; Chu, V.; Conde, J.P.; Liu, J.Z.; Park, H.R.; Wagner, S. (1991). *J. Appl. Phys.;* Vol. 69, p. 2942.

Chen, I.; Wronski, C.R. (1995). *J. Non-Cryst. Solids;* Vol. 190, p. 58.

Cuniot, M.; Marfaing, Y. (1988). *Philos. Mag.*; Vol. B 57, p. 291.

See, for, example, Curtins, H.; Favre, M. (1989). *Amorphous Silicon and Related Materials, Vol. A.* Edited by H. Fritzsche (Advances in Semiconductors, Vol. 1, World Scientific Publishing Co., Singapore, 1989) p. 329.

Dalal, V. L. (1995). NREL Quarterly Report, June-Aug.

Delley, B.; Steigmeier, E.F. (1993). *Phys. Rev.*; Vol. B47, p. 1397.

Doughty, D.A.; Doyle, J.R.; Lin, G.H.; Gallagher, A. (1990). *J. Appl. Phys.*; Vol. 67, p. 6220.

Drevillion, B.; Toulemonde, M. (1985). *J. Appl. Phys.*; Vol. 58, p. 1.

Evangelisti, F. (1985). *J. Non-Cryst. Solids;* Vol. 77&78, p. 969.

Fantoni, A.; Vicira, M.; Martins, R. (1994). *Mat. Res. Soc. Proc.*; Vol. 336, p. 711.

Gallagher, A.; Barzen, S.; Childs, M.; Laracuente, A. (1996). *Atomic-Scale Characterization of Hydrogenated Amorphous-Silicon Films and Devices.* NREL/SR-520-22565. Golden, CO: National Renewable Energy Laboratory. Work performed at National Institute of Standards and Technology, Boulder, Colorado.

Ganguly, G.; Suzuki, A.; Yamasaki, S.; Nomoto, K.; Matsuda, A. (1990). *J. Appl. Phys.*; Vol. 68, p. 3738.

Ganguly, G.; Yamasaki, S.; Matsuda, A. (1991). *Phil. Mag.*; Vol. B 63, p. 281.

Ganguly, G.; Matsuda, A. (1994). *Mat. Res. Soc. Proc.*; Vol. 336, p. 7.

Ganguly, G.; Matsuda, A. (1994). *Phys. Rev. B*; Vol. 49, p. 10986.

Ganguly, G.; Nishio, H.; Matsuda, A. (1994). *Appl. Phys. Lett.;* Vol. 64, p. 3581.

Ganguly, G.; Matsuda, A. (1995). *J. Non-Cryst. Solids;* Vol. 198-200, p. 1003.

Guha, S.; Narasimhan, K.L.; Pietruszko, S.M. (1981). *J. Appl. Phys.;* Vol. 52, p. 859.

Guha, S.; Yang, J.; Czubatyj, W.; Hudgens, S.J.; Hack, M. (1983). *Appl. Phys. Lett.*; Vol. 42, p. 588.

Guha, S.; Yang, J.; Nath, P.; Hack, M. (1986). *Appl. Phys. Lett.*; Vol. 49, p. 218.

Guha, S.; Yang, J.; Pawlikiewicz, A.; Glatfelter, T.; Ross, R.; Ovshinsky, S.R. (1989). *Appl. Phys. Lett.*; Vol. 54, p. 2330.

Guha, S.; Yang, J.; Jones, S.J.; Chen, Y.; Williamson, D.L. (1992). *Appl. Phys. Lett.*; Vol. 61, p. 1444.

Guha, S. (1993). *Research on Stable, High-efficiency Amorphous Silicon Multijunction Modules.* NREL/TP-411-5654. Golden, CO: National Renewable Energy Laboratory. Work performed by United Solar Systems Corp., Troy, Michigan.

Guha, S. (1994). *Research on Stable, High-efficiency Amorphous Silicon Multijunction Modules.* NREL/TP-411-7190. Golden, CO: National Renewable Energy Laboratory. Work performed by United Solar Systems Corp., Troy, Michigan.

Guha, S.; Yang, J.; Banerjee, A.; Glatfelter, T.; Hoffman, K.; Ovshinsky, S.R.; Izu, M.; Ovshinsky, H.C.; Deng X. (1994). *Mat. Res. Soc. Proc.*; Vol. 336, p. 645.

Guha, S.; Yang, J.; Banerjee, A.; Glatfelter, T.; Hoffman, K.; Xu, X. (1994). *Solar Energy Materials and Solar Cells*; Vol. 34, p. 329.

Guha, S.; Yang, J., U.S. Patent No. 5,298,086 (29 March 1994).

Guha, S. (1995). *Amorphous Silicon Research.* Golden, CO: National Renewable Energy Laboratory. Work performed by United Solar Systems Corp., Troy, Michigan.

Guha, S.; Xu, X.; Yang, J.; Banerjee, A. (1995). *Mat. Res. Soc. Proc.*; Vol. 377, p. 621

Hazra, S.; Middya, A.R.; Ray, S. (1995). *J. Appl. Phys.*; Vol. 78, p. 581.

Kameda, M.; Sakai, S.; Isomura, M.; Sayama, K.; Hishikawa, Y.; Matsumi, S.; Haku, H.; Wakisaka, K.; Tanaka, M.; Kiyama, S.; Tsuda, S.; Nakano, S. (1996). *Conference Record of the Twenty Fifth IEEE Photovoltaic Specialists Conference-1996*; p. 1059.

Kane, E.O. (1961). *Phys. Rev.*; Vol. 127, p. 131.

Knights, J.C.; Lucovsky, G.; Nemanich, R.J. (1978). *Philos. Mag.*; Vol. B37, p. 467.

Knights, J.C.; Lucovsky, G.; Nemanich, R.J. (1979). *J. Non-Cryst. Solids;* Vol. 32, p. 393.

Lee, S.; Arch, J.K.; Fonash, S.J.; Wronski, C.R. (1990). *Conference Record of the Twenty First IEEE Photovoltaic Specialists Conference*-1990; p. 1624.

Lyding, J.W.; Hess, K.; Kizilyalh, I.C. (1996). *Appl. Phys. Lett.*; Vol. 68, p. 2526.

Matsumura, H.; Okushi, H. (1992). *Amorphous & Microcrystalline Semiconductor Devices.* Edited by J. Kanicki, Artech House, Vol. II; p. 517.

McElheny, P.J.; Suzuki, A.; Mashima, S.; Hasezaki, K.; Yamasaki, S.; Matsuda, A. (1991). *Jpn. J. Appl. Phys.*; Vol. 30, p. L142.

Mimura, H.; Hatanaka, Y. (1987). *Appl. Phys. Lett.*; Vol . 50, p. 326.

Nevin, W.A.; Hamagishi, H.; Asaoka, K.; Nishio, H.; Tawada, Y. (1991). *Appl. Phys. Lett.*; Vol. 59, p. 3294.

Perrin, J.; Takeda, Y.; Hirano, N.; Matsumura, H.; Matsuda, A. (1989). *Jpn. J. Appl. Phys.;* Vol. 28, p. 5.

Ross, R.; Mohr, R.; Fournier, J.; Yang, J. (1987). *Conference Record of the Nineteenth IEEE Photovoltaic Specialists Conference-1987*; p. 327.

Schropp, R.E.I.; Ouwens, J.D.; Von der Linden, M.B.; Van der Werf, C.H.M.; Van der Weg, W.F.; Alkemade, P.F.A. (1993). *Mat. Res. Soc. Proc.*; Vol. 297, p. 797.

Stuzmann, M.; Jackson, W.B.; Smith, A.J.; Thompson, R. (1986). *Appl. Phys. Lett.*; Vol. 48, p. 62.

Tanaka, K.; Matsuda, A. (1987). *Mat. Sci. Report*; Vol. 2, p. 139.

Tsu, D.V.; Chao, B.S.; Ovshinsky, S.R.; Guha, S.; Yang, J. (1997). *Appl. Phys. Lett.*; Vol. 71, p. 1317.

Turner, W.A.; Jones, S.J.; Pang, D.; Bateman, B.F.; Chen, J.H.; Li, Y.M.; Marques, F.C.; Wetsel, A.E.; Wickboldt, P.; Paul, W.; Bodart, J.; Norberg, R.E.; El Zawawi, I.; Theye, M.L. (1990). *J. Appl. Phys.;* Vol. 67, p. 7430.

Verdeyen, J.T.; Beberman, J.; Overzet, L. (1990). *J. Vac. Sci. and Tech.*; Vol. 8, p. 1851.
Williamson, D.L. (1995). *Mat. Res. Soc. Proc.*; Vol. 377, p. 251.

Wronski, C.R; Maley, N. (1991). *AIP Conference Proceedings 234-1991*; p. 11.

Xi, J.; Liu, T.; Iafelice, V.; Si, K.; Kampas, F. (1994). *Mat. Res. Soc. Proc.;* Vol. 336, p. 681.

Xu, X.; Yang, J.; Guha, S. (1993). *Appl. Phys. Lett.*; Vol. 62, p. 1399.

Xu, X.; Yang, J.; Guha, S. (1993). *Conference Record of the Twenty Third IEEE Photovoltaic Specialists Conference*-1993; p. 971.

Xu, X.; Yang, J.; Guha, S. (1994). *J. Non-Cryst. Solids*; Vol. 198-200, p. 60.

Xu, X.; Yang, J.; Banerjee, A.; Guha, S.; Vasanth, J.; Wagner, S. (1995). *Appl. Phys. Lett.*; Vol. 67, p. 2323.

Yang, J.; Ross, R.; Glatfelter, T.; Mohr, R.; Hammond, G.; Bernotaitis, C.; Chen, E.; Burdick, J.; Hopson, M.; Guha, S. (1988). *Conference Record of the Twentieth IEEE Photovoltaic Specialists Conference*-1988; p. 241.

Yang, J.; Xu, X.; Guha, S. (1994). *Mat. Res. Soc. Proc.*; Vol. 336, p. 687.

Yang, J.; Banerjee, A.; Glatfelter, T.; Hoffman, K.; Xu, X.; Guha, S. (1994). *First World Conference on Photovoltaic Energy Conversion Proceedings;* p. 380.

Yang, J.; Xu, X.; Banerjee, A.; Guha, S. (1996). *Conference Record of the Twenty Fifth IEEE Photovoltaic Specialists Conference-1996;* p. 1041.

Yoshida, T.; Ichikawa, Y., Sakai, H. (1989). *9th Euro. Comm. PV Conf. Proc.*, p. 1006.

Yoshida, T.; Hokaya, T.; Ichikawa, Y.; Sakai, H. (1990). *Techn. Digest 5th Int'l PVSEC*; p. 537.

REPORT DOCUMENTATION PAGE

Form Approved
OMB NO. 0704-0188

1. AGENCY USE ONLY (Leave blank)	2. REPORT DATE	3. REPORT TYPE AND DATES COVERED
	May 1998	Final Technical Progress Report; 1 August 1994 – 28 February 1998

4. TITLE AND SUBTITLE
Amorphous Silicon Research, Final Technical Progress Report, 1 August 1994 – 28 February 1998

5. FUNDING NUMBERS
C: ZAN-4-13318-02
TA: PV804401

6. AUTHOR(S)
S. Guha

7. PERFORMING ORGANIZATION NAME(S) AND ADDRESS(ES)
United Solar Systems Corp.
1100 West Maple Road
Troy, MI 48084

8. PERFORMING ORGANIZATION REPORT NUMBER

9. SPONSORING/MONITORING AGENCY NAME(S) AND ADDRESS(ES)
National Renewable Energy Laboratory
1617 Cole Blvd.
Golden, CO 80401-3393

10. SPONSORING/MONITORING AGENCY REPORT NUMBER
SR-520-24724

11. SUPPLEMENTARY NOTES
NREL Technical Monitor: K. Zweibel

12a. DISTRIBUTION/AVAILABILITY STATEMENT
National Technical Information Service
U.S. Department of Commerce
5285 Port Royal Road
Springfield, VA 22161

12b. DISTRIBUTION CODE

13. ABSTRACT *(Maximum 200 words)*

This report describes the status and accomplishments of work performed under this subcontract by United Solar Systems. United Solar researchers explored several new deposition regimes/conditions to investigate their effect on material/device performance. To facilitate optimum ion bombardment during growth, a large parameter space involving chamber pressure, rf power, and hydrogen dilution were investigated. United Solar carried out a series of experiments using discharge modulation at various pulsed-plasma intervals to study the effect of Si-particle incorporation on solar cell performance. Hydrogen dilution during deposition is found to improve both the initial and stable performance of a-Si and a-SiGe alloy cells. Researchers conducted a series of temperature-ramping experiments on samples prepared with high and low hydrogen dilutions to study the effect of hydrogen effusion on solar cell performance. Using an internal photoemission method, the electrical bandgap of a microcrystalline *p* layer used in high-efficiency solar cells was measured to be 1.6 eV. New measurement techniques were developed to evaluate the interface and bulk contributions of losses to solar cell performance. Researchers replaced hydrogen with deuterium and found deuterated amorphous silicon alloy solar cells exhibit reduced light-induced degradation. The incorporation of a microcrystalline *n* layer in a multijunction cell is seen to improve cell performance. United Solar achieved a world-record single-junction a-Si alloy stable cell efficiency of 9.2% with an active area of 0.25 cm^2 grown with high hydrogen dilution. Researchers achieved state-of-the-art top, middle, and bottom component cells; initial and stable characteristics are shown in Table 1 of this report. They also achieved a world-record triple-junction, stable, active-area cell efficiency of 13.0% with an active area of 0.25 cm^2.

14. SUBJECT TERMS
photovoltaics ; amorphous silicon alloy solar cells ; a-Si alloy solar cells ; triple–junction solar cells ; high-efficiency solar cells ; hydrogen dilution ; deposition

15. NUMBER OF PAGES
96

16. PRICE CODE

17. SECURITY CLASSIFICATION OF REPORT	18. SECURITY CLASSIFICATION OF THIS PAGE	19. SECURITY CLASSIFICATION OF ABSTRACT	20. LIMITATION OF ABSTRACT
Unclassified	Unclassified	Unclassified	UL